Enabling Oxide Dispersion Strengthening *via* In-situ Reaction During Laser Powder Bed Fusion Additive Manufacturing: Methods and Mechanisms

by

Houshang Yin

A dissertation submitted to the Graduate Faculty of
Auburn University
in partial fulfillment of the
requirements for the Degree of
Doctor of Philosophy

Auburn, Alabama
Aug 6, 2022

Keywords: Additive manufacturing, Oxide dispersion strengthening, Austenitic stainless steel, Laser powder bed fusion, Pulsed wave laser, Melt pool dynamics

Copyright 2022 by Houshang Yin

Approved by

Xiaoyuan Lou, Chair, Associate Professor of Materials Engineering
Barton C. Prorok, Professor of Materials Engineering
Jeffery Fergus, Professor of Materials Engineering
Robert L. Jackson, Professor of Mechanical Engineering

Abstract

Oxide dispersion strengthened (ODS) steels have continuously attracted interest over the past few decades for their potential applications in fission and fusion nuclear systems, high-temperature heat exchangers, and gas turbines. While powder metallurgy (PM) is the typical process for manufacturing this class of materials, it possesses a great limitation in producing complex geometry for reasonable cost and time. Laser powder bed fusion (L-PBF) additive manufacturing (AM) offers great advantages over PM, enabling complex component design, high production rate, and reduced design iteration. Research has been carried out to fabricate ODS steels by laser AM. Challenges still exist in producing the high-density oxide dispersion during laser solidification.

In this dissertation, the fabrication of ODS steels by (L-PBF) was systematically studied. Different pathways of oxygen intrusion and processing parameters were investigated. The goal is to develop methods and mechanistic understandings to utilize in-situ oxidation to form nanoscale oxides in the steel alloy during laser solidification. First, in-situ oxidation by reacting with a gas-phase oxygen donor was explored. Factors influencing the oxide dispersion in AM steels such as alloy composition, oxygen getter elements, atmospheric oxygen partial pressure, and laser AM parameters were studied. The reasons that present high-density nano oxide dispersion were identified. Second, a reactive AM method was developed to produce AM ODS stainless steel by reacting Y-containing stainless steel powder with solid-phase oxygen donors, like low melting temperature oxides (MoO_3 and Fe_2O_3). High thermal stability was achieved, and the underlying strengthening mechanism was investigated. Third, a different laser mode, pulse wave (PW) emission laser, was used to reduce the oxide spattering during laser melting and thus increase the oxide density in AM ODS steel. Pulse laser showed a great advantage in refining the oxide size and microstructure. The effects of PW laser power, pulse interval, pulse width, and repetition rate on oxide dispersion and steel microstructure were systematically explored. The mechanistic insights on how pulse laser helps oxide dispersion was obtained. Last but not least, the melt pool simulation was performed to understand the effects of pulse laser on melt pool dynamics and temperature distribution, which are believed to be the key controlling factors that affect spattering behavior and phase transformation during laser solidification.

Acknowledgments

I would like to thank the following people, without whom I would not have been able to complete this dissertation.

Firstly, I would like to express my deepest gratitude to my advisor, Dr. Xiaoyuan Lou, for his invaluable guidance and endless support. Under his supervision, I become more explicit about my research goal and how to conduct research and identify and solve problems. His hardworking and passionate attitude inspires me to be a self-motivated and persistent person. I sincerely appreciate his suggestions and kind encouragement, which helps me smoothly finish my Ph.D. journey. I could not have hoped for a better advisor.

Many thanks to my committees: Dr. Barton Prorok, Dr. Jeffery Fergus, and Robert Jackson. Their broad knowledge and experience opened my mind and expanded my research area. I appreciate their tremendous support and invaluable suggestions on my research. I would like to thank Dr. Qinghua (Peter) He, who served as my dissertation reader and helped evaluate this ddissertation.

I would like to thank our collaborators, Andrii Shmatok and Md Fahim Salek, for their help on the XCT; Ralf Fisher's help on the PW laser machine; Bingqiang Wei, Dr. Jian Wang from the University of Nebraska–Lincoln helped with the TEM characterization and micropillar compression; Miao Song from the University of Michigan supported the TEM work; Laura R. Hawkins and Mukesh N. Bachhav from Idaho National Laboratory carried out the APT analysis, and Dr. Lin Jian from Thermo Fisher Scientific helped us do the 4D STEM analysis.

Special thanks to department technician Mr. Steven Moore for equipment training and department secretary Ms. Cheryl Rhodes for organizing fantastic activities. I also want to thank my teammates: Dr. Pu Deng, Dr. Jiacheng He, Dr. Jiacheng Liu, Jingfan Yang, Qingyu Pan, Ralf Fisher, and Josh Le. I appreciate their insightful suggestions, ideas, and friendship. I also thank my friends at Auburn for their thoughtful suggestions and companionship.

Finally, I would like to express my great thanks to my family and my beloved wife, Yuying Zhang. This dissertation would have been impossible without their endless support, warm love, and patience.

This work was primarily sponsored by the National Institute of Standards and Technology under contract NIST-70NANB18H220.

Table of Contents

List of Tables

List of Figures

List of Abbreviations

AM	Additive Manufacturing
L-PBF	Laser Powder Bed Fusion
ODS	Oxide Dispersion Strengthening
SS	Stainless Steel
DED	Direct Energy Deposition
SLM	Selective Laser Melting
SE	Secondary Electron
BSE	Backscattered Electron
EDS	Energy Dispersive X-ray Spectrometry
SEM	Scanning Electron Microscopy
EBSD	Electron Backscattered Diffraction
TEM	Transmission Electron Microscopy
HAADF	High Angle Annular Dark Field
FIB	Focused Ion Beam
XCT	X-ray Computed Tomography
HAGB	High Angle Grain Boundary
LAGB	Low Angle Grain Boundary
PW	Pulse Wave
CW	Continuous Wave
FMS	Ferritic/Martensitic Steels

PM	Powder Metallurgy
MA	Mechanical Alloying
HIP	Hot Isostatic Pressing
HE	Hot Extrusion
TMT	Thermomechanical Treatment
SPS	Spark Plasma Sintering
3D	Three-Dimensional
CAD	Computer-Aided Design
VED	Volumetric Energy Density
APT	Atom Probe Tomography
NC	Nanocrystalline
SF	Schmid Factor

CHAPTER 1

INTRODUCTION

1.1 Motivation for This Research

The rapidly growing demand for energy forms without green gas emissions stimulates great interest in advanced fission and fusion reactors. However, the advanced designs of fission and fusion reactors require the systems to operate under extremely harsh conditions where high temperature, radiation, stress, and corrosion/oxidation are expected. These enormous challenges demand the development of high-performance materials with a good balance of mechanical, physical, and radiation properties that can be sustained under long-term service in the above-mentioned hostile environment. Over the past few decades, ODS steels have continuously attracted interest for their potential applications in fission and fusion nuclear systems and high-temperature heat exchangers.

The excellent properties of ODS steel come from the high-density nanoscale oxide dispersion in the alloy matrix. Alloy composition and manufacturing process dictates the oxide formation, dispersion, and mechanical properties. The traditional method to fabricate ODS steels is through the powder metallurgy (PM) process, involving time-consuming ball milling and mechanical alloying and consolidation. Its incompetence in creating geometric complexity limits the use of ODS steels in energy sectors.

The ongoing development of additive manufacturing (AM) technology presents an opportunity to produce complex parts with ODS steels. By rapid and localized laser solidification, the formation of nanoscale oxide particles by in-situ oxidation in the melt pool during laser AM.

Although a tremendous amount of work has been conducted to fabricate ODS steels by laser AM over the past few years, none have demonstrated a comparable oxide density to those made by the conventional method. A systematic study of oxygen uptake, reaction, and oxide nucleation/growth during laser AM is desired. On the other hand, oxygen loss during laser AM was often significant but not well understood. A better understanding of the oxygen pathway in the melt pool and reaction dynamics is critical for uncovering the factors that inhibit the oxide dispersion during laser AM.

1.2 Research Objective and Technical Approaches

This work focuses on fabricating AM ODS stainless steels via in-situ oxidation between alloys and oxygen donors. The laser processing of alloys mixed with Y_2O_3 is not of interest. The primary goal of this work is to establish mechanistic understandings of in-situ oxide dispersion during laser solidification and develop insights to further optimize the process to achieve true oxide dispersion strengthening. The specific technical objectives are:

(1) To systematically investigate the in-situ oxidation of AM 316L SS alloyed with different oxygen getters under an oxidizing atmosphere in L-PBF. Factors influencing the oxide dispersion in AM steels, such as alloy composition (mainly oxygen getter elements), the oxygen level in the shielding gas, and laser AM parameters, were studied.

(2) To understand the effectiveness of solid-phase oxygen donor (other type oxides, MoO_3/Fe_2O_3) to in-situ oxide dispersion during L-PBF AM. Excellent thermal stability and mechanical properties were observed by optimizing the oxide concentration, process, and heat treatment. The advantages and challenges of fabricating ODS steel by reactive AM were discussed.

(3) To develop the pulse-wave (PW) laser technology to promote high-density oxide dispersion by reactive AM. The study understands the impacts of PW laser parameters on the oxide size, distribution, and mechanical properties.

(4) To reveal the mechanisms that inhibit high-density oxide dispersion during laser AM through the melt-pool dynamic modeling and powder spattering study.

In order to achieve these objectives, microstructural and mechanical characterization of different samples fabricated by L-PBF were carried out in this study. The oxide chemistry, size, and distribution were analyzed by scanning electron microscopy (SEM), transmission scanning microscopy (TEM), and atom probe tomography (APT). The maco- and micro-mechanical properties were investigated by the Vickers hardness tester, nano indenter, and micropillar compression. The spattering video was captured by a high-speed camera. The melt pool modeling used a finite volume method (FVM) by commercial software, FLOW-3D. Thermodynamic simulations were calculated with the Pandat using the PanFe database.

1.3 Organization of Upcoming Chapters

In the following, Chapter 2 will provide a review of the ODS steels, additive manufacturing, PW laser, and previous studies on the AM ODS steels. Chapter 3 will summarize the experimental and simulation methods, including materials, AM processing conditions, material characterization, mechanical testing, melt pool simulation, and thermodynamic calculation. Chapter 4 will present the in-situ oxidation during laser additive manufacturing (AM) by tailoring the oxygen level in the shielding gas during the printing process. This work seeks to validate if the gas-phase oxygen donor can enable in-situ oxide dispersion and understand the roles of major controlling factors, including the choice of the alloying element with different oxygen affinity, concentration, and oxygen level in shielding gas during AM process, and laser parameters. Chapter 5 will demonstrate reactive AM by using solid-state oxygen donors as an effective way to promote oxide nucleation and stabilize cellular dislocation boundaries. High thermal stability was achieved by optimizing the oxygen concentration, alloy design, and heat treatment. The root cause of the excellent mechanical properties was studied through advanced characterization and small-scale mechanical testing. Chapter 6 will investigate the advantage of pulse laser AM in refining the microstructure in AM steels. The study evaluates the effects of various pulse laser parameters on the microstructure and mechanical properties of AM 316L SS. In Chapter 7, the material characteristics and mechanical properties of AM ODS steels by either in-situ reaction to low melting temperature oxides or laser solidification with Y_2O_3 pre-mix were evaluated under various PW laser parameters. In Chapter 8, the fundamental reasons that inhibit the high-density nano oxide dispersion are studied by melt pool modeling, thermodynamic simulation, and experiments. Chapter 9 will give an overview of the fabrication of L-PBF ODS steels by reactive AM and provide recommendations for future research.

CHAPTER 2

BACKGROUND

2.1 Oxide Dispersion Strengthening (ODS) Steels

The challenges of meeting the rapidly growing demand for energy while reducing reliance on fossil fuels have been a worldwide interest in advanced fission and fusion energy [1]. Fission and fusion reactor service conditions are characterized by combinations of high temperatures, significant time-varying stresses, chemical reactive environments, and intense neutron radiation fields [2–5]. These enormous challenges underscore the need to develop high-performance materials with an outstanding balance of mechanical, physical, and radiological properties that can be sustained under long-term service in the abovementioned hostile environment. ODS steels are the most promising structural material. Over the past few decades, they have continuously attracted interest for their potential applications in fission and fusion nuclear systems [6–8] and high-temperature heat exchangers [9].

Oxide dispersion strengthening steels generally contain a dense and uniform dispersion of nano-scale oxides (typically yttrium oxide or its variants) with an average size of sub 10 nm and the volumetric number density of 10^{21}-$10^{24}/m^3$ [10–12]. The dense oxide dispersion is critical to improving the high-temperature mechanical properties by limiting dislocation mobility and reducing the structural damages by neutron/ion irradiation by providing sinks to recombine point defects. Therefore, ODS steel has been considered one of the most promising materials for fourth-generation nuclear fission reactor cladding tubes and nuclear fusion reactor blankets [13,14].

2.1.1 ODS Alloys

Advanced steels and Ni-based superalloys are commonly used in high-temperature applications because of their excellent high-temperature strength, ductility, excellent creep strength, and good oxidation/corrosion resistance. Unfortunately, these alloys cannot fully meet the requirements for high-temperature reactor applications. For example, ferritic/martensitic steels (FMS) are limited to around 600℃ [13] due to inferior tensile and creep strength at higher temperatures. The use of Ni-based alloys is also limited by radiation-induced transmutation and the thermal stability of the precipitates in high-temperature irradiation environments [15].

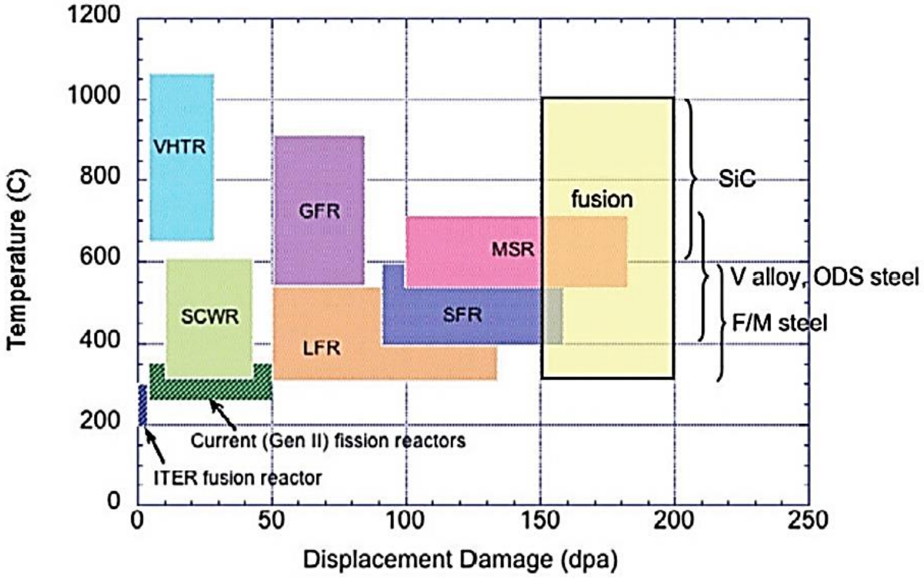

Fig. 2-1 Overview of operating temperatures and displacement damage dose regimes for structural materials in the current (generation II) and proposed future (Generation IV) fission and fusion energy systems [16].

Fig. 2-1 compares the proposed operating temperatures and lifetime displacement damage level for structure materials in the six Generation IV reactor concepts and three fusion energy systems. While the high operating temperature contributes to economic benefits, it demands better materials to service in harsh conditions. ODS Ni-based and Fe-based alloys have attracted great research interest from both high-temperature material and nuclear material communities. Benjamin et al. first developed Ni-based ODS alloy with his co-workers around 1966 [17]. Since then, various ODS alloys have been developed and commercialized for nuclear and aerospace applications. Table 2-1 summarizes some typical mechanically alloyed (MA) ODS alloys that are commercially available. Y_2O_3 is the choice of oxide reinforcement in all these alloys.

Table 2-1 Summary of typical ODS alloys[18–20]

Type	Matrix	Chemical composition in wt.%										
		Ni	Fe	Cr	Ti	V	Mo	W	Al	C	Ta	Y_2O_3
MA754	Ni-based	Bal	1	20	0.5	-	-	-	0.3	-	-	0.6
MA758		Bal	1	30	0.5	-	-	-	0.3	0.05	-	0.6
MA6000		Bal	-	15	0.5	-	4	-	4.5	-	2	1.1
PM 1000		Bal	-	20	-	-	0.3		0.3			0.6
12YWT	Fe-Based	-	Bal	12.3	0.39	-	-	3	-	-	-	0.25
14YWT		-	Bal	14	0.3	-	-	3	-	-	-	0.25
PM2000		-	Bal	18	0.5	-	-	-	5.5	-	-	0.5
MA 956		-	Bal	20	0.5	-	-	-	4.5	-	-	0.5
MA957		-	Bal	14	1	-	0.3	-	-	-	-	0.25
Eurofer97	F/M	-	Bal	9	0.3	0.2		1.1	-	-	0.14	0.3

The microstructure and mechanical properties of ODS steels depend not only on the manufacturing process but also on the alloy composition. In view of the mechanical properties, W, Mo, and Ta are sometimes added to provide solution strengthening. A high Cr (15~20 wt%) strategy and a certain amount of Al is usually adopted in composition design for good corrosion and oxidation resistance. For example, PM 2000 and MA 956 have 5.5 wt% and 4.5 wt% Al, respectively. The aluminum can improve ODS steel's corrosion and oxidation resistance by forming a dense alumina layer [21]. A small amount of transition metal additions is also necessary for high-temperature ODS alloys because of their beneficial effects on controlling nano oxide composition, which will further affect oxide size, density, and thermal stability.

2.1.2 Characteristics of Nanoscale Oxides in ODS alloys

Y_2O_3 is the most commonly used feedstock oxide to prepare ODS alloys due to its remarkable thermal stability [22]. A small amount of transition metal elements such as Ti, Al, Zr, and Hf are added to refine the oxides and improve oxide dispersion. It was reported that Ti plays a significant role in improving the dissolution of Y_2O_3 particles during the MA process and promoting the formation of Y-Ti-O nano dispersoids [23]. The structure and chemistry of the phase transformation of oxides in ODS steels have been extensively investigated using TEM and APT[24–29]. Based on TEM observation, large Y-Ti-O nanoparticles have been transformed into two equilibrium phases, $Y_2Ti_2O_7$ and Y_2TiO_5 [23,28]. However, the results from atom probe tomography (APT) show the Y/Ti ratio is much smaller than one [30], far from the reported TEM $Y_2Ti_2O_7$ and Y_2TiO_5. Non-stoichiometric Ti, Y, and O enriched small nanoclusters at the size of 2-15 nm and $Y_2Ti_2O_7$ precipitates at the size of ~15-35 nm were reported by Sakasegawa [31]. Although the composition depends on the chemical composition and the processing parameters of the ODS steel, generally, Ti addition can reduce the oxide size by forming nanoclusters or Y-Ti-O oxides. Aluminum addition is favorable for corrosion resistance, but it enables the formation of large Y-Al-O particles, such as $YAlO_3$, $Y_4Al_2O_9$, and $Y_3Al_5O_{12}$ [32–34]. The size of Y-Al-O particles ranges from several to hundreds of nanometers and can deteriorate the mechanical properties. The addition of Zr was found to strongly suppress the formation of Al and Y oxides in ODS steel [35]. Also, the first principle calculation indicates that the binding energy of Y-Zr-O and Y-Hf-O clusters are higher than Y-Al-O and Y-Ti-O clusters in the ferrite matrix[36]. Smaller Y-Zr-O oxide nanoparticles in Zr-contained ODS steels can lead to the formation of more homogenous and dispersive oxides [37].

In summary, the oxide types in ODS alloys are complex, highly dependent on the alloying elements. Zr and Ti addition generally favors the formation of small oxides and increases the number density, while Al addition results in oxide coarsening.

2.1.3 Conventional Preparation Processes

In addition to alloy composition, numerous studies show that the preparation process significantly affects the average size, number density, and distribution of nano-oxides [38]. The preparation process also determines the high-temperature service performance and irradiation swelling resistances. This section summarizes the research progress on ODS steel preparation, including powder metallurgy (PM), liquid metal forming, and hybrid processes.

2.1.3.1 Powder Metallurgy Process

At present, the primary preparation method for ODS steel is through the powder metallurgy process. Fig. 2-2 shows the detail of the PM process. The standard PM route consists of the following steps [13], including (1) selection of the steel composition; (2) steel powder production through gas atomization (master alloy); (3) blending of the steel powder and commercial Y_2O_3 at the size of 20-200nm; (4) mechanical alloying (MA) by ball mills or attritor mills; (5) canning and degassing; (6) consolidation using hot isostatic pressing (HIP), hot extrusion (HE), or spark plasma sintering (SPS); (7) heat treatment or thermomechanical treatment.

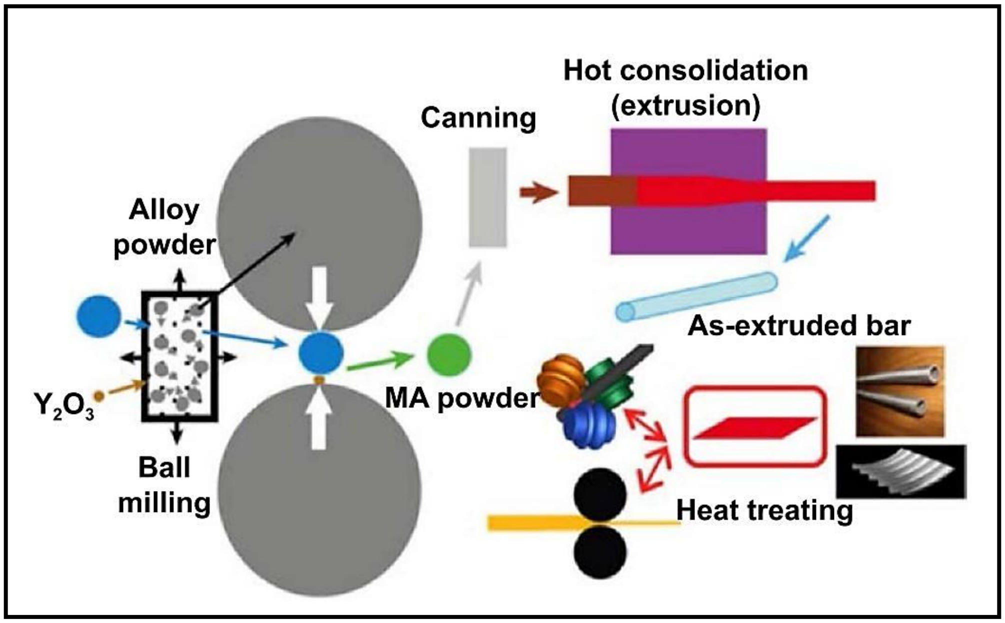

Fig. 2-2 Powder metallurgy process of ODS steels [39].

Among these steps, MA is critical to the quality of the final product. Processing parameters such as milling speed, ball-to-powder weight ratio, milling time, milling atmosphere, and milling temperature need to be optimized to break the oxide particles down into Y-O dispersoids. While the PM process has been commercialized to produce tube and bar forms of ODS steels [6,9], it suffers from low yielding and poor batch-to-batch repeatability [38,40]. High manufacturing costs and lack of the ability to form complex geometry limit its use in manufacturing large and complex components [41,42].

2.1.3.2 Liquid Metal Forming Process

The liquid metal forming of ODS steels directly adds fine oxide powders into molten steel during casting and disperses oxides uniformly in the steel matrix. The process was affected by the poor oxide wettability in molten metal, agglomeration, and the buoyancy of lower density oxides. To prevent agglomeration of the nano oxides, the use of Y_2O_3 colloidal suspensions with low concentration/viscosity has been investigated [43], resulting in nonuniform oxide dispersion in the steel matrix. Interestingly, the addition of Y improved the wettability of Y_2O_3 and promoted the dispersive distribution of Y_2O_3. Instead of adding Y_2O_3 directly to molten metal, an alternative method by pouring Y-contained liquid metal into the oxygen carrier Fe_2O_3 demonstrated the possibility of directly casting ODS steels, as shown in Fig. 2-3.[44].

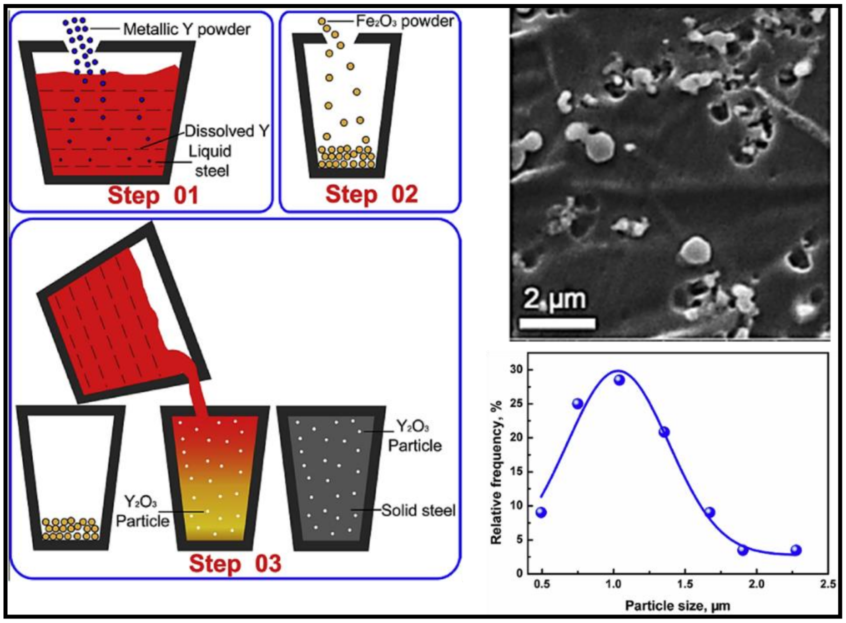

Fig. 2-3 Schematic representation of producing ODS steel by the Fe_2O_3 oxygen carrier casting method[44].

Through reactive casting, the formation of Y_2O_3 was completed in a short time, which inhibited the oxide coarsening and agglomeration. Unfortunately, this process can only obtain submicron size oxides. The cooling rate of the casting process is slow, which provides time for oxide growth.

The development of casting technology for ODS steels requires innovative solutions to several complex engineering challenges: dispersing particles uniformly in the liquid, avoiding the agglomeration of the nanoparticles, and improving the wettability between oxide and liquid metal. Key challenges remain for the liquid metal process, but its potentials to lower manufacturing costs and scalability continue to attract research in this field.

2.1.3.3 Hybrid Process

The term hybrid process refers to the fabrication methods involving MA or liquid metal processes. It can be understood in a broader context to contain elements of chemical, physical or metallurgical principles. For example, there is a continuing interest in controlling the internal oxidation of steel powders to reduce or even eliminate the MA step in the standard PM route. There are also attempts to combine the MA process with the casting process to form oxides by the in-situ reaction. The challenges listed above still exist when multiple processes are involved in manufacturing.

In summary, the conventional PM process is able to fabricate high-quality ODS steels for simple geometries. But the high manufacturing cost and difficulty of forming complex components limit its adoption at a large scale in the industry. Other methods based on liquid metal forming are actively explored with the intention to lower manufacturing costs and support large-scale industrial use.

2.2 Additive manufacturing

Additive Manufacturing (AM), also known as three-dimensional (3D) Printing, has gathered much interest from researchers in the past few years[45]. Based on the digital model, parts can be built layer upon layer by a localized laser solidification. Unlike traditional subtractive manufacturing, it provides a bottom-up approach to form net-shape structures. This technology makes it possible to manufacture complex structural parts that cannot be made by traditional manufacturing methods. Common materials for laser AM include stainless steel, aluminum alloys, titanium alloys, Ni-based alloys, CoCr, etc. [46,47]. According to ASTM Standard [48], laser based AM processes include directed energy deposition (DED) and powder bed fusion (PBF), with laser beam as the primary heat source. Laser powder bed fusion (L-PBF) represents the most widely adopted metal additive manufacturing (AM) technology, offering high geometric resolution and fast fabrication speed to produce complex-shaped components [23–25].

2.2.1 Laser Powder Bed Fusion (L-PBF)

According to SmarTech Publishing's latest metal AM report, "Additive Manufacturing with Metal Powders 2018", L-PBF technology is one of the most studied AM methods [49]. Also known as selective laser melting (SLM), it spreads and solidifies metallic powder layer by layer in a powder bed to produce dense metallic parts. Fig. 2-4 shows the typical working mechanism. The power input and layer thickness need to be optimized so there is no lack of fusion through the build direction. Inert shielding gas (typically argon or nitrogen) flows above the powder bed to prevent extensive oxidation and carry away the spattered powder. The obtained geometric tolerance and minimum feature size are between 40 and 200 μm[50].

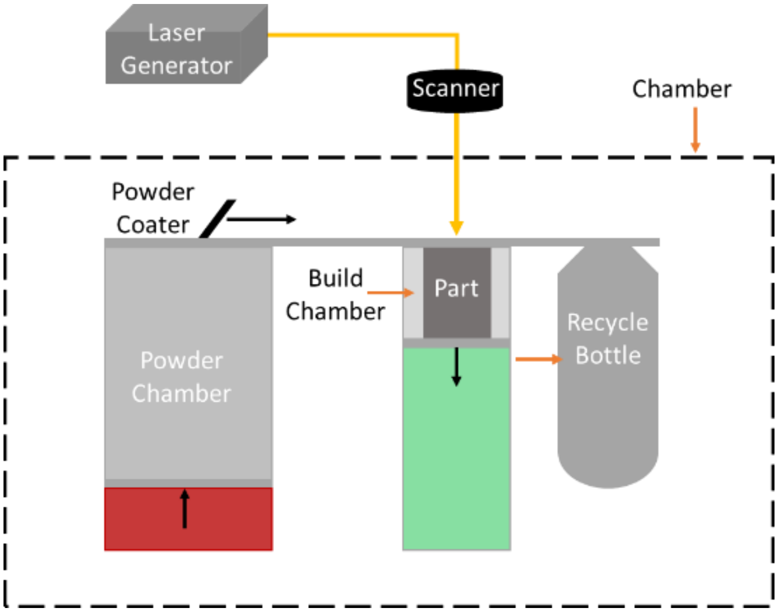

Fig. 2-4 Schematic of operating process design in L-PBF.

L-PBF process has the advantage over the conventional method to fabricate parts with complex internal features at high production rate. It can also be used in prototyping to reduce design iteration [51,52]. Depending on the materials to be fabricated, L-PBF AM can still face challenges from process-induced thermal residual stress, solidification cracking/defects, dimensional inaccuracy, part-to-part variability, and many metallurgical imperfections [53].

The laser solidification produces a smaller melt pool, resulting in a cooling rate up to 10^3–10^8 K/s. Such a high cooling rate was reported to induce non-equilibrium microstructures, including ultrafine nanostructures and precipitates, unique local elemental segregation, disconnected low angle boundaries, nanoscale cellular structures, metastable phases, etc. [REF]. These unique structural features can play either beneficial or detrimental roles in the physical and mechanical properties.

2.2.2 AM ODS Steels

If AM can be further developed to fabricate ODS steels, it will solve many grand challenges that were discussed in the earlier sections. Attempts were made to develop laser AM for ODS alloys. High oxygen content is usually harmful to cast or weld metals due to the formation of large oxide inclusions, which degrades the mechanical properties. However, with the rapid and localized solidification, laser AM was reported to produce oxide inclusions at the nanoscale [54,55]. For instance, AM 316L stainless steel (SS) made by L-PBF contains high-density Si and Mn-rich oxides at an average size of 40-50 nm [56–58]. With these unique processing characteristics, a tremendous amount of work has been reported to fabricate ODS steels by laser AM, which can be categorized into two main approaches. In the first approach, AM ODS steels were made by laser melting a mixture of steel and nano-oxide powders pre-made by high-energy ball milling. Walker et al. [59] reported to use L-PBF to fabricate pre-synthesized PM 2000 ODS steel powder. This method produced Y-Al-O oxides with the size of 54-60 nm, one order of magnitude larger than those found in traditional ODS steels. Other similar work done by Boegeleine et al. [60,61] showed the thin-walled builds of AM PM 2000 with MA powders had yield strength (YS) inferior to the HIPed counterparts that were made with the same powders. Still, the YS could be further improved by post-heat treatment due to the precipitation of fine Y-enriched particles. Recent work by Ghayoor et al. [62,63] showed that AM ODS steels with similar quality could be fabricated without involving powders broken down via high-energy ball milling. Submicrometer yttria particles could be broken down by laser melting to form ODS 304L SS. Zhai et al. [64] reported that the feedstock powder containing nano-oxide particles and coarse SS powders mixed by low-energy milling yielded an excellent quality ODS SS with a density of 99.5%. In this case, Y_2O_3 agglomeration was observed. Similar approaches by using powder mixing, such as Fe-14Cr-Y_2O_3 [65], and Ti-45Al-3Nb-Y_2O_3 [66], were also reported for AM.

Oxide dispersion via in-situ oxidation reaction during melting was recently reported as an alternative approach to fabricating ODS steels during laser solidification [67–73]. This method eliminates high-energy ball milling and can potentially reduce the overall manufacturing cost. Mirzababaei et al. [67] reported nano oxide dispersion in FeCrAlY steel via internal oxidation could be enhanced by high-level excess oxygen in the powder and surrounding environment. Haines et al.'s work [68] also demonstrated that reactive gases such as oxygen and carbon dioxide could be used in the printing atmosphere during L-PBF AM to produce oxide-rich FeCrAlTi SS with improved mechanical properties at both room temperature and elevated temperatures. However, their results showed the produced oxide density was at the level of $10^{19}/m^3$, significantly lower than the conventional ODS alloys.

While a large body of recent studies has reported the development of AM ODS steels, to the best of our knowledge, none of them demonstrated comparable oxide density as those made by conventional means. Under laser solidification, both manufacturing approaches, either oxide pre-mixing or in-situ formation, face the same challenge of maintaining material quality and adequate oxide size/distribution. The loss of oxide or oxygen reactant was the primary factor limiting the performance of the final product. Introducing the amount of oxygen reactant higher than expected was generally utilized to maintain the oxygen level in the material [62,74,75] but often led to a high level of manufacturing defects in the product. It should be noted that most work so far focused on simply reporting the ODS fabrication for different alloy systems and the resulting properties. Systematic studies of oxygen uptake, reaction, and oxide nucleation/growth during AM are limited. Understanding oxide reaction in the melt pool and its pathway is critical for revealing the mechanistic obstacles that inhibit the dense oxide dispersion.

2.3 Laser configuration in Additive Manufacturing

As an essential component in the L-PBF system, laser working mode and parameters can significantly affect the quality of the AM metal parts and microstructure development. The details are summarized in the following sections.

2.3.1 Laser Working Mode

A laser can be operated as a continuous wave (CW) laser and a pulse wave (PW) laser. CW laser provides constant power output over the time of manufacturing, while PW laser operates in the pulse mode to output in a short and periodic fashion. Both laser modes have been used in laser AM to manipulate part quality and microstructure.

2.3.1.1 Continuous Wave Laser

At present, metal AM technologies are predominantly reliant on CW laser to melt materials [76]. In industry, CW lasers are normally utilized for welding and cladding, whereas PW lasers are considered when precision is required for fabricating and cutting thin parts [77]. In the CW laser-based AM, the important processing parameters include hatch spacing, scanning speed, laser power, and layer thickness. These parameters combined contribute to the overall laser energy density used for melting [53]. Despite the popularity of CW laser in the commercial L-PBF process, there are challenges to using CW laser to fabricate ceramics and refractory metals due to their high melting temperatures and high thermal conductivity [78]. To process such materials, a pulse laser has been used to reach very high temperatures while minimizing the heat-affected zones [79].

2.3.1.2 Pulse Wave Laser

PW laser, on the other hand, produces an intermittent release of energy during the process. Recently, the need for PW laser AM has increased in the industry to satisfy the demands to print those hard-to-print materials. Although PW laser AM is a relatively new area, recent work has highlighted its advantages over CW laser in handling high-temperature materials [80,81]. PW laser offers greater advantages over CW laser in terms of better manufacturing resolution, less residual stress, and reduced global heat input. PW and CW lasers create different heating profiles and thermal histories during AM, which further produce vastly different microstructural and mechanical properties. A faster solidification rate is created by PW laser, leading to microstructure refinement.

Ullsperger et al. [82] utilized ultrashort PW laser to fabricate Al-40 wt.% Si alloys thin-wall structure with high precision. As shown in Fig. 2-5, the refinement of primary Si particles and the reduction in the melt pool size were observed by decreasing PW laser pulse duration under the same scan speed of 167 mm/s and the repetition of 20 MHz (Fig. 2-5). The unique microstructure produced by pulse laser results in a microhardness that is distinctly higher than the material that was produced by CW laser and thermal spray.

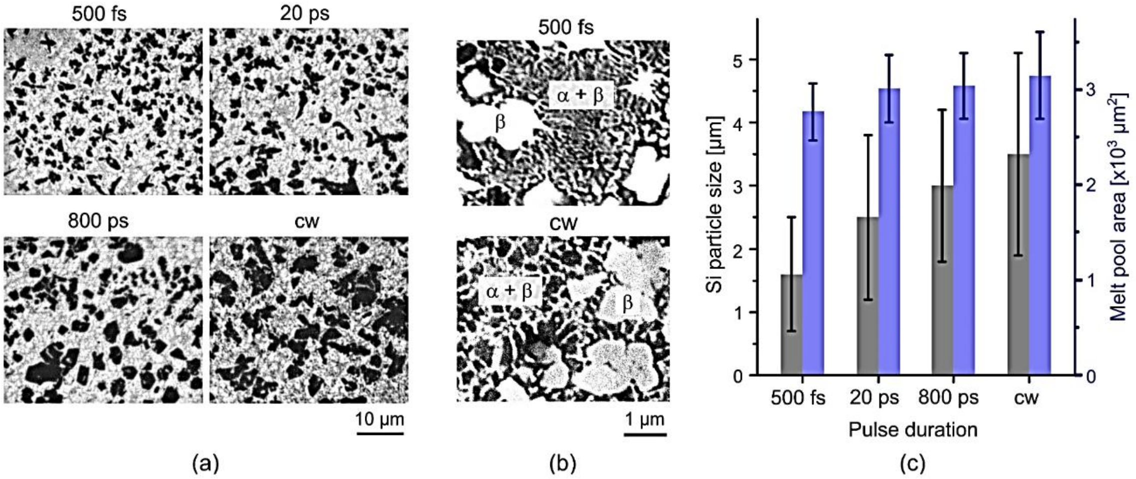

Fig. 2-5 (a) OM images of the fused walls using a repetition rate of 20 MHz and a scan speed of 167 mm/s. Si appears in black, and α-Al in white. (b) BSE images of the L-PBF samples at higher magnification, where the white phase is Si, and the black is α-Al. (c) The mean size of the primary Si phase and the melt pool area depends on the pulse mode [82].

Pinkerton and Li [83,84] found that the hardness of the stainless steel clads made by PW laser was positively correlated with the pulse frequency but negatively correlated with the pulse duty cycle. Lower surface roughness and higher hardness were obtained in AM Ti-6Al-4V by using a PW laser. Another study by Rave et al. [85] shows PW laser can refine grain structure and induce the nucleation of fine equiaxed grains. PW laser also showed great potential to reduce the Nb segregation and control the morphology of Laves phase in Inconel 718 [86–88]. The refinement in the microstructure by PW laser was claimed that attributed to a high cooling rate and a melt pool disturbance by Ravi et al. [85] and Xiao et al. [86,89]. The enhanced cooling rate and refined phase in the PW laser AM process could also benefit ODS alloys with PW laser. The PW effects on the AM ODS 316L SS will be discussed in chapters 6-8.

2.3.2 Critical Laser Parameters

For CW laser AM, laser parameters include laser power (P, W), scan speed (υ, mm/s), hatch spacing (h, μm), and layer thickness (T, μm). The volumetric energy density (VED) is employed to examine the overall energy input to the material, which can be linked to melting pool dimension and microstructure [90,91]. The VED is expressed as:

$$VED = \frac{P}{\upsilon h T} \tag{1}$$

Sometimes, h also refers to the spot size of the laser rather than the hatch spacing, especially in the case of the single-track scan. Many studies have been performed to verify the relationship between the process parameters and the relative density of the material. The maximum relative density is required for structure materials, and usually, there is a range of VED values to achieve the highest density.

Compared to the abovementioned parameters that CW laser operates on, PW laser parameters are more complicated. Square wave shaping of laser power is a standard method to transfer the laser energy into PW laser. The pulse laser configuration is presented in Fig. 2-6 [92]. The pulse energy E can be expressed as [92]:

$$E = \int_0^{t_{on}} P(t)dt \tag{2}$$

where $P(t)$ is the power level, which can vary as a function of time t, t_{on} is the duration of the pulse or the pulse width. Pulse repetition rate (RR) can be defined as:

$$RR = \frac{1}{t_{on} + t_{off}} \tag{3}$$

where t_{off} is the temporal distance between the end of the pulse and the beginning of the consecutive one, also being referred as pulse interval in this dissertation. There is another critical parameter in PW laser, duty cycle δ, which expresses the laser on time over the whole pulsation period and can be calculated as:

$$\delta = \frac{t_{on}}{t_{on} + t_{off}} \tag{4}$$

For a square-wave-shaped pulse, the pulse profile doesn't change throughout the duration. Hence, average power (P_{avg}) in PW emission can be calculated as:

$$P_{avg} = E \cdot RR = P_{peak} \cdot \delta \tag{5}$$

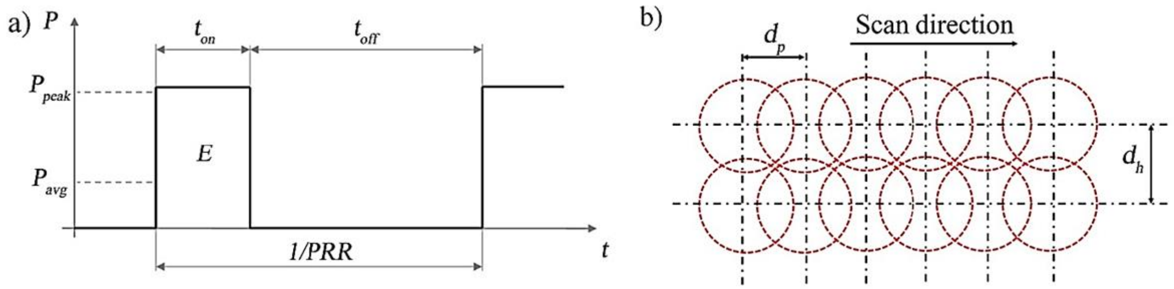

Fig. 2-6 Schematic representation of (a) temporal and (b) spatial disposition of PW laser.

Laser power, pulse width, and the repetition rate can be classified as independent parameters, which are related to the melt pool geometry of a single pulse laser spot. The others are dependent variables that can be derived from the independent ones. These make it even more complicated how PW laser parameters affect the relative density and microstructure of AM parts.

2.4 Spattering During the Additive Manufacturing

The powder spattering phenomenon is generally observed during laser-based machining and manufacturing processes. In AM process, spattering refers to the ejection of materials from the melt pool and then possibly being re-deposited in the nearby region or removed by shielding gas [93]. The spatters have been confirmed to create defects in the parts [94]. Spattering during AM of ODS steels can be more complex. Oxides in the melt tend to float to the surface and agglomerate to create scales. A thick scale reduces the ability of the laser to provide energy to the metal, which in turn deteriorates the melting and stability of the melt pool [95]. Also, these oxides can be spattered during the laser process and lead to the loss of oxygen from AM ODS alloys.

2.4.1 Powder spattering mode

Melt pool spattering has been studied by utilizing different techniques, such as visible light, IR videography [96–98], simulations [99], and high-speed x-ray imaging [94]. Five types of spattering modes (solid spatter, metallic jet, powder agglomeration spatter, entrainment melting spatter, and defect-induced spatter) were identified, as shown in Fig. 2-7, and the formation mechanisms are discussed below [94].

(1) Solid spatter: during scanning, a large amount of un-melted spatter is generated throughout the entire build process. The intense vapor generated by the localized laser heating, referred to as “vapor jet,” created sufficient force to eject un-melted powder before melting. Solid spatter formation can lead to non-uniformity in powder layer thickness but has less effect on the overall part quality.

(2) Metallic jet: liquid droplets are observed ejected from the melt pool at the edge of the depression zone, and this type of spatter is referred to as metallic jet spatter. The intense metallic vapor generates high recoil pressure and strong melt flow. When the metallic vapor is intense enough to produce force capable of overcoming the surface tension, liquid metal can be ejected from the melt pool and form metallic jet spatters.

(3) Powder agglomeration spatter: powders and spatters can agglomerate and coalesce to form spatters much larger than the original feedstock powder. Liquid-solid and liquid-liquid powder agglomeration are the two main kinds of powder agglomeration spatters.

(4) Entrainment melting spatter: ambient gas flow can carry powders/spatters to the laser heating region, and once they encounter the laser beam, the solid powders/spatters are melted and ejected by vapor jet. This type of spatter is referred to as an entrainment melting spatter.

(5) Defect-induced spatter: when the laser interacts with a severe defect like large pores, laser interaction with these large pores exhibits sudden instability, resulting in the eruption of liquid spatter. Fig. 2-7 schematically shows the spatter types and their formation mechanisms.

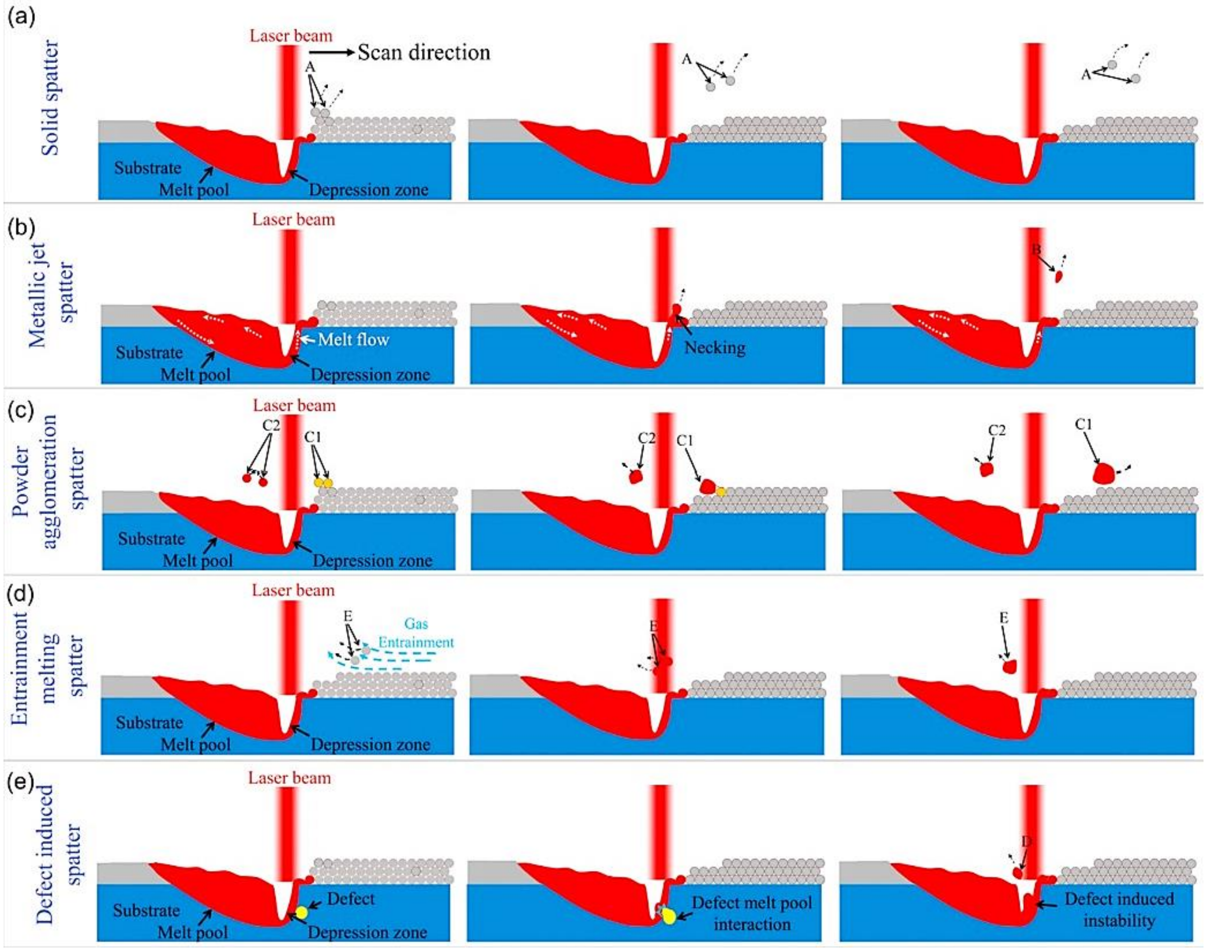

Fig. 2-7 Schematics show the formation mechanisms of all spatter types. (a) Solid spatter (A). (b) Metallic jet spatter (B). (c) Powder agglomeration splatter (C1, liquid-solid agglomeration spatter, C2, liquid-liquid agglomeration spatter). (d) Entrainment melting powder spatters (D). (e) Defect-induced spatter (E)[94].

During the L-PBF process, different parameters like laser power and scan speed will cause various spattering phenomena. PW laser may cause different spattering behavior from CW laser.

CHAPTER 3

EXPERIMENT

3.1 Materials

316L stainless steel (SS) is widely selected for energy-industry applications such as nuclear reactor services. This is primarily due to its good mechanical and corrosion properties in the low to intermediate temperature range. While many similar performing materials are still challenging to produce with AM processes reliably, 316L SS by AM L-PBF is well accepted as a leading AM material due to its easy fabrication, good mechanical and corrosion properties, and good overall part quality.

In Chapter 4, three different alloying elements, Si, Al, and Y, were selected as the candidate oxygen getter elements for ODS 316L SS due to their different oxygen affinity. Table 3-1 shows the alloy compositions of the feedstock powders used in this work. Commercial 316L powder manufactured by nitrogen-gas atomization (Carpenter Technology, USA), designated as "316L-Si", was employed to study the Si effect. Al-doped 316L SS powder, designated as "316L-Al", was also manufactured directly by nitrogen-gas atomization (Carpenter Technology, USA). It should be noted that Si in 316L-Al powder was removed to prevent the effect of Si. Y-doped 316L SS powder was pre-made by ball-milling a custom-made 316L-0Si SS powder and high-purity yttrium powder with a planetary ball miller (Fig. 3-1) at different concentrations. 316L-0Si was fabricated via nitrogen-gas atomization (Carpenter Technology, USA) by intentionally removing Si and Mn from the standard 316L SS composition. The high-purity irregularly shaped yttrium powder (99.9%, US Research Nanomaterial Inc., USA) with an average particle size of 40 μm was used. The low-energy ball milling resulted in Y-doped 316L SS powder with Y content varied from 0.5, 1.2, and 2 wt.%, designated as "316L-0.5Y", "316L-1.2Y", "316L-2.0Y", respectively. The planetary ball milling process was carried out in a vacuum SS jar at the rotation speed of 200 rpm for 2 hrs with a ball-to-powder weight ratio of 5:1. The milling protocol involved changing rotational direction every 30 mins, followed by a pause interval of 5 mins to avoid overheating. All powders were sieved to 15-44 μm for good flowability.

Table 3-1 Chemical compositions of 316L powder with different oxygen getters purchased from Carpenter Powder Products and planetary ball milled powder (wt.%).

	Fe	Cr	Ni	Mo	C	S	Mn	O	Si	Al	Y
316L	Bal	16.7	10.7	2.29	0.002	0.0006	1.02	0.0384	0.74	/	/
316L-Al	Bal	17.88	14.18	0.14	0.0071	0.0039	1.56	0.0126	0.03	0.85	/
316L (Si, Mn free)	Bal	17.7	13.9	2.84	0.0004	0.0004	0.02	0.044	0.01	/	/
316L-1.2Y	Bal	17.7	13.95	2.84	0.0004	0.0004	0.02	0.078	0.011	/	1.03

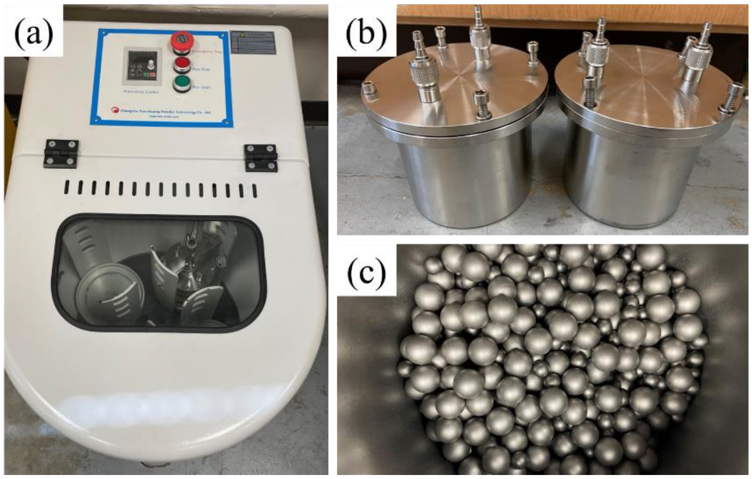

Fig. 3-1 Planetary Ball mill (XQM-2A), vacuum stainless steel mill jar, and stainless steel balls were used.

In Chapter 5, gas-atomized Y doped 316L SS and 316L SS were used as feedstock powder materials. The study focuses on in-situ oxidation to form Y_2O_3 dispersion in the alloy. Table 3-2 shows the chemical composition of these two powders. The two powders were mixed at different ratios to create a range of Y_2O_3 concentrations in the final product (0.5, 1.0, 2.0, and 3.5 wt%), assuming all Y will react with oxygen and generate Y_2O_3. The oxides with lower melting temperature, MoO_3 (high purity, 99.94+%, 13-80 nm, melting temperature, 795 ℃), and Fe_2O_3 (high purity, 99.5+%, 20 nm, melting temperature,1565℃), are used as oxygen carriers to promote oxidation reaction. Considering the oxygen loss during the AM printing process as reported in other's work [100], the pre-estimated oxygen concentration of 1 wt% (10000 ppm) in the final steel was used to prepare ODS steels, which is higher than the oxygen level in the commercial ODS alloys. In contrast to the in-situ reaction, AM ODS steel was also fabricated by laser melting a powder mixture with 2 wt% Y_2O_3+316L SS, where the Y_2O_3 size used is 30-45nm. The same planetary ball milling process mentioned above was carried out to prepare the materials in Chapter 5.

Table 3-2 Chemical composition of Y dopped 316L SS (Y-316L) and 316L SS.

	Mn	Si	Ni	Cr	Mo	Y	Fe
Y-316L	1.42	0.68	9.95	16.46	1.96	1.69	Bal
316L	0.92	0.73	12.9	17.7	2.32	-	Bal

In Chapters 6-8, gas atomized 316L SS powder, 2 wt% Y_2O_3+316L SS powder mixture, and a powder mixture of 3.3 wt% Fe_2O_3+ 1.57 wt% Y+316L SS were used to investigate the effects of PW laser parameter on L-PBF ODS steels and the spattering behavior.

3.2 Laser Powder Bed Fusion Process

Two laser systems were used in this study. A commercial Concept Laser, Mlab Cusing^{TM} system, was used to build samples for study in Chapters 4 and 5. A self-designed L-PBF system equipped with a PW laser was utilized for studies in Chapters 6 and 8.

3.2.1 Continuous Wave Laser

In Chapter 3, L-PBF AM was conducted using a Concept Laser Mlab Cusing^{TM} system (Fig. 3-2) equipped with a 100W Yb: YAG fiber laser, with a wavelength of 1070 nm and a focus diameter of 50 μm.

Fig. 3-2 Concept Laser Mlab Cusing^{TM} system

Printing parameters were chosen based on the optimal density for 316L SS parts, with 90 W laser power, 600 mm/s scan speed, 80 μm hatching space, and 25 μm layer thickness. The baseline study utilized the same printing parameters to fabricate all three materials to compare in-situ oxidation among different materials. To evaluate the effect of laser energy input on oxygen pickup, different scanning speeds were also applied to 316L-1.2Y.

The effects of atmospheric oxygen partial pressure on in-situ oxide formation were studied by adjusting the oxygen level in the shield gas. The atmospheric oxygen level of 0%, 1%, and 2% in the processing environment was achieved by introducing shield gas of argon mixed with different percentages of O_2. The oxygen content in the Concept Laser AM system cannot be safely increased beyond 2%. The oxygen level in the machine was continuously monitored by the Metrotec A19-S oxygen sensor. The shield gas flow rate was maintained at approximately 10-13L/min during the fabrication. The list of samples, processing parameters, and oxygen levels in the atmosphere are shown in Table 3-3.

Table 3-3 Processing parameters and printing environmental oxygen levels investigated in this study.

Sample	Powder	Printing environmental oxygen level (%)	Printing parameters		
			Laser power (W)	Scan speed (mm/s)	Hatching distance (μm)
#1	316L	0	90	600	25
#2		1			
#3		2			
#4	316L-Al	0	90	600	25
#5		1			
#6		2			
#7	316L-1.2Y	0	90	600	25
#8		1		400	
#9		1		600	
#10		1		1000	
#11		2		600	
#12	316L-0.5Y	2	90	600	25
#13	316L-2.0Y	2	90	600	25

In Chapter 5, samples were also fabricated by Concept Laser Mlab Cusing^{TM} system with 90 W laser power, 600 mm/s scan speed, 60 μm hatching space, and 25 μm layer thickness.

3.2.2 Pulse Wave Laser

In Chapters 6-8, samples were fabricated by a custom L-PBF machine (Fig. 3-3) equipped with an IPG model YLR-400-AC ytterbium fiber laser with both CW and PW operation modes. The maximum laser power is 400 W, the laser wavelength is 1070 nm, and the maximum power modulation rate is 50 kHz. The detailed printing parameters are listed in Table 6-1, Chapter 6.

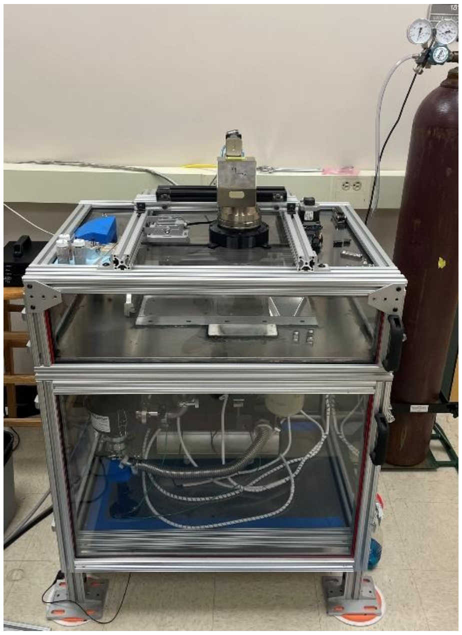

Fig. 3- 3 Custom L-PBF equipped with IPG model YLR-400-AC ytterbium fiber laser.

3.3 Microstructure Characterization

3.3.1 Sample Preparation

For microstructure analysis, as-built or heat-treated samples were sectioned by a Buehler™ Isomet 2000 Precision Saw (Fig. 3-4 (a)) along the build direction. The heat treatments were conducted by a Mellen™ high-temperature furnace, with and without water quench, depending on the requirements. The specimens were mounted with conductive resin by Struers™ LaboPress-3 Mounting Press (Fig. 3-4 (b)) and then polished by a Struers™ Tegrapol 15 automatic polishing machine equipped with Tegraforce-1 head (Fig. 3-4 (c)), starting from 220 grit SiC polishing pad, and followed by 9 µm, 3 µm, and 0.25 µm suspension. The sample preparation was finalized with the Buehler Vibromet-2 Vibratory Polisher (Fig. 3-4 (d)) in 0.04 µm colloidal silica suspension. After vibratory polishing, the surface of specimens was first cleaned with 1% Alconox solution by wiping using a microfiber cleaning cloth to remove the remaining suspension particles. Then the specimens were further washed with ultrasonic cleaner (Fig. 3-4 (e)) for 15 minutes. This preparation method produced a strain-free and scratch-free surface on the relatively soft austenitic stainless steel samples. Electro-etching was sometimes required to reveal the melt pool and cellular/columnar structures. It was conducted at 10% oxalic acid with a Voltage of 5 V and a time of 35 s.

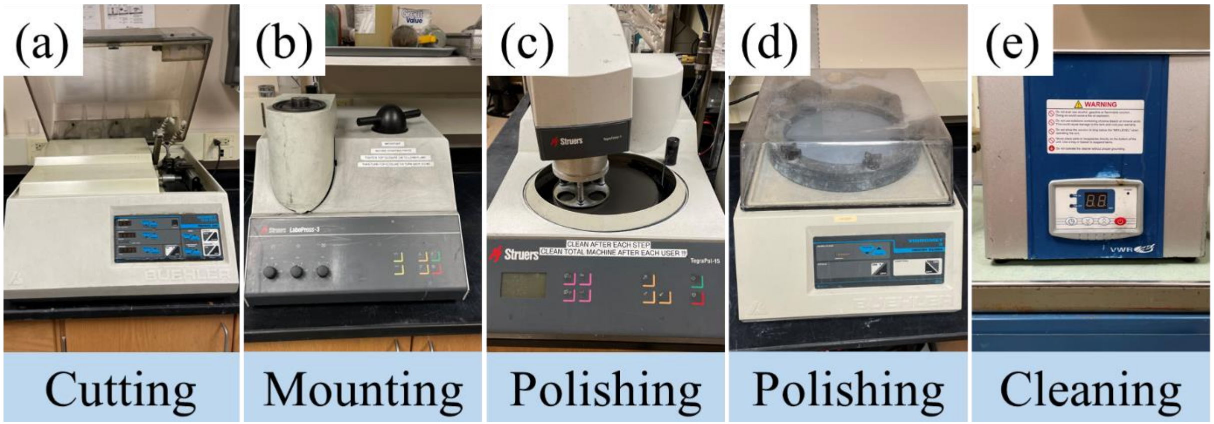

Fig. 3-4 Sample preparation flow chart for microstructure and mechanical analysis.

3.3.2 Density Measurement of L-PBF parts

The optical metallographic images were taken using an Olympus BX51 (Fig. 3-5) microscope, and the material density analysis was performed with ImageJ software. The optical images of the polished specimens were taken by optical microscope with 5 or 10 magnifications depending on the specimen size. The images were then processed by ImageJ software to highlight pore contrast and were converted into binary images for density measurement.

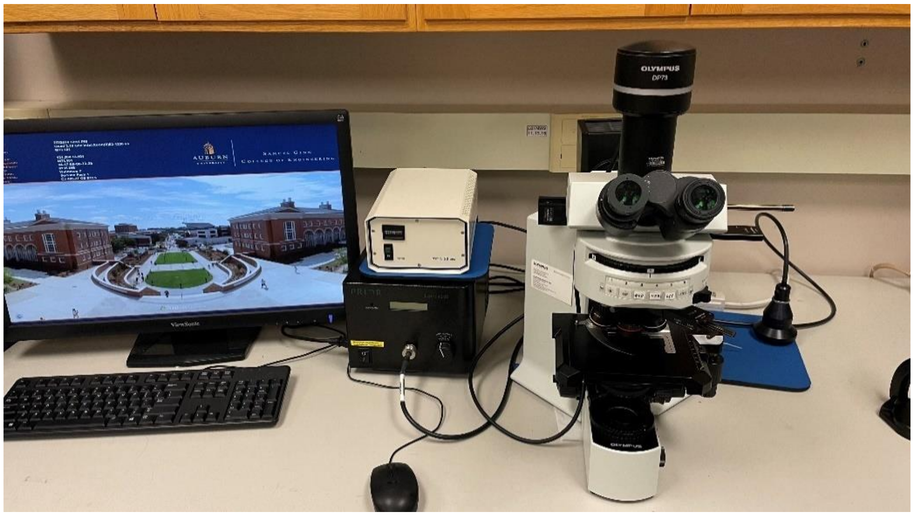

Fig. 3-5 Olympus BX51 optical microscope

3.3.3 Scanning Electron Microscopy (SEM)

SEM characterization was carried out using a JEOL JSM 7000F field emission scanning electron microscope (SEM, Fig.3-6) with Energy Dispersive X-ray Spectroscopy (EDS) detector (Oxford Instruments, Oxford, UK). Backscattered electron (BSE) images were obtained with a yttrium-aluminum-garnet (YAG) scintillator detector at accelerating voltages of 10 kV. The number, density, and size of oxide particles were acquired by using ImageJ software. The chemical composition of different phases was explored by employing EDS point analysis or mapping.

Fig. 3- 6 JEOL JSM 7000F field emission scanning electron microscope.

3.3.4 Transmission Electron Microscopy (TEM)

Transmission electron microscopy (TEM) samples were prepared by focused ion beam (FIB) milling. An FEI NOVA FIB was used to extract the specimens from the regions of interest, and the specimens were mounted onto copper grids for further examination. TEM characterization was conducted in an FEI Osiris FEG-TEM/STEM operating at 200 kV. Bright-field/dark-field imaging and elemental mapping were carried out in the scanning-TEM (STEM) mode, while diffraction patterns for phase analysis were obtained in the TEM mode. Diffraction patterns were then analyzed using GATAN Digital Micrograph and Crystal Maker software. The morphology, size distribution, and chemistry of oxide inclusions were investigated.

3.3.5 Atom Probe Tomography (APT) Characterization

The atom probe tomography (APT) tips were prepared using the standard lift-out and annular milling techniques. Following annular milling, the tips were cleaned with 5 keV and then 2 keV Ga ions to minimize the ion damage near the tip surface. A Quanta 3D field emission gun

(FEG) focused ion beam/scanning electron microscope (FIB/SEM) was used to prepare the APT tips. The APT experiments were conducted on a CAMECA LEAP 4000XHR instrument under laser mode at a specimen temperature of 45–50 K with a laser energy of 50–60 pJ, a repetition rate of 200 kHz, and a detection rate of 0.5%. Datasets from 3 tips were collected for each sample, and the largest one has about 55 million ions. The FIB and APT experiments were conducted at the Microscopy and Characterization Suite (MaCS), Center for Advanced Energy Studies (CAES).

3.4 Mechanical Properties Testing

3.4.1 Vicker's Hardness

Vickers hardness was tested using a DM-400 FT Microhardness tester (LECO Corporation) with an applied force of 1 kg and a duration time of 30 s. Eight indentations were tested on each sample, and the average hardness was reported.

3.4.2 Nanohardness

Nano hardness was obtained using an iMicro nanoindenter (KLA instruments, Fig. 3-7 (a)) with a Berkovich diamond tip by the continuous stiffness method. 25 indents (5×5 arrays) were repeated on each specimen to provide reasonable statistical confidence. Indents were positioned with 50 μm spacing to avoid plastic zone overlap (Fig. 3-7 (b)). The surface effect is overcome once the indent penetrates deeper than ≥ 400-500 nm [101]. The depth limit of indents was set as 2000 nm to get the bulk property.

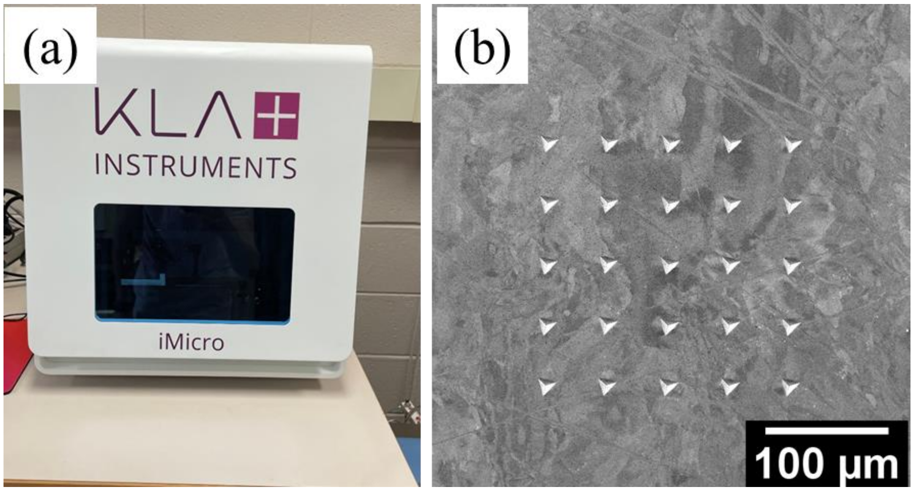

Fig. 3-7 iMicro nanoindenter, KLA instruments (a), and indent array in the sample with 50 μm spacing and 2000 nm depth.

3.4.3 Micro Pillar Compression

Micropillars with diameters of about ~3 μm and aspect ratio (height/diameter) of 2 were prepared by focused ion beam (FIB) using an FEI Helios NanoLab 660 Dual Beam system. In-situ SEM compression tests were performed using a Hysitron PI85 PicoIndenter used the displacement control mode at the strain rate of 10^{-3} s^{-1}. Two micropillars were repeated for each test. EBSD guided pillar selection principle was discussed in section 5.3.3, Chapter 5.

3.5 Spattering

The spattering behavior of CW and PW L-PBF samples was studied by using a high-speed camera, Redlake Motion Scope M2. The distance between the camera and sample is ~30 cm. (Fig. 3-8). The images were taken at 1000 fps with an exposure time of 700 μs. The spattering images of scanning directions both parallel to and vertical to the camera were captured. The sparkline in the images represents the spatter travel distance during the exposure time of 700 μs, and the length of the line are used to estimate the speed of the spatter by using the ImageJ software. At least 50 spatter particles were analyzed, and the average speed value with standard deviation was reported.

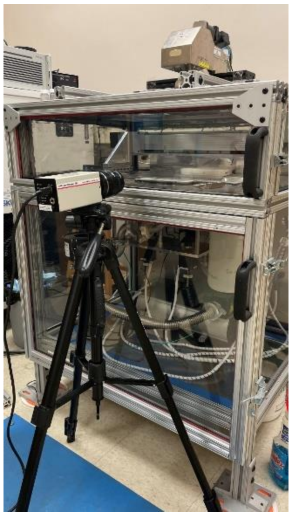

Fig. 3-8 Set up of high-speed camera Redlake Motion Scope M2.

CHAPTER 4

ON THE IN-SITU NANOSCALE OXIDE DISPERSION VIA ATMOSPHERIC OXIDATION DURING LASER POWDER BED FUSION

Argon (Ar) is usually used in the L-PBF as the shielding gas to protect the parts being oxidized for AM materials. But the oxygen residual in the atmosphere was claimed to be responsible for the higher oxygen level in the AM parts [102]. The possible oxidation has usually been regarded as a disadvantage in affecting the toughness [103]. But for ODS steels, the oxide is critical to their mechanical properties. The oxygen in the printing atmosphere could facilitate the oxide formation for certain types of steel when it can be manipulated in a controlled manner. Saeidi et al. [57] reported in-situ oxide formation by printing 316L SS in an Ar atmosphere with 0.1% residual oxygen. Si-rich oxide was observed in the material but with a low volume fraction. Haines et al. [68] proved the increased oxygen level in ferritic Fe-Cr-Al-Ti alloy printed in 0.2% O_2 mixed argon compared to the counterpart printed in pure Ar. Their work shows the potential for the fabrication of ODS steel in L-PBF by adjusting the oxygen level in the shielding gas. But more work needs to be done to understand the efficiency of fabrication of ODS steel by in-situ oxidation. In this chapter, we proposed that the oxygen level in the shield gas, oxygen getter in the alloys with different oxygen affinity, getter concentrations, and printing parameters will affect the oxidation behavior of steel. These factors were systematically studied, and possible limits to fabricated ODS steel by in-situ oxidation are discussed.

4.1 Grain Structure and Defects

Typical grain structures of 316L-Si, 316L-Al, and 316L-1.2Y processed at 1% O_2 atmosphere were shown in Fig. 4-1. There appears to be no significant difference. All the samples exhibited columnar grains along the build direction. The high-temperature gradient along the heat flow during L-PBF produced highly anisotropic microstructures. Grains with a high aspect ratio spanned across several printed layers without being limited by melt pool boundaries. The temperature gradient was dictated by heat removal from the melt pool toward the base plate. But local variations of melt pool geometry are visible. This study applied the same printing parameters and scan strategy to all three materials. The minor differences in the grain structure were caused by the materials' different thermal properties and solidification characteristics. Different from 316L-Si, Al and Y doped 316L SS exhibited increased porosity levels. Besides the lack-of-fusion defects and gas pores caused by the less optimal laser parameters, a large amount of oxide agglomeration sites formed across the material, as shown in Fig. 4-1.

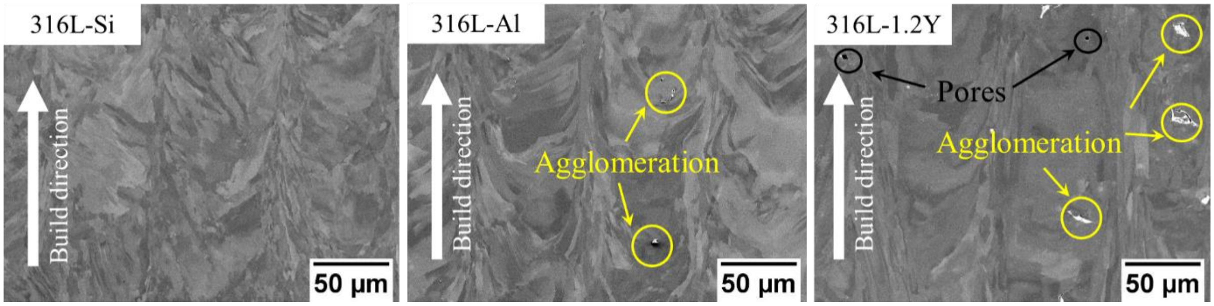

Fig. 4-1 Lower magnification SEM images showing the microstructure of 316L, 316L-Al, and 316L-1.2Y samples printed at 1% O_2 atmosphere, the presence of oxide agglomeration in 316L-Al and 316L-1.2Y samples.

Fig. 4-2 presents the etched micrograph to show the defect structures in 316L-1.2Y printed at 1% O_2. Pores and oxide agglomeration are distributed mainly along the melt pool boundaries.

They can be distinguished by the lighter contrast of oxide agglomeration under SEM, as pointed by the arrows. Interestingly, most lack-of-fusion pores were filled with oxide agglomerates, either entirely or partially. The EDS mapping shows that the oxide agglomerates are mainly yttrium-rich oxides.

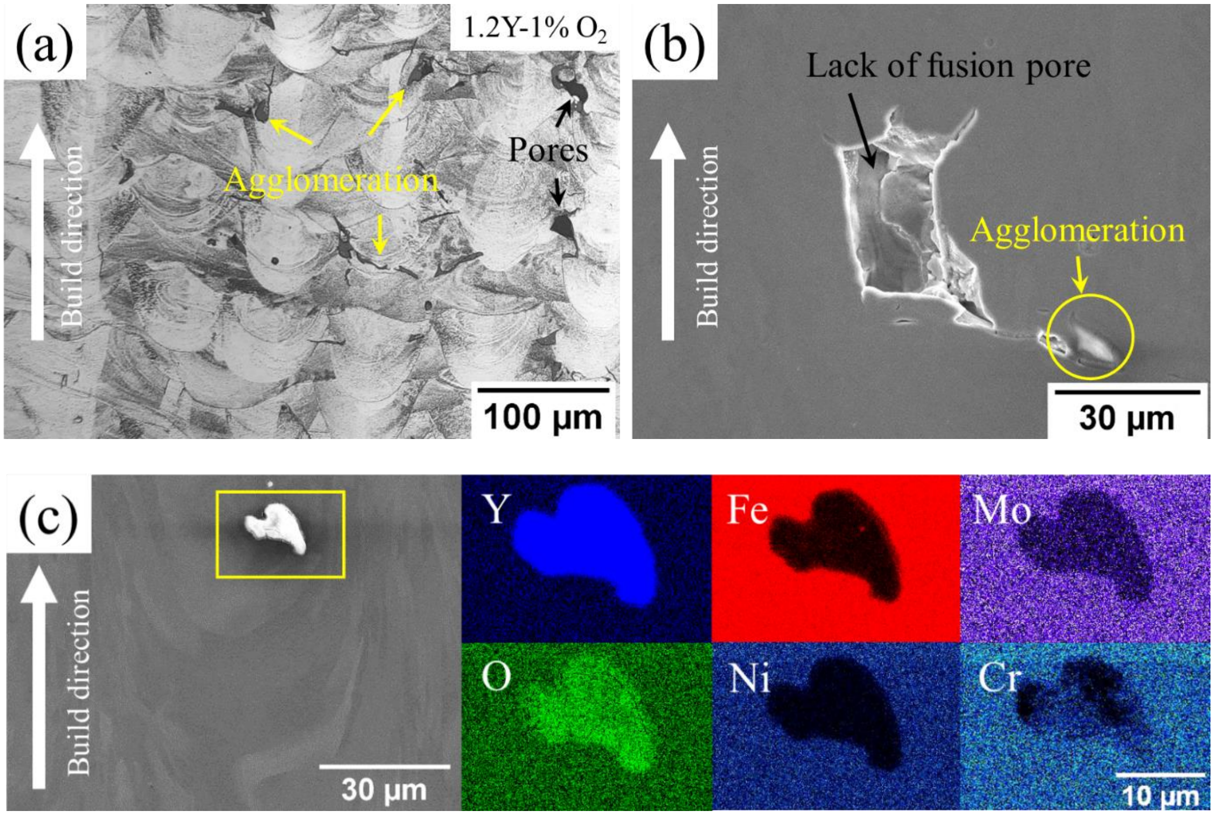

Fig. 4-2 Optical images show defects and agglomeration distributed along with the melt pool boundary in 316L-1.2 Y sample printed at 1% O_2 atmosphere(a), SEM images show detailed defects and agglomeration (b), and EDS mapping of oxide agglomerates (c).

Fig. 4-3 shows the density changes in three materials as the atmospheric oxygen percentage increased. While 316L-Si maintained its high density under all conditions, both 316L-Al and 316L-Y exhibited reduced density with increased oxygen. We emphasize that the laser parameters were optimized for 316L-Si, not for 316L-Al or -Y, which resulted in the discrepancy among materials at 0% O_2. The lower density of 316L-Al or -Y in higher oxygen environments was mainly caused by oxide agglomeration. Y and Al have higher oxygen affinity, resulting in heavier surface oxidation during melting. The melt pool turbulence pushed oxides towards the boundaries to form coarse agglomerates. We suspect the oxide agglomeration might also change the local thermal properties and residual stress upon cooling, promoting the formation of lack-of-fusion defects.

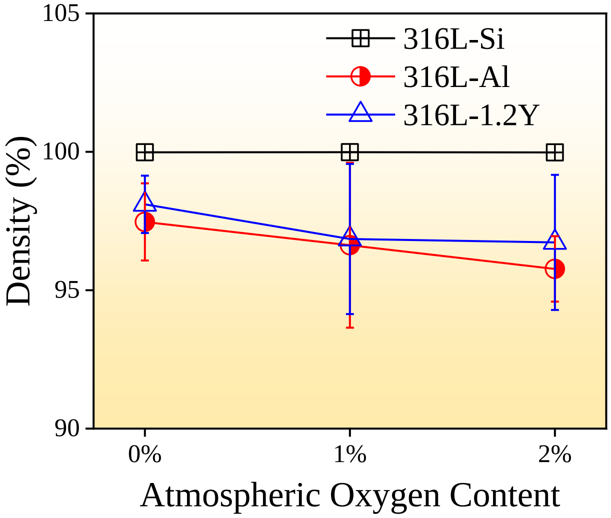

Fig. 4-3 The density of 316L-Si, 316L-Al, and 316L-1.2Y samples were printed at various atmospheric oxygen content.

4.2 Dispersed Nanoscale Oxides

Nanoscale oxides were dispersed uniformly in all three materials. Fig. 4-4 shows the EDS mapping by TEM, illustrating the typical compositions of the nano oxides. AM 316L-Si contains mainly Si and Mn-rich oxides, which have been widely reported in the literature [54,104–107]. In comparison, Al-rich oxides and Y-Si rich oxides formed in the Al-doped 316L SS and Y-doped

316L SS made by L-PBF AM, respectively. Under the as-built condition, the oxides are spherical, resulting from their poor wettability in the melt [57]. Therefore, we believe the nano oxides nucleated from the melt state. The selected area diffraction confirmed that all oxides are amorphous in nature and that the particle was incoherent to the steel matrix. No defects or void was visible along with the particle/matrix interface.

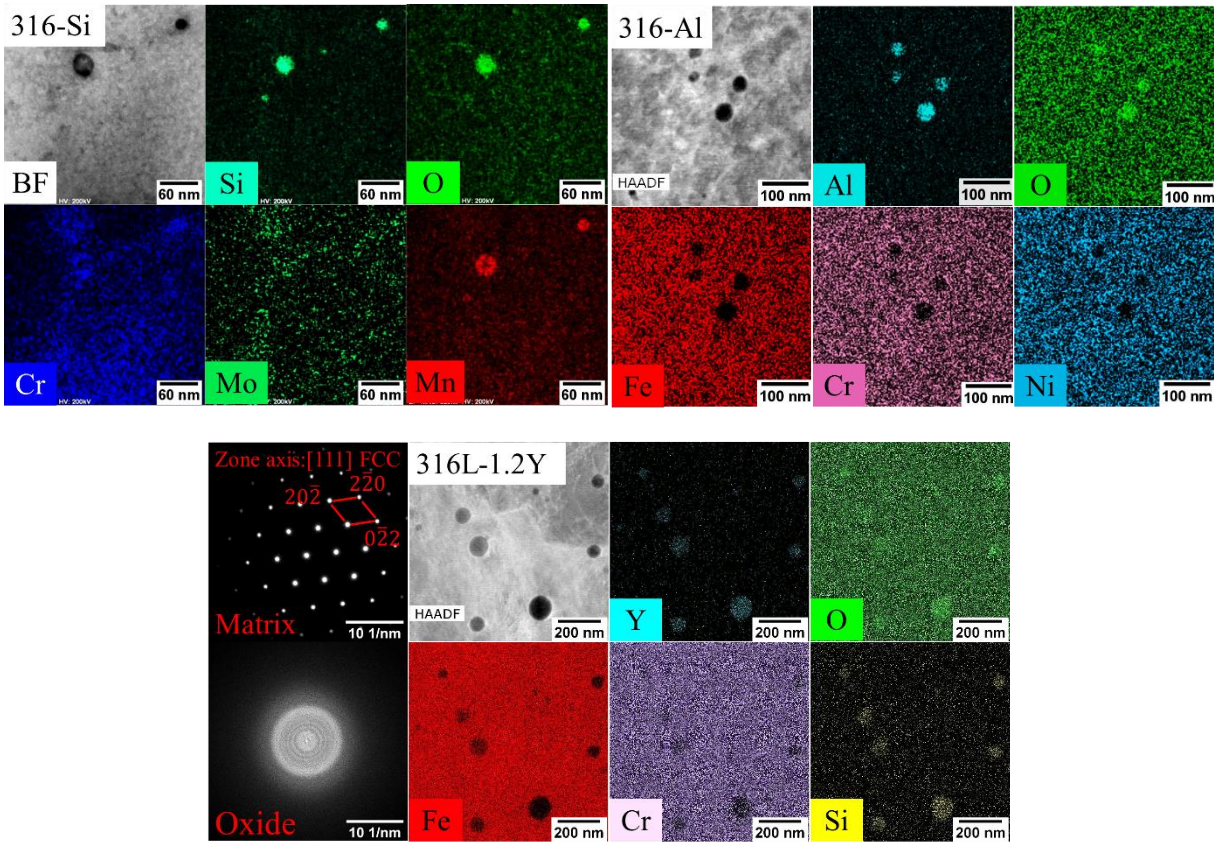

Fig. 4-4 TEM/EDX element mapping of typical nano oxides in as-built AM 316L-Si, 316L-Al, and 316L-1.2Y samples, printed at 1% O_2 atmosphere.

Oxide formation during laser AM is generally controlled by the oxygen affinity of the oxygen getter elements in the alloy. Elements with higher oxygen reactivity, such as Si, Al, and Y, are oxidized first in the melt. For AM 316L-Si, Pu et al. [54] confirmed that the oxygen level of feedstock SS powder is the main contributor to the oxide dispersion by L-PBF. However, with more reactive elements, studies have shown that increased atmospheric oxygen levels could drastically promote oxide nucleation during laser AM [68,108]. The oxide composition is dictated by Gibbs's free energy in the given alloy system. Complex oxides are generally formed, whose compositions highly depend on the type of AM process (mainly thermal history during AM) and the alloy composition[73,109,110].

It is interesting to note that L-PBF typically produces amorphous oxides, regardless of the oxygen reactivity of the getter element. Taking yttria in ODS steel as an example, the conventional casting or powder metallurgy generally produced the crystalline yttria nanoparticles even with a 2-5 nm particle size. Amorphous yttria was commonly reported as being made by thin film deposition. The high cooling rate kinetically favored the formation of the amorphous phase. For instance, the critical cooling rate required for the formation of silicate glass is typically in the range of 10^2 to 10^6 Ks^{-1}. During L-PBF AM, the cooling rate was reported to be 10^6 to 10^7 Ks^{-1}, depending on the laser processing parameters [111]. We emphasize that the amorphous oxides are thermodynamically less stable and will transform to crystalline during post-AM heat treatment.

4.3 Effects of atmospheric oxygen content on oxide formation

The effects of the atmospheric oxygen level on the oxide size and area number density of 316L-Si, 316L-Al, and 316L-1.2Y were reported in Fig. 4-5. Low accelerating voltages, ranging from 7 to 10 kV, were applied to reduce the beam sample interaction volume and increase spatial resolution under BSE mode. The resolution limitation under this condition was 10 nm. Three materials show similar average oxide sizes (Fig. 4-5(a)). However, the size does not change significantly with the atmospheric oxygen level (Fig. 4-5(b)). It is worth noting that the oxide density is increased when switching to stronger oxygen getters like Al or Y. The formation mechanism of nano oxides in AM 316L SS has been explored by different researchers. Most works focused on weak oxygen getter Si, concluding that the increase in the atmospheric oxygen level contributes less to nano oxide formation than the oxygen level of the feedstock powder. The recent development of AM ODS steels using in-process oxidation [68,108] showed the density of nanoscale oxides in AM steel could be further improved by stronger oxygen getters and higher atmospheric oxygen levels; however, the improvement was still mediocre. Our results, shown in Fig. 4-5., are consistent with the reported data in the literature.

The oxygen content changing (baseline are the feedstocks powders) in parts produced in 0%, 1%, and 2% O_2 measured using inert gas fusion, as reported in Fig. 4-5(c). Compared to 316L-Si, the elevated atmospheric oxygen level contributed more oxygen to 316L-Al and 316L-1.2Y. A significant enhancement in oxygen was detected from AM 316L-1.2Y, contradictory to its negligible increase of nano oxides. Also, 316L-Si and 316L-Al can keep absorbing oxygen from a high oxygen atmosphere while 316L-1.2Y reaches a limit of 2% O_2.

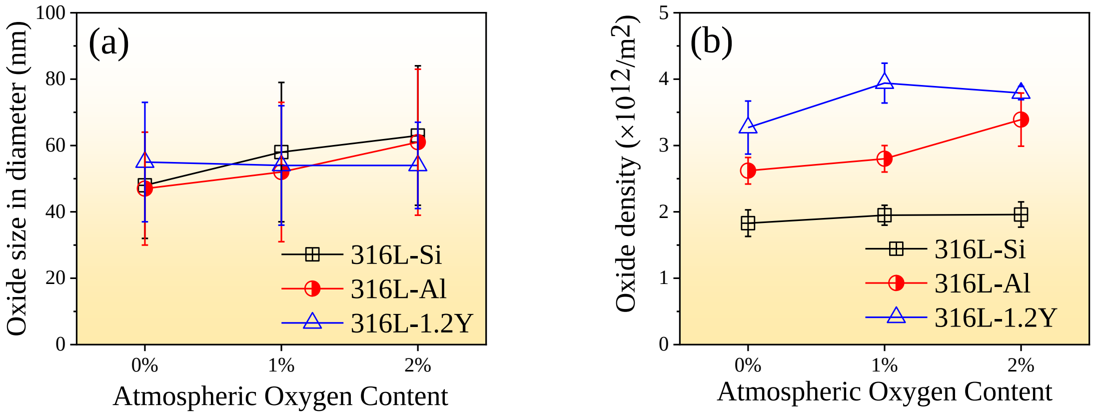

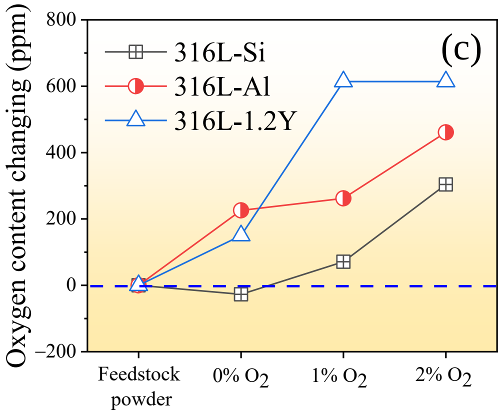

Fig. 4-5 Oxide size in diameter (a), number density (b), and oxygen content change of three different oxygen getters Si, Al, and Y printed at various atmospheres (c) (baseline: feedstock powder).

4.4 Effects of printing parameter on oxide formation and dispersion

Different laser scan speeds, 400, 600, and 1000 mm/s, were applied to 316L-1.2Y at 1% O_2 to reveal the effect of thermal history on oxide formation. When the scan speed increased, as shown in Fig. 4-6, AM 316L-1.2Y presented higher oxide density with a smaller oxide size, and the oxide size distribution shifted to a smaller size. The lower linear energy density (P/v, J/mm) can increase the cooling rate of the melt pool [111] and reduce the in-process heat treatment caused by the thermal cycle from subsequent layers. We note that the total oxide volumetric fraction remains constant with respect to scan speed. The differences in oxide size/distribution in these samples may be caused by the different levels of oxide coarsening, not nucleation. Thus, a faster scan reduced the chance of oxide agglomeration and limited the oxide coarsening during AM. Oxygen measurement from these samples by inert gas fusion was also shown in Fig. 4-6.

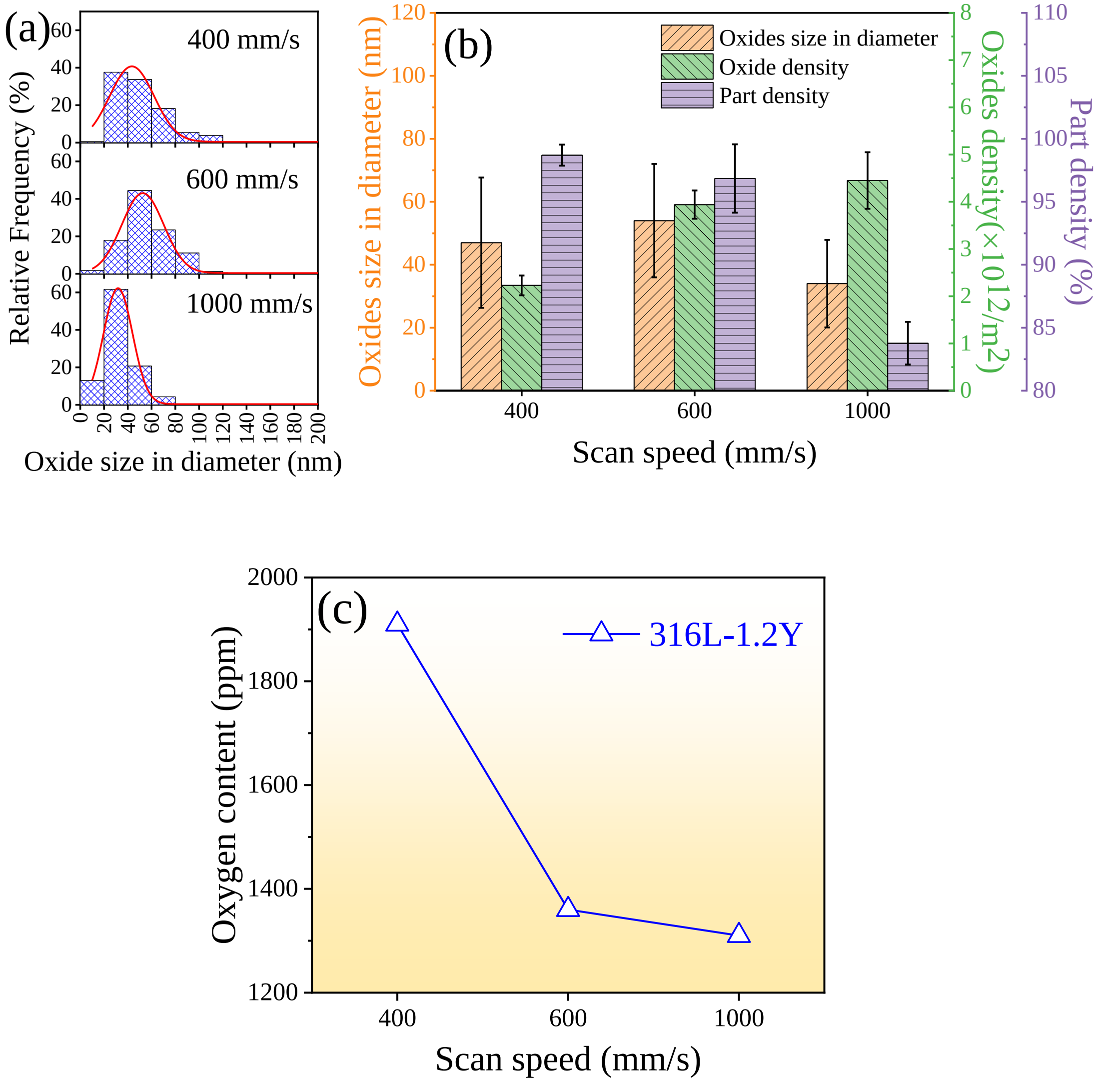

Fig. 4-6 Oxide size distribution (a), average oxide size in diameter, number density and part density (b), and oxygen content(c) of 316L-1.2Y printed at 1% O_2 atmosphere, with different scanning speeds.

The overall oxygen content in the 1000 mm/s sample was ~30% lower than that in the 400 mm/s samples, suggesting a faster scan reduced the reaction time for oxygen pick-up from the atmosphere. The relationship between oxide formation and printing parameters of laser AM was reported in the literature. Eo et al. [72] found that melt pool residence time was not critical in determining oxygen content variation in the AM 316L by laser direct energy deposition (DED) with Ar protection. In their study, the slower scanning speed led to a slightly lower oxide density. Haines et al. [68] also found the oxygen content in the AM Fe-Cr-Al-Ti stainless steel decreased with an increase in laser energy. Our study demonstrated that printing parameters could significantly alter oxidation kinetics and oxide dispersion if higher atmospheric oxygen levels and more reactive elements are involved. It is worth noting the overall material density reduces as the scan speed increases. Faster scan speed will generally induce more lack-of-fusion defects.

4.5 Effects of oxygen getter concentration on oxide formation and dispersion

Fig. 4-7 demonstrates how the concentration of an effective oxygen getter affects the oxide size and density. No visible change is observed in oxide size/distribution with the Y increase from 0.5 to 2 wt.%. Higher oxide density in 316L-2.0 Y samples suggests that adding more reactive elements increases the efficiency of oxygen pick-up from an oxygen-contain printing environment. Unlike the earlier studies using 316L-Si [54], this study confirms that the oxygen transfer from the atmosphere to the melting pool could dominate in-melt pool oxidation when more efficient reactants are involved. On the other hand, the part density dropped significantly as the function of Y content. A careful investigation of defect types suggests the defect formation was promoted by more oxide agglomeration during printing. Clearly, excessive oxide agglomeration can take place when oxide density is beyond a certain threshold.

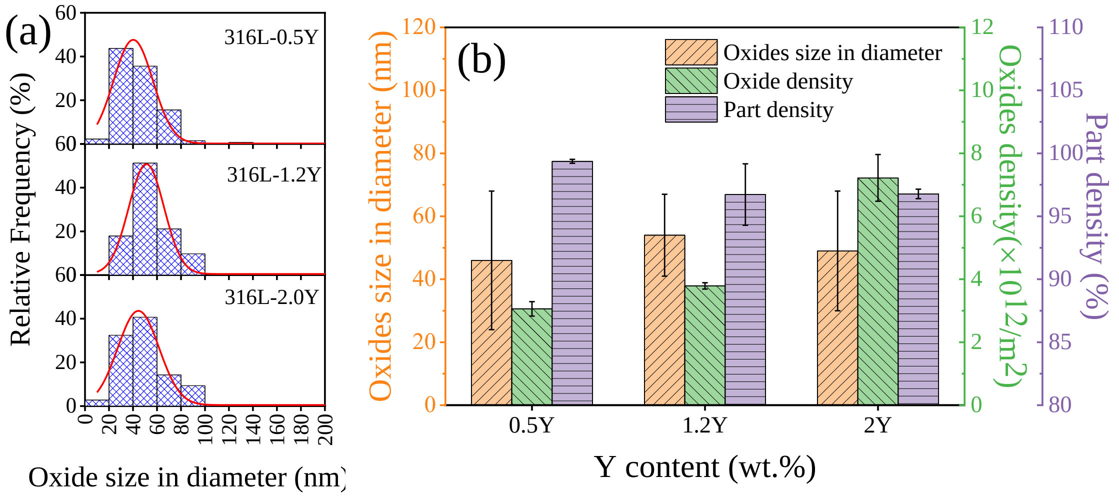

Fig. 4-7 Oxide size distribution(a), average oxide size in diameter, number density, and part density(b) as the function of Y content printed at an environmental oxygen level of 2%.

4.6 Hardness

Vickers hardness measurement was performed on 316L-Si, 316L-Al, and 316L-1.2Y samples produced in various oxygen atmospheres, as shown in Fig. 4-8. A slight difference in hardness was observed in all three samples fabricated in selected atmospheric oxygen levels. We employed a dispersed barrier hardening model to predict the hardness change based on the oxide measurement. The estimated obstacle-induced changes in yield strength ($\Delta\sigma_y$), given as [112]

$$\Delta\sigma_y = M\alpha\mu b/\lambda \approx M\alpha\mu b\sqrt{Nd}$$

Where M is the Taylor factor (3.06 for FCC polycrystals), α is the strength factor (0.86 for spherical particles [112]), μ is the shear modulus of the matrix (78 GPa for 316L), b is the Burgers vector (0.258 nm [113]) and λ is the inter-obstacle spacing, a function of particle size d and number density N . $\Delta\sigma_y$ for 316L-1.2Y printed at 0% and 1% O_2 atmosphere are 77.23 MPa and 71.01 MPa, respectively. The difference between these two materials was only ~6 MPa. The increment in yield strength is generally proportional to hardness:

$$\Delta\sigma_y = \frac{1}{3}\Delta HV(MPa) = \frac{9.81}{3}\Delta HV(kgf/mm^2).$$

The negligible difference ~2 $HV(kgf/mm^2)$ cannot be revealed from results. Due to the alloying differences, the removal of Mo from 316L-Al and Mn from 316L-1.2Y could also lead to lower hardness than AM 316L-Si. This result was also in accordance with Bogachev et al. [114], who stated that 0.3wt% of Y_2O_3 nanoparticles in an ODS steel matrix is too low to influence the microhardness of the material.

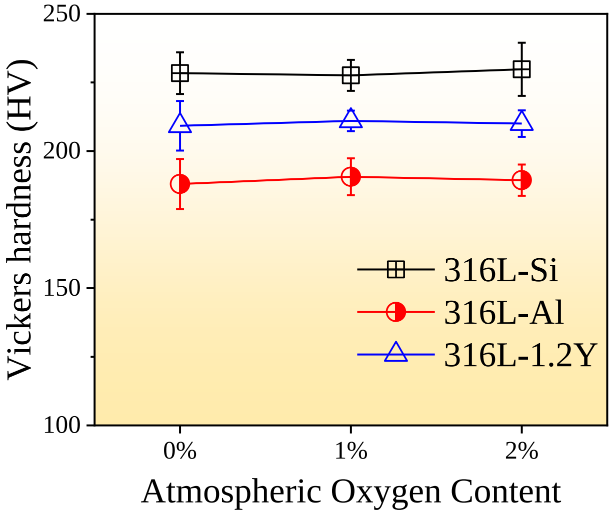

Fig. 4-8 Vickers hardness of three different oxygen getters Si, Al, Y printed various atmospheres.

4.7 Discussion

The study confirmed that the formation and dispersion of nano oxides through in-melt-pool oxidation could be significantly improved by selecting more reactive elements, reducing the melt pool's liquid residence time, and increasing both atmospheric oxygen level and the content of effective oxygen getters in the alloy. However, the data also revealed a competitive relationship between the dispersion of nanoscale oxides and oxide agglomeration under a realistic printing environment. This section will discuss the controlling mechanism, quantify the reaction steps, and provide our perspectives on employing in-situ oxidation during laser AM to manufacture ODS alloys.

4.7.1 Mechanistic Picture of Atmospheric Oxidation in Laser Melt Pool

Atmospheric oxidation in molten metal has been well described for continuous casting or welding. The theory originated from understanding how oxygen gas interacts and dissolves in liquid metal. For the oxidation of molten steel, the reaction generally consists of a few steps [115], including (1) the diffusion of O_2 towards the gas-liquid interface, (2) the dissociation of O_2 into singular atom [O] under the plasma induced by the heat source, (3) the direct oxidation at the liquid surface, (4) the diffusion of oxygen atom [O] through the oxide film, (5) the chemical reaction at the oxide-metal interface, (6) the diffusion of [O] in the liquid steel, (7) the chemical reaction between [O] and oxygen getters in the liquid steel, (8) the diffusion of oxygen getters in the liquid steel. This oxidation mechanism assumes that the continuous oxide layer is readily formed across the whole melt pool when exposed to the air. Therefore, oxygen diffusion through the oxide layer is considered the rate-limiting step.

However, in L-PBF AM, the reaction steps can be different, considering the highly localized energy input, unstable melt pool, and fast heating and cooling rate. Fig. 4-9 illustrates the proposed mechanistic explanation of oxygen-metal interaction during L-PBF AM. The localized energy input by laser promotes the O_2 dissociation, resulting in high-energy plasma above the melt pool surface Fig. 4-9(a). The physicochemical behavior of a plasma-metal interface is significantly different from that of a gas-metal interface, which enhances the local solubility of oxygen [116] and promotes diffusion kinetics across the interface. On top of the melt pool surface, metallic elements with higher oxygen affinity, such as Si, Mn, Cr, Al, and Y, were selectively oxidized.

First, a thin oxide film will form on the melt pool surface, as shown in Fig. 4-9(b). Then the dynamic Marangoni convection inside the melt pool accelerates the diffusion and re-distribution of dissolved oxygen and getter elements like Y and Al, promoting nano oxide dispersion. The convection can also break the oxide film, push oxides toward the melt pool boundaries and generate oxide agglomerations, as shown in Fig. 4-9(c). Laser AM possesses advantages in enhancing the rate of oxygen transfer across the gas-liquid interface. But the oxide formation in the melt pool is more sensitive to the physical properties of the melt pool. The oxidation kinetics and oxide dispersion are sensitive to the gas-liquid interaction time, the reactivity of the elements, oxygen content in the shield gas, and local turbulence [68]. A semi-continuous slag layer can form on the melt pool surface and will impede the oxygen diffusing into the melt pool. Moreover, if the slag and/or oxide agglomeration on the previous layer cannot be fully dissolved into the successive layer, it could induce more defects inside the sample.

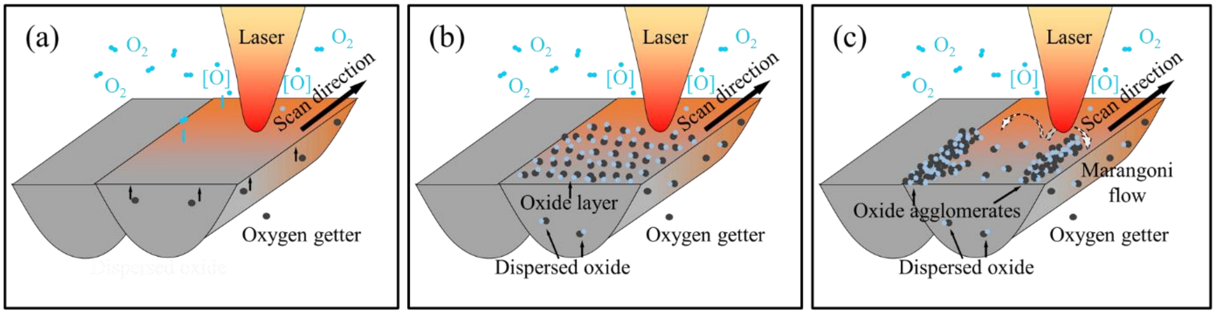

Fig. 4-9 Schematic of the interactions between laser, gas, and melt pool. In-situ oxidation by the dissolution of O_2 as atomic oxygen diffused into melt pool during L-PBF.

4.7.2 Oxide Slag Formation on the Melt Pool Surface

Fig. 4-10 shows the cross-sectional view of the surface oxide layers of three materials printed in a 1% O_2 environment. Surface slag layer formation was reported for laser DED processes involving an oxygen-containing atmosphere [72,117]. Compared to laser DED, L-PBF AM generally presented one to three orders of magnitude higher cooling rate, thus reducing the time for oxidation reaction during manufacturing. Haines et al. [68] discounted the possibility of forming surface oxide slag on the melt pool surface based on their fabrication of Fe-Cr-Al-Ti steel in the oxidizing atmosphere by L-PBF. This conclusion is consistent with our observations from AM 316L-Si printed in a high O_2 environment, as shown in Fig. 10.

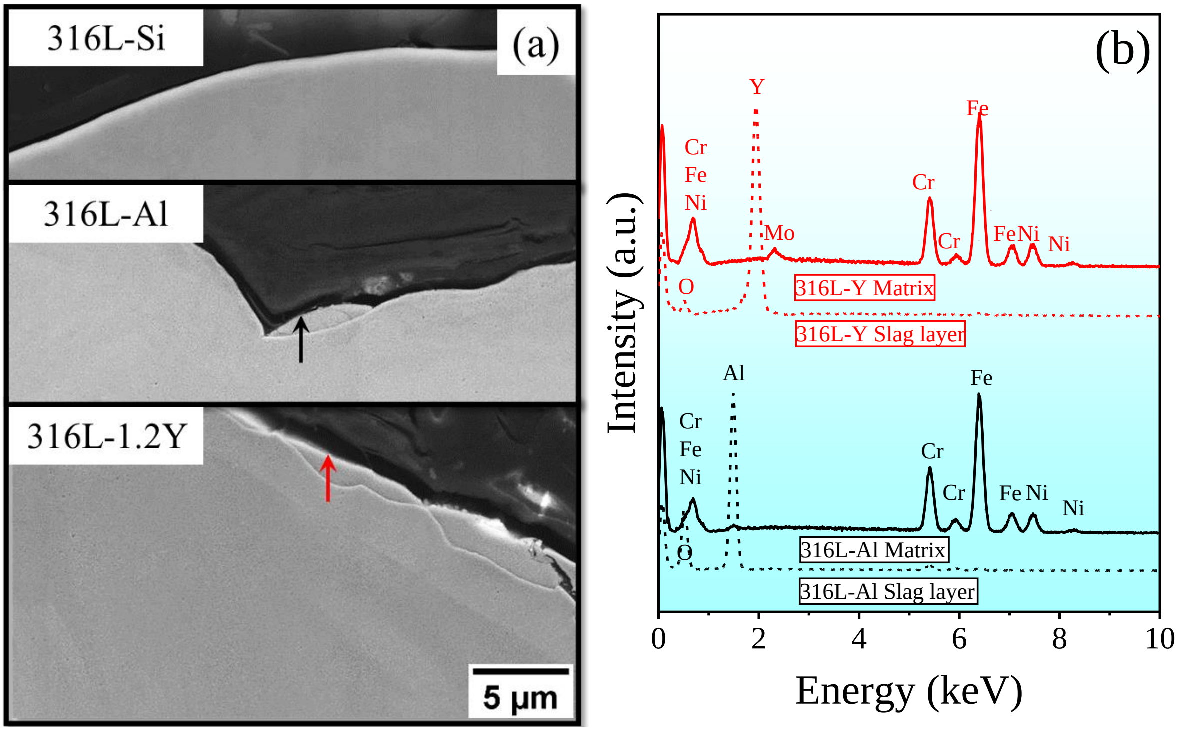

Fig. 4-10 Oxide slag layer formation on the melt pool surface of 316L-Si, 316L-Al, and 316L-1.2Y samples printed at 1% O_2 atmosphere (a), and EDS point analysis show the composition of the slag layer (agglomeration) (b).

In comparison, AM 316L-Al SS shows surface oxides accumulated near melt pool boundaries, with an EDS scan confirming they are Al-rich oxides (43.67% Al, 36.66% O, 5.5 % Cr, 11.05% Fe,1.24% Mn, 1.88%Ni, in wt.%). With more reactive AM 316L-1.2Y SS, a semi-continuous oxide slag layer enriched with Y formed in a 1% O_2 environment. EDS confirms that the stoichiometric ratio of Y:O is close to Y_2O_3, the same as the oxide agglomerates found in the steel matrix.

Fig. 4-11 shows all three materials' top-view EDS maps of the printing surface. In AM 316L-Si SS, the indication of strong oxidation on the melt-pool surface was only visible along the melt pool boundaries. This observation is consistent with our earlier work [54], concluding that only minor regional oxidation occurs in the melt pool of AM 316L-Si during L-PBF AM. As arrowed in the figure, the re-introduction of spattered powders was also found to contain a higher amount of oxygen. However, its contribution to surface oxidation is still negligible. In comparison, AM 316L-Al SS presents a higher fraction of Al-rich surface oxide on the melt pool surface. The surface oxide, visualized in the form of discrete black spots, is located along the melt pool boundaries. With more reactive yttrium in AM 316L-1.2Y SS, ~50% of the melt-pool surface is covered with thick Y-rich oxide originating from the melt pool boundaries. A thin oxide layer was observed in the melt-pool interior.

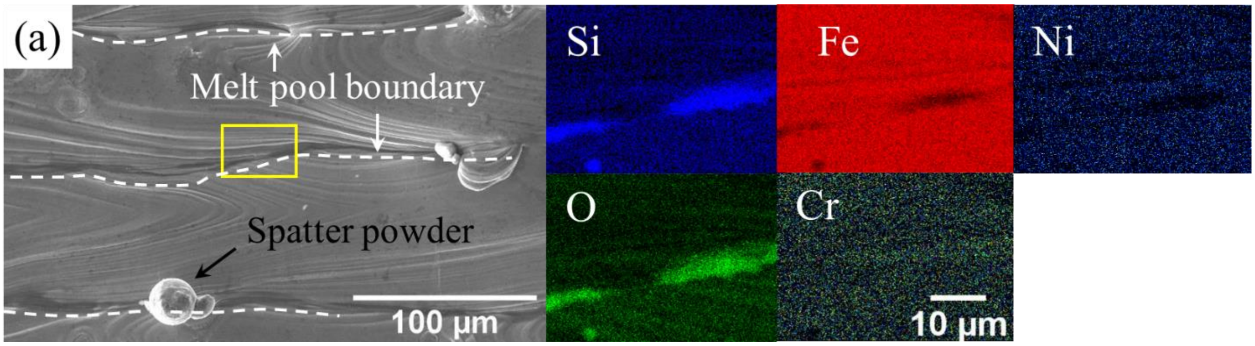

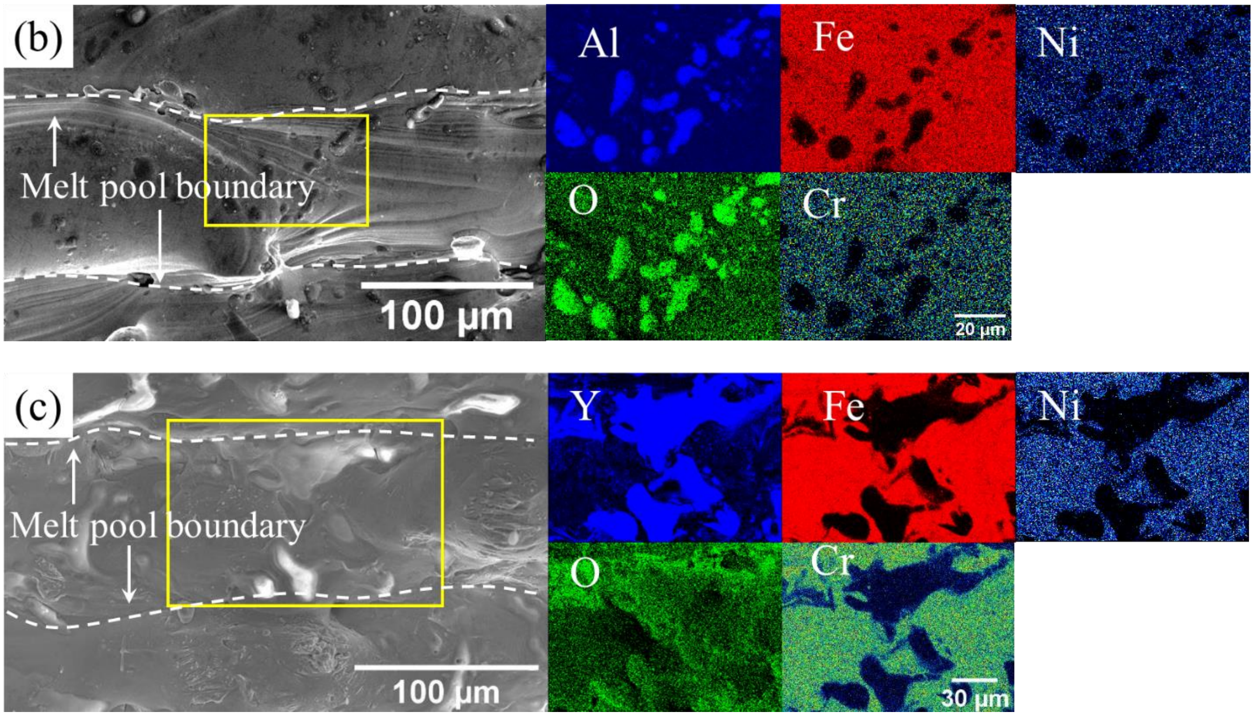

Fig. 4-11 Surface oxidation and oxide slags formation on the melt pool surface with different oxygen getters (a) Si; (b)Al; (c)Y, samples were printed at 1% O_2 content.

These results suggest that surface oxidation can contribute greatly to the overall oxide build-up in the product when more active oxygen getters are involved. In AM 316L-Al and AM 316L-1.2Y, we observed a mixed-mode of surface oxidation with a thin oxide film on the melt pool surface and a thick oxide layer near the melt pool boundaries, in contrast to the continuous surface slag found in the casting process. At the same time, the differences in the oxide coverage and thickness still exist, depending on materials and processing conditions. In L-PBF, the melt pool dynamics are intense and result in turbulence due to Marangoni flow. The liquid instability caused by the turbulence constantly breaks apart the surface oxide layer, resulting in the further exposure of the melt to air. This process contributes to accelerated surface oxidation (more slagging) and more oxygen diffusion across the melt/air interface. Surface slagging and oxygen diffusion are the competing processes to consume the total oxygen supply provided by a given environment, meaning the faster surface oxidation can limit the oxygen diffusion across the interface and produce less efficient nano oxide formation.

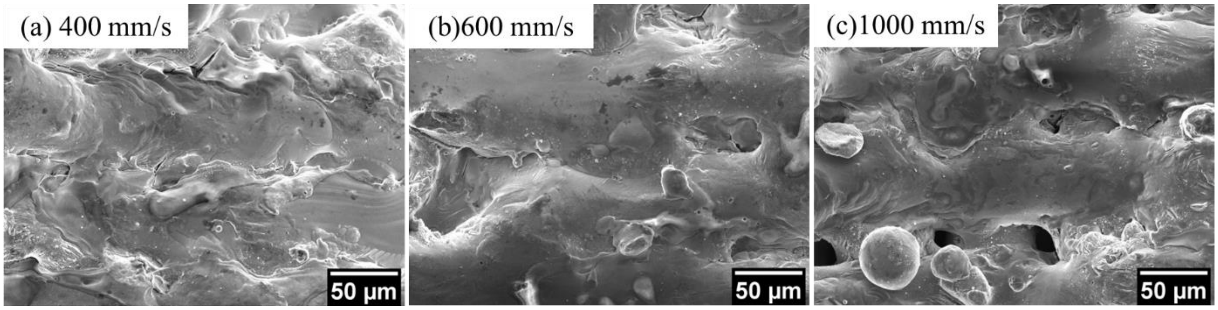

Fig. 4-12 Surface oxidation and oxide slags formation on the melt pool surface in 316L-1.2Y with different scanning speed, (a) 400 mm/s, (b) 600 mm/s, (c) 1000 mm/s, samples were printed at 1% O_2 atmosphere.

Fig. 4-12 shows the melt pool surface of 316L-1.2Y printed with different scan speeds. An increase in scan speed (decrease of liquid melt pool exposure time) led to a great reduction in the oxide slags formation. This is consistent with the oxygen content analysis (Fig. 4-6(c)). However, the oxide volume fraction among these samples is similar, suggesting dispersed oxygen intrusion into the matrix is barely affected, although low scan speed enables longer diffusion time.

We emphasize that the surface oxidation rate highly depends on the type of reactive elements and atmospheric oxygen level. AM 316L-Al presented a continuous increase in nano oxide density as a function of oxygen content in the shield gas, while AM 316L-1.2Y showed a slight drop in nano oxide density at a 2% O_2 environment. The thick surface oxide slag (shown in Fig. 4-11 (c)) formed in AM 316L-1.2Y inhibited the oxygen diffusion at the melt/air interface.

4.7.3 Oxide Agglomeration in Defects

Oxides agglomeration in AM ODS alloys is commonly observed [62,70,117,118]. In AM ODS alloys, the added oxides would agglomerate in the melt pool due to the bad interface between oxide and matrix. In addition, the lower density of oxide will float onto the melt pool surface and form slag layers. Oxide agglomeration can take away a large amount of oxygen from the matrix and reduce the oxide density in AM ODS steels. In our study, XCT was used to quantify the volume fraction of the oxide agglomerates in the AM part. The sample with the size of 1×1×2 mm and a total volume of 2 mm^3 was characterized by X-ray computed tomography unit ZEISS Xradia 620 Vesra. Tube voltage was set to 130 kV and current to 133 μA to ensure sufficient sample penetration. The voxel size was set to 2.28 μm with 2400 total amount of projections. The reconstruction of frames was done using the Scout-and-Scan Control system Reconstructor. Porosity and agglomeration analysis was performed in VG Studio MAX 3.5. Both porosity and agglomeration analyses were done in the VG porosity module. Pores and agglomerations were separated and calculated separately by thresholding them by volume, sphericity, and compactness simultaneously to ensure the best possible separation.

Fig. 4-13 shows how oxide agglomerates were extracted from the bulk specimen by XCT. The sample is a 316L-1.2Y sample printed at a 1% O_2 atmosphere. Fig. 4-13(a) is a 2D transverse cross-section from the XCT reconstructed part. The presence of agglomeration (grey) and pores (black) can be observed. These features have also been verified from optical and SEM characterization. Fig.4-13(b) shows that the agglomeration (with color) can be successfully separated from pores (black). Fig. 4-13(c) and Fig. 4-13(d) shows the 3D distribution of agglomerates and whole defects (agglomeration and pores). They demonstrate that the agglomeration follows a periodical pattern, which is typically caused by insufficient energy input [119].

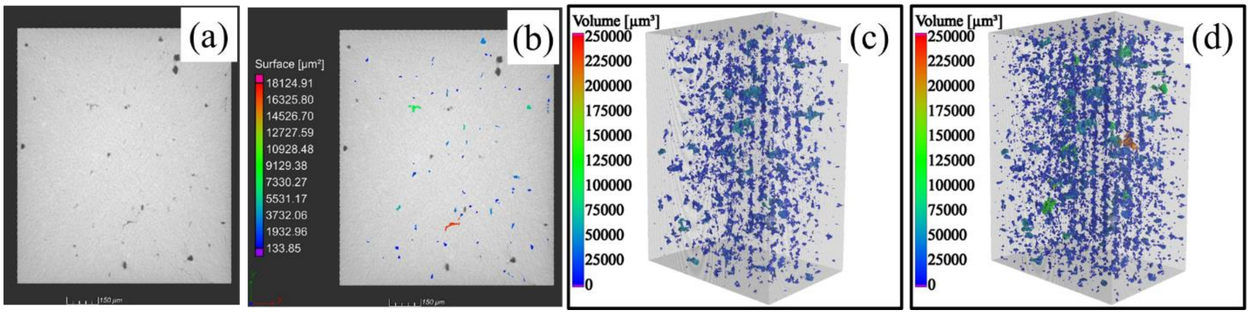

Fig. 4-13 X-Ray CT scanning of a 316L-1.2Y sample printed at 2% O_2 atmosphere. (a) 2D, transverse cross-section of the volume from the XCT reconstructed part (b) oxide agglomerate determination via Volume Graphic 3.4; (c) oxide agglomerate and (d) all defects distribution in the parts.

The volume fraction of overall defects (agglomeration and pores) in AM 316L-1.2Y printed in 1% O_2 atmosphere is ~3.3%, and the volume fraction of oxide agglomerates is ~0.71%. The calculated oxygen content in this sample is ~950 ppm if we assume the stoichiometric ratio of Y:O in the agglomerate follows that in Y_2O_3 (from EDS point analysis). The measured oxygen content in this sample (Fig. 4-5) was reported at ~1360 ppm, and we conclude that only 410 ppm oxygen was presented in the form of nano oxides in the steel matrix. This value is significantly less than the ODS material PM 2000 (1080 ppm) and MA 950 (910 ppm) processed by conventional methods [120]. The oxygen trapped in the agglomerates reduced the oxygen transfer efficiency for in-situ nano oxide dispersion during L-PBF AM, even when more-than-enough oxygen can be supplied from the atmosphere.

4.8 Conclusion

In the present study, the in-situ nano-oxide formation during L-PBF in AM 316L SS alloyed with different elements Si, Al, and Y was investigated by utilizing a high oxygen printing atmosphere. The oxide dispersion and melt pool oxidation behavior are affected by the oxygen content in the shield gas, the oxygen getter in the steel, and printing parameters. The dispersed oxide density in AM 316L-Si is not sensitive to the oxygen content in the printing atmosphere, with a density of $\sim 1.8\times 10^{12}/\mathrm{m}^2$. Higher oxygen affinity elements Al and Y promote oxide formation. As a result, the oxide density in 316L-Al and 316L-1.2 Y increases as oxygen content increases. Up to ~2 times, higher oxide density than that in 316L-Si can be achieved in these two samples. The oxidation behavior of 316L was affected by different oxygen getters. The melt pool surface of 316L-Si was barely oxidized, while a thicker oxide layer was observed on 316L-1.2Y samples. Shortening/reducing liquid phase duration using a higher scan speed would help refine the dispersed oxide and increase the oxide density. The undesired slag layer can hinder the oxygen pick-up from the printing atmosphere and deteriorate the part density of L-PBF ODS steels. In-situ reactive AM in an oxygen-containing environment did not produce desired nano oxide dispersion to improve the mechanical property.

CHAPTER 5

IN-SITU SYNTHESIZED OXIDE DISPERSION STRENGTHENED ALLOY WITH EQUIAXED GRAIN STRUCTURE AND EXCELLENT THERMAL STABILITY BY ADDITIVE MANUFACTURING

It has been shown that melt pool surface oxidation hinders the dispersed oxide formation in the matrix by introducing a gas-oxygen donor (oxygen in the shielding gas). Other efficient oxygen sources for L-PBF ODS should be considered. Significant oxygen loss in the L-PBF ODS steel observed by Zhong et al. [100] also demonstrated the incapability to fabricate ODS steel with high oxide density by using a mixture of ex-situ Y_2O_3 particles with 316L SS powder. We believe the laser can not fully melt the Y_2O_3 particles instantly due to their high melting temperature. Floating, agglomeration, and spattering of the unmelted particles will cause oxygen loss during the L-PBF process. To increase the oxide density and improve the mechanical properties, low melting point solid-oxygen donor, Fe_2O_3, or MoO_3 nanoparticles, were mixed with pre-alloyed 316L-Y SS steel powder. We believe the dissociation of the solid-oxygen donor and reaction between oxygen and Y that occurs in the liquid melt will increase the oxide density in L-PBF ODS steel. The effects of pre-alloyed yttrium concentration on the mechanical properties and thermal stability of in-situ reacted ODS steel were investigated. Stabilized cellular boundary by dispersed oxides was believed to contribute to the excellent thermal stability of in-situ reacted AM ODS steel.

5.1 Microstructure

5.1.1 Feedstock Powder

Oxides with low melting point, MoO_3 and Fe_2O_3, are replacing oxygen containing argon as the solid-phase oxygen donor for in-situ reactive AM. Feedstock powders were prepared by mixing nano powders of solid-phase oxygen donors and gas atomized steel powders via low-energy planetary ball milling, as shown in Fig. 5-1.

Fig. 5-1 Feedstock powder for in-situ reacted AM ODS steel

Unlike the conventional high-energy MA process, low-energy ball milling can mix powders uniformly at a lower rotation speed in a short time. This process can maintain the spherical shape of the powder and maintain a good flowability for the L-PBF process. The donor oxides uniformly decorate the powder surface and serve as an oxygen source for in-situ oxidation during the melting process. The loss of oxygen in AM ODS steel was reported [100]. In this study, 1 wt% O (10000 ppm oxygen, equivalent to 3 wt% MoO_3 and 3.3 wt% Fe_2O_3) was added to the feedstock powder, and theoretically, it can form for up to 3.5 wt% Y_2O_3 in the matrix. The oxide (weight percentage) in the AM ODS steel was controlled by adjusting the Y content in the feedstock powder. Samples of pre-alloyed Y concentrations of 0.39, 0.79, 1.57, and 2.75 wt% (with 0.5, 1, 2, and 3.5 wt% Y_2O_3) were studied in this work. These oxide percentages were the calculated values based on the assumption that oxygen from the donor was completely utilized during the reaction.

5.1.2 Effects of Y concentration on oxide nucleation and dispersion

Fig. 5-2 shows the oxide (the black dots in the images) morphology and distribution in the L-PBF ODS steel (oxide donor Fe_2O_3) with different pre-alloyed Y concentration in the SS powder. In the as-built condition, spherical oxides are uniformly distributed in the matrix in all samples. In as-built 0.39 and 0.79 wt% Y samples, submicron oxides can be observed, but most oxides were with an average size of ~50 nm. In comparison, submicron oxides were barely observed in 1.57 and 2.75 wt% Y samples. After heat treatment at 1100℃ for 10 hrs, oxide coarsening was evident in 0.39 and 0.79 wt% Y samples, but not 1.57 and 2.75 wt% Y samples. In the SS for this research, the reacting priority of elements with oxygen was determined by their oxygen affinity. The element with the highest oxygen reactivity in the melt will first be oxidized. Due to the high oxygen content (1 wt%, 10000 ppm) in the feedstock powder, once the Y in 0.39 and 0.79 wt% samples were fully oxidized, the excess oxygen could further react with Si, Mn, and Cr to form different types of oxides. Y_2O_3 and its variants are the desired oxide for designing ODS alloys due to its high stability at elevated temperatures. In comparison, Si- and Mn-rich oxides were reported to be metastable during laser AM, and post AM heat treatment. They are prone to oxide coarsening and can be transformed into the $MnCr_2O_4$ spinel phase [55]. The bimodal oxide types in 0.39 and 0.79 wt% samples suggested that the ratio between yttrium and oxygen is crucial for AM ODS steel made by the in-situ reaction. The 1.57 wt% sample was selected for further microstructure and mechanical characterization.

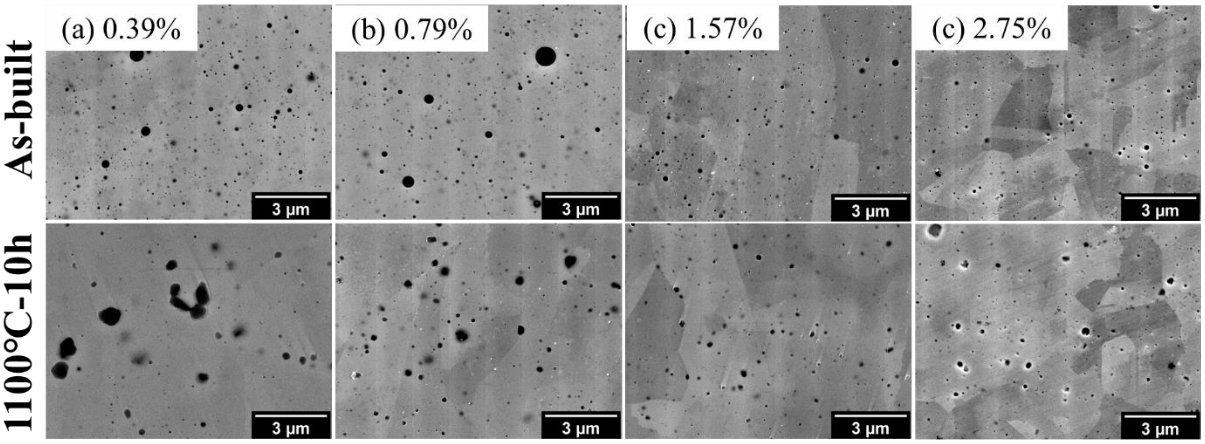

Fig. 5-2 Effects of the pre-alloyed Y concentration on the microstructure of L-PBF ODS steel. (a) 0.39 wt%, (b) 0.79 wt%, (c) 1.57 wt% and (d) 2.75wt%. (Corresponds to 0.5, 1, 2, and 3.5 wt% Y_2O_3, respectively)

5.1.3 Grain Structure

Fig. 5-3 shows the EBSD grain misorientation maps of the as-built AM 316L SS, as-built and heat-treated (1100°C-50 hrs) 2 wt% Y_2O_3 ODS samples (1.57 wt% Y+3.3 wt% Fe_2O_3). Microstructure heterogeneity was present in the pure AM 316L SS, with the coarse columnar grains oriented along the build direction. The material was primarily textured along <001> due to the directional solidification by laser AM. The unique microstructure features of AM 316L SS as compared to conventional 316L SS, along with its anisotropic properties, have been well documented elsewhere [121]. Compared to AM 316L SS, AM ODS SS with 1.57 wt% Y addition showed refined grain structure with random texture. The epitaxial grain growth, which is normally observed in laser AM, was inhibited. The material showed an equiaxed grain size averaged at ~5.8 μm. AM ODS SS also showed superior thermal stability. After being heat-treated at 1100°C for 50 hrs, no grain growth was observed. The average grain size was ~5.4 μm.

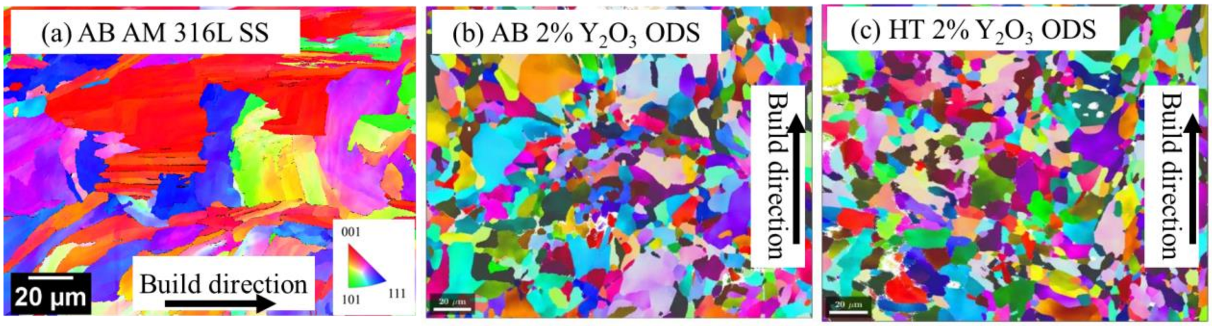

Fig. 5-3 Grain structure of the as-built 316L SS (a), as-built (b), and 1100°C-50h heat-treated (c) in-situ 2 wt% Y_2O_3 ODS sample (1.57 wt% Y+ 3.3 wt% Fe_2O_3).

5.1.4 Oxide Morphology and Distribution in AM ODS SS by Reactive AM

Nanoscale oxides were dispersed uniformly in as-built and heat-treated AM ODS SS samples, as shown in Fig. 5-4 and 5-5. The EDS mapping illustrates the composition of the nano oxides.

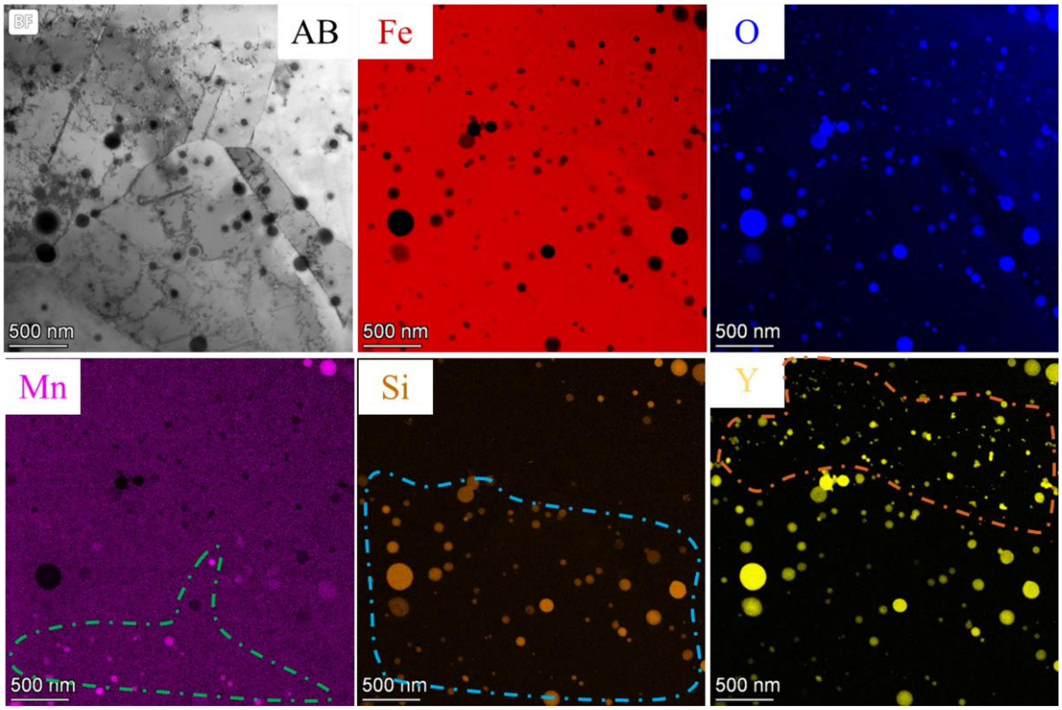

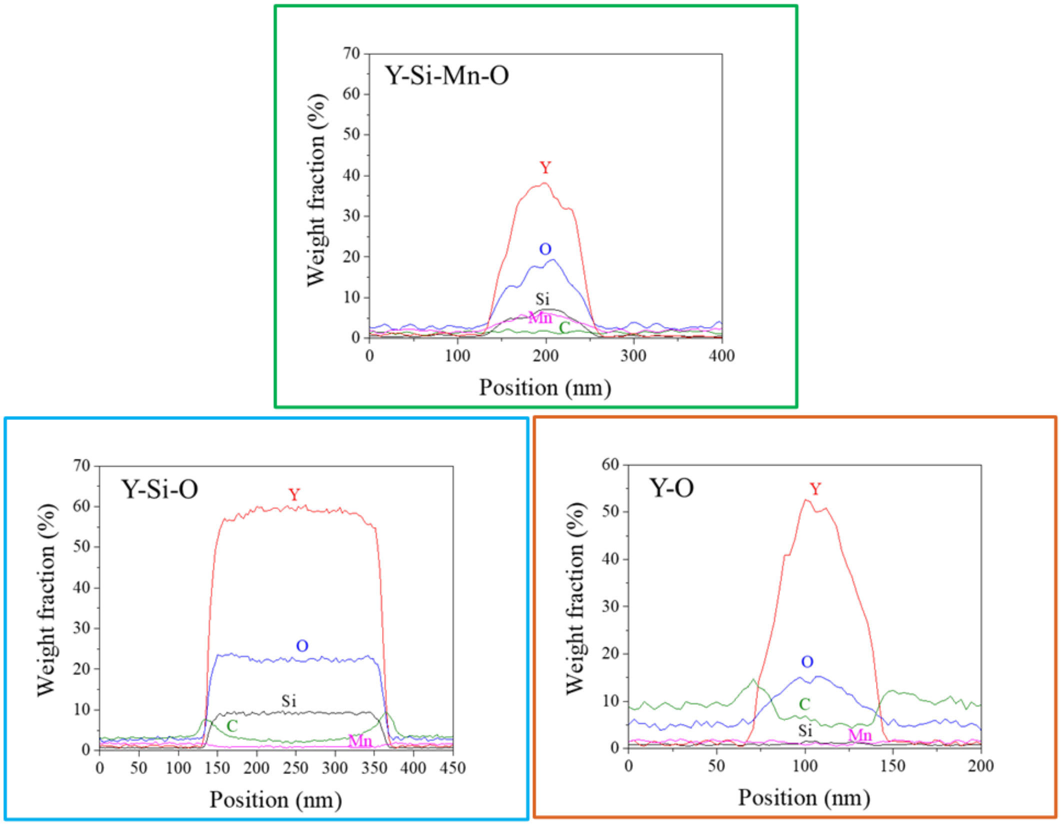

Fig. 5-4 TEM images in HAADF mode and EDS mapping show three types of oxide in the as-built 2 wt% Y_2O_3 ODS sample, line scan of Y-Si-O, Y-O, and Y-Si-Mn-O oxides in as-built 2 wt% Y_2O_3 ODS sample.

A variety of oxides, including Y-O, Y-Si-O, and Y-Si-Mn-O type oxides, were present in as-built AM ODS SS. The EDS line scan from different oxides shown in the figure also indicates the different elemental compositions of the oxides. No Fe_2O_3 was observed in the material, suggesting the oxygen donor was fully reacted. Thus, we believe that these oxides nucleated from the melt state, the dissolved Fe_2O_3 release oxygen and react with higher oxygen affinity getters yttrium. The oxide composition is dictated by Gibbs's free energy in the given alloy system. Complex oxides are generally formed whose compositions highly depend on the type of AM process and the alloy composition. Unlike the various oxide compositions in the as-built sample, most oxides consist of Y-Si-Mn-O in the heat-treated sample, suggesting the oxide evolution during the heat treatment.

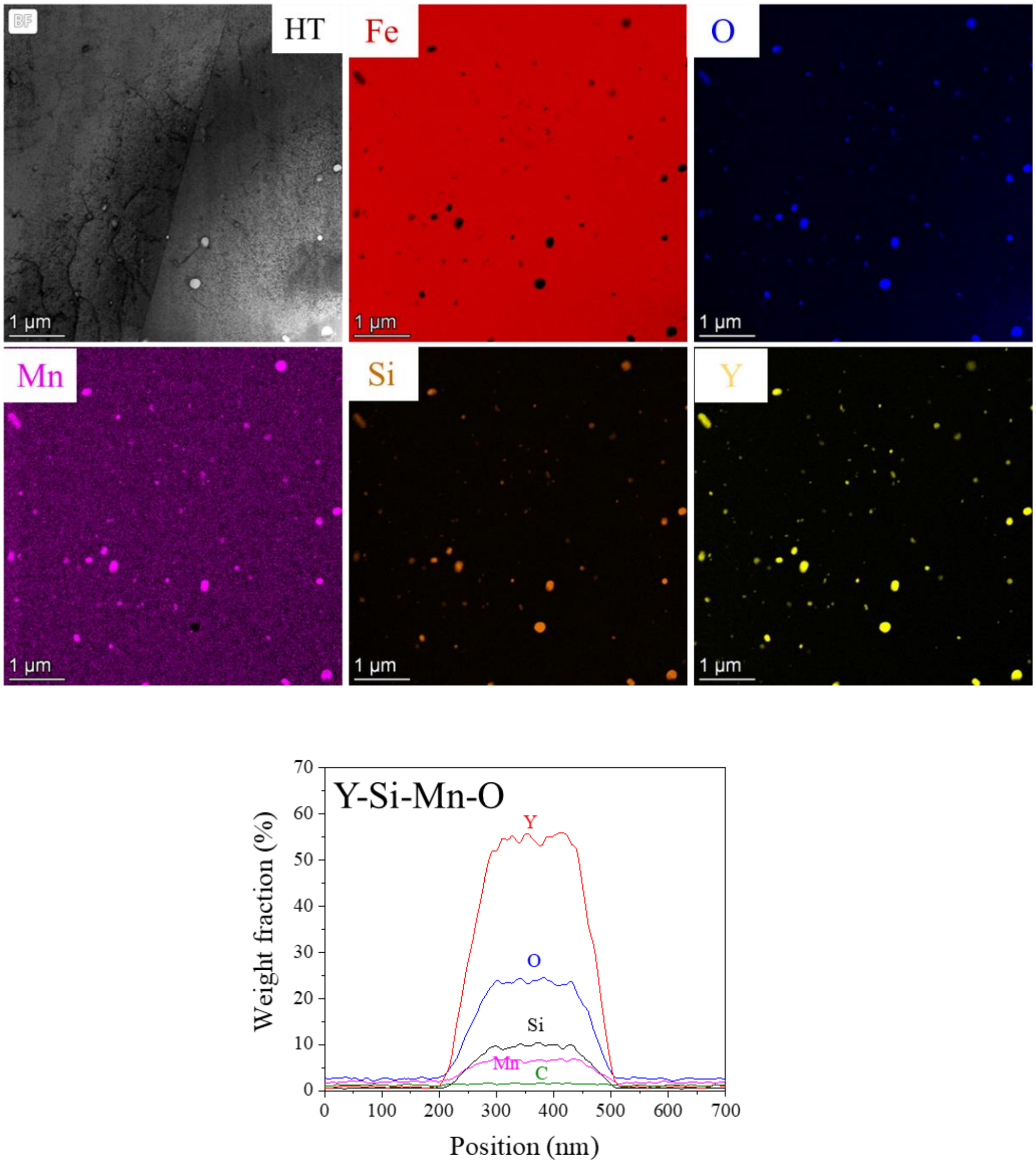

Fig. 5-5 TEM images in HAADF, and EDS mapping show a single type of oxide Y-Si-Mn-O in a 1100℃-50 h heat treated 2 wt% Y_2O_3 ODS sample.

High-resolution TEM images and the diffraction pattern of the oxide in as-built and heat-treated samples are shown in Fig. 5-6. It shows that the oxide in the as-built condition is amorphous. In contrast, the oxide has a clear crystalline structure in the heat-treated sample. The high cooling rate during the AM process favored amorphous oxide formation. The oxides transformation from amorphous to crystalline was also reported in conventional ODS alloys. After MA, the oxide dissolved in the alloy matrix and reprecipitated during the post-sintering/HIP process [122,123].

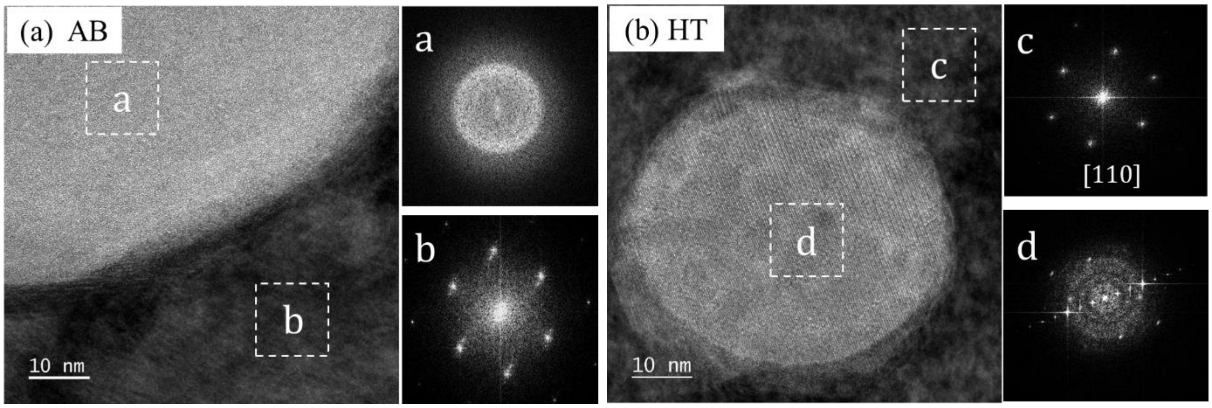

Fig. 5-6 HRTEM images and diffraction pattern of oxide in the as-built and HT sample show amorphous oxides in the AB sample and crystalline oxides in the HT sample.

The oxide size and density analyzed from the TEM images are shown in Fig. 5-7. The size of the in-situ oxide formed during AM process using a solid oxygen donor is ~50 nm. The size is almost identical to that of oxide obtained by in-situ oxidation in Chapter 4. This is probably due to the nucleation and growth of the oxide in the liquid metal being too fast. Although the AM process is noticed with a high cooling rate, the liquid phase duration time is still long enough for the oxide growth. A decrease in oxide density and slight coarsening are observed after the heat treatment. The oxide density of the heat-treated samples is about one-third of that in the as-built sample. The inferior oxide size and density of AM ODS steel can limit the application, and thus it is urgent to understand the oxide-forming and evolution during the L-PBF process. Improving the oxide density will be a big challenge for AM ODS steel, and more works need to be done to address this problem.

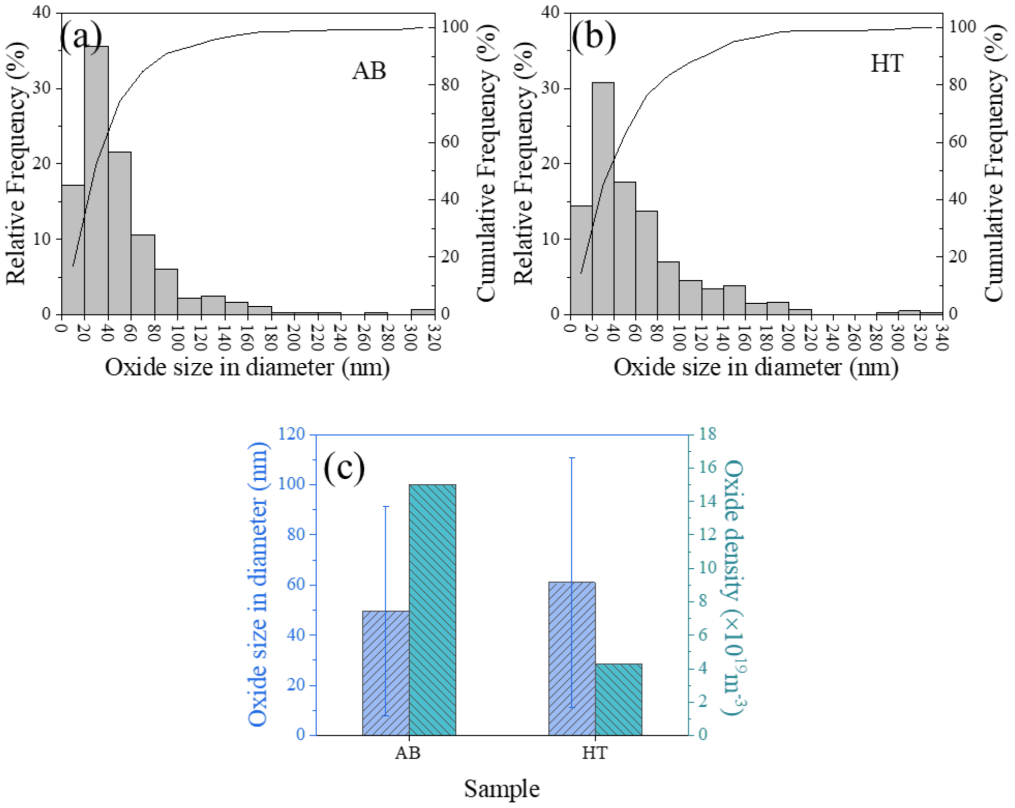

Fig. 5-7 Size distribution of oxides in as-built (a) and heat-treated (b) 2 wt% Y_2O_3 ODS samples; (c) average size and density of oxides.

5.2 Mechanical Properties

5.2.1 Nanohardness

Fig. 5-8 summarizes the nano hardness of AM 316L SS, AM 316L SS alloyed with Y (316L-1.69Y), and AM ODS SS with different Y_2O_3 content under as-built and different heattreating conditions. In as-built condition, AM 316L-1.69Y is harder than AM 316L SS due to the solid solution strengthening by yttrium. The as-built AM ODS steels were softer than 1.69Y-316L and almost identical to the hardness of AM 316L SS. The lower hardness in as-built ODS steel suggests that the Y in the feedstock powders fully reacted with the oxygen, and hence the solid solution strengthening by Y was minimized. However, the mechanical properties were influenced by high-temperature heat treatment. After heat-treated at 1100℃ for 10 hrs, AM 316L SS, 316L-1.69Y SS, and ODS SS with lower Y_2O_3 content showed hardness reduction as compared to the as-built condition. Hardness reduction of AM alloys after heat treatment was known due to extensive dislocation recovery and recrystallization [124]. Recovery reduces dislocation density and, in many alloys, dissemble dislocation cellular structures. However, AM ODS SS with higher Y_2O_3 content showed hardness increase after being heat-treated at 1100℃ for an extended amount of time. After 50 hours at 1100℃, 15-20% hardness increase can be obtained depending on the oxide content. This contradicts the general decreasing trend of oxide density by heat treatment, as shown in Fig. 5-7.

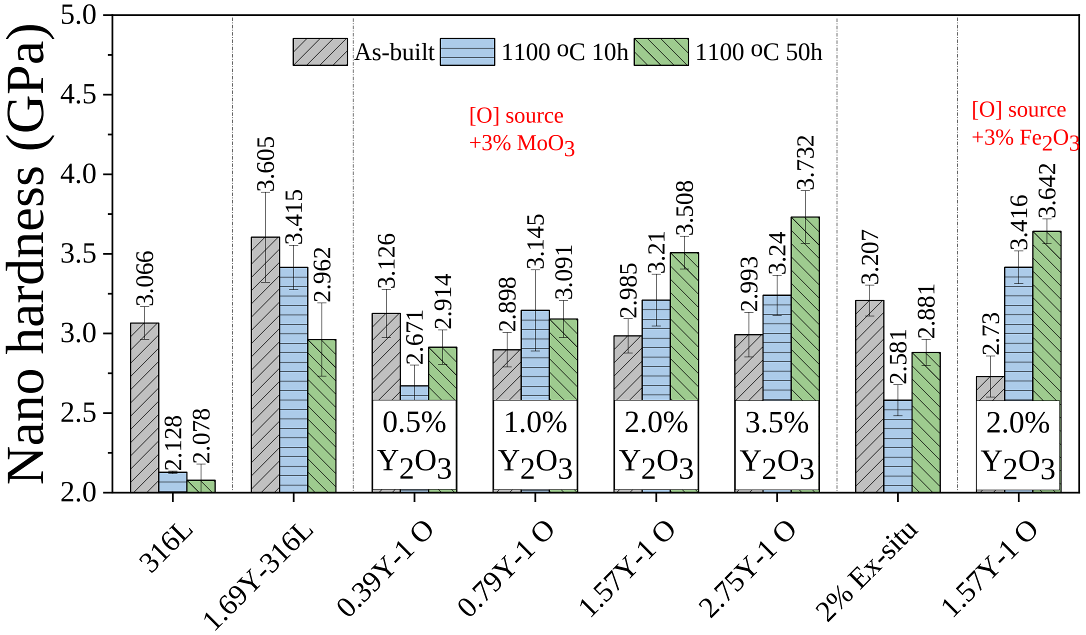

Fig. 5-8 Summary of nano hardness of as-built and heat-treated 316L, Y-doped 316L, AM ODS steel with different Y_2O_3 content.

5.2.2 Vicker's Hardness

Fig. 5-9 shows the Vickers hardness comparison of AM 316L SS, AM 316L-1.69Y SS, and AM ODS SS with different Y_2O_3 content. Similar to nano indentation results, the hardness increase of AM ODS SS with heat treatment was confirmed. For the in-situ reacted AM ODS steel, the hardness slightly decreases with the increasing content of Y_2O_3 in as-built conditions. In AM ODS SS with 2 wt% Y_2O_3, ~25% hardness increase was observed compared to as-built material. However, the dispersed barrier hardening model or Orowan strengthening mechanism [125] is difficult to explain the increased hardness since the oxide density of the heat-treated sample is lower than that in as-built conditions.

Due to the resolution limitation of TEM, sub-nano particles/clusters may not be captured.

More characterization like atom probe tomography and micropillar compression test were carried out to understand the strengthening mechanisms of AM ODS steel after heat treatment.

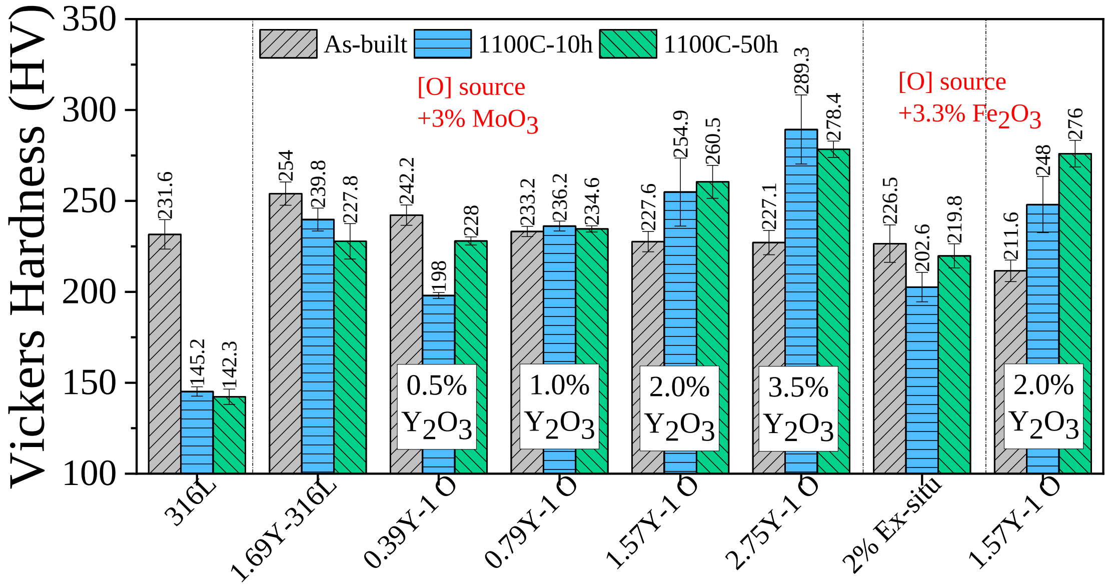

Fig. 5-9 Summary of Vickers hardness of as-built and heat-treated 316L, Y-doped 316L, AM ODS steel with different Y_2O_3 content.

5.3 Discussion

5.3.1 Chemical segregation and nanoscale dispersoids in AM ODS SS

Two hypotheses were developed to explain the hardness increase in AM ODS SS after heat treatment. First, the hardness change is mainly contributed by the solid state solution strengthening by dissolved Y. Second, sub-nanoscale clusters beyond TEM resolution were formed during heat treatment. Both hypotheses required atom probe tomography (APT) to conduct high resolution characterization. Table 5-1 shows the chemical composition obtained from APT from both as-built and 1100°C-50 hrs heat-trated samples, and the results were averaged from three tips of each sample. There is no Y in either as-built or heat-treated AM, which suggests Y fully reacted with oxygen and did not contribute to solid solution strengthening. There is also no sub-nanoscale clustering being observed in the heat-treated samples. Although the oxides in as-built AM ODS SS underwent phase transformation during heat treatment, the element redistribution did not nucleate new nanoclusters. As shown in Fig. 5-10, no evidence of sub-nano clustering was confirmed by this study.

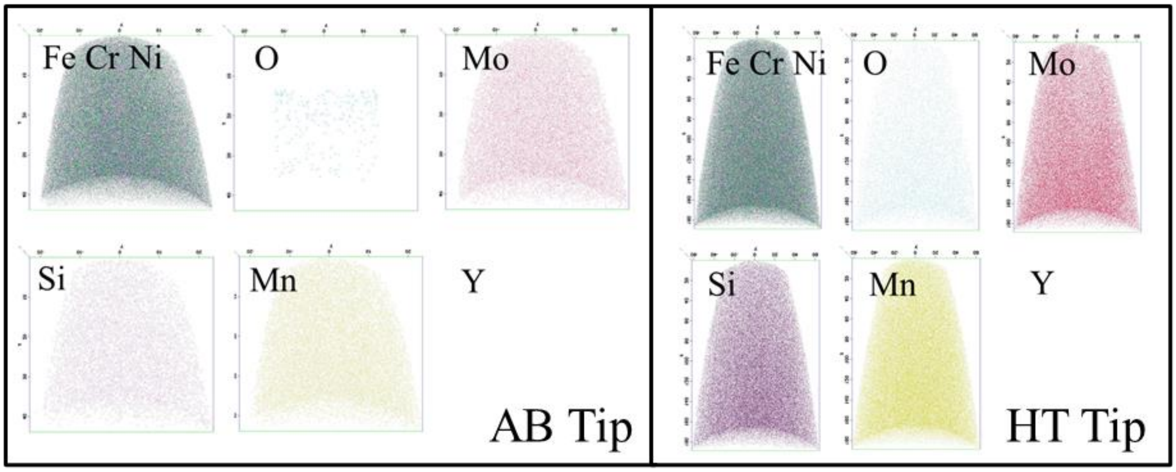

Fig. 5-10 Atom probe tomography of as-built and 1100°C-50hrs heat-treated 2 wt% Y_2O_3 L-PBF ODS steel.

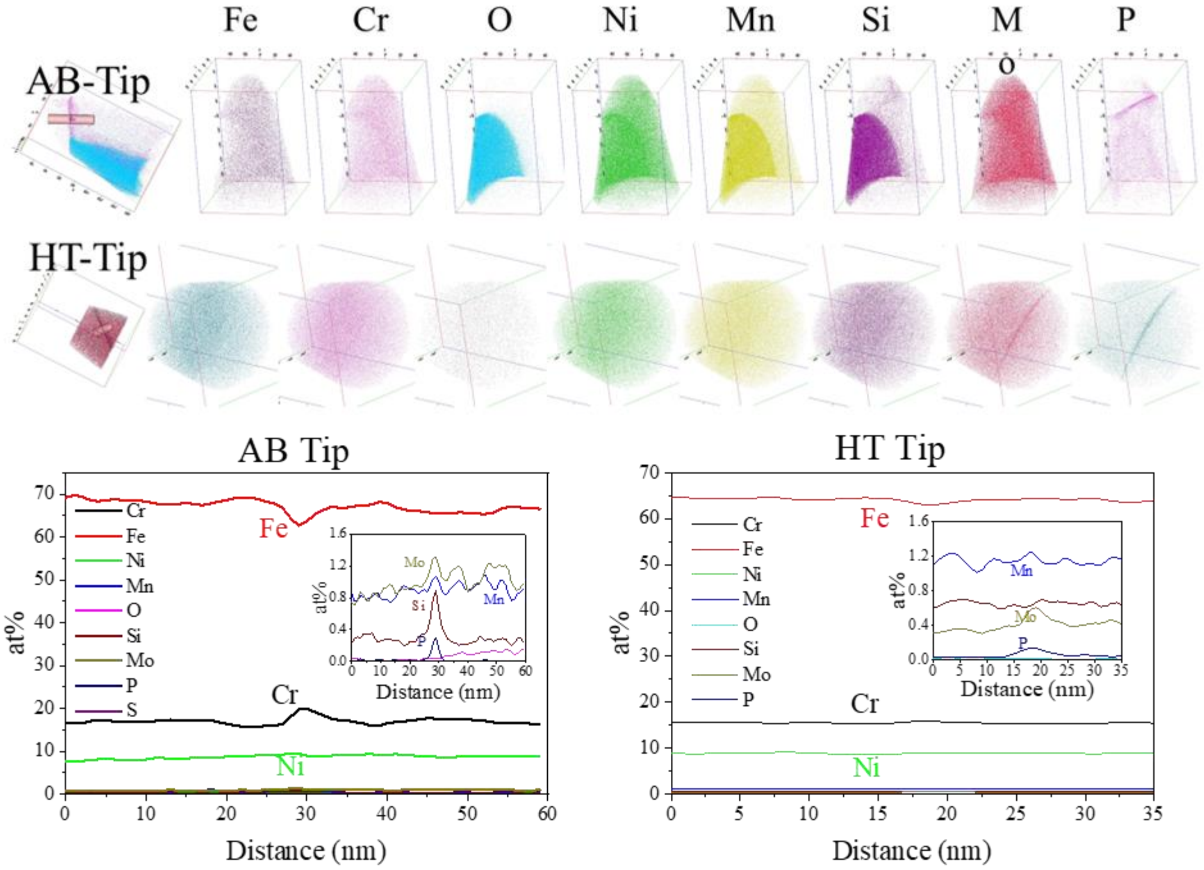

Fig. 5-11 Grain Boundary segregations in as-built and 1100℃-50hrs heat-treated 2 wt% Y_2O_3 L-PBF ODS steel.

Fig. 5-11 shows the grain boundary segregation of various elements in as-built and heat-treated AM ODS SS. The chemical segregation of Cr, Mo, Si, and P on the grain boundaries were estimated to be +3 at%, +0.3 at%, +0.6 at%, and +0.3 at%, respectively. This result is consistent with the study of L-PBF 316L SS [126]. AM 316L SS by L-PBF was reported to show [50,113,127,128] Mo and Cr segregation along both high-angle grain boundaries and low-angle dislocation cellular walls [11, 14, 19]. The presence of these cellular dislocation structures was determined to be the main contributor associated with the superior mechanical properties of AM steels [113]. However, the cellular structures and elemental segregation along them varnish at >800℃

[130]. At the temperature higher than 1000℃, AM 316L SS can fully recrystallize by eliminating dislocation cells [130]. Surprisingly, the segregation of Cr, Mo, and P remained in the 1100℃-50hrs heat-treated AM ODS SS, with approximately +0.5 at%, +0.2 at%, and +0.1 at%, respectively.

Table 5-1 Chemical composition of as-built and heat-treated 2 wt% Y_2O_3 L-PBF ODS steel, in wt%.

wt%	Fe	Cr	Ni	Mn	Si	Mo	Y	Cu	V	O	C	N	P
AB	70.038 ±0.947	15.728± 0.385	10.226± 0.87	0.964 ±0.019	0.196 ±0.05	2.434 ±0.589	0	0.272 ±0.172	0.067 ±0.017	0.0385± 0.047	0.006 ±0.002	0	0.032 ±0.041
HT	68.36 ±3.24	17.612± 1.499	10.925± 1.109	1.278 ±0.092	0.3195± 0.041	0.913 ±0.407	0.002 ±0.001	0.366 ±0.066	0.064 ±0.017	0.0105± 0.006	0.001 ±0.001	0.11 ±0.11	0.028 ±0.019

5.3.2 Thermal Stability of the Cellular Structure

Fig. 5-12 shows the cellular structure in as-built, and heat-treated AM ODS SS. Fig. 5-12(a) confirmed the presence of cellular dislocation structures in the as-built material even when equiaxed grain nucleation took place during laser solidification (shown in Fig. 5-3). Compared to the reported dislocation cells in as-built AM 316L SS from literatures, the cell walls in AM ODS SS in this work were generally defined by loosely tangled dislocation. The reduced dislocation density on cell walls in AM ODS SS, as compared to AM 316L SS, may be caused by the equiaxed grain nucleation during AM. Fig. 5-12(b) shows a STEM/HAADF image of the as-built sample. The brighter contrast of the cell wall is highlighted in this mode to show local chemical segregation [130,131]. The oxide was also observed uniformly distributed in the matrix and along the boundaries.

After heat treatment at 1100°C for 50 hrs, as shown in Fig. 5-12(c) and (d), the dislocation cell structures still remained in the material, with reduced dislocation density. Oxide particles were redistributed along the cell walls and grain boundaries, as shown in Fig. 5-12(c). We believe the high-density oxides along these boundaries might stabilize the structures of both dislocation cells and grain boundaries at high temperatures.

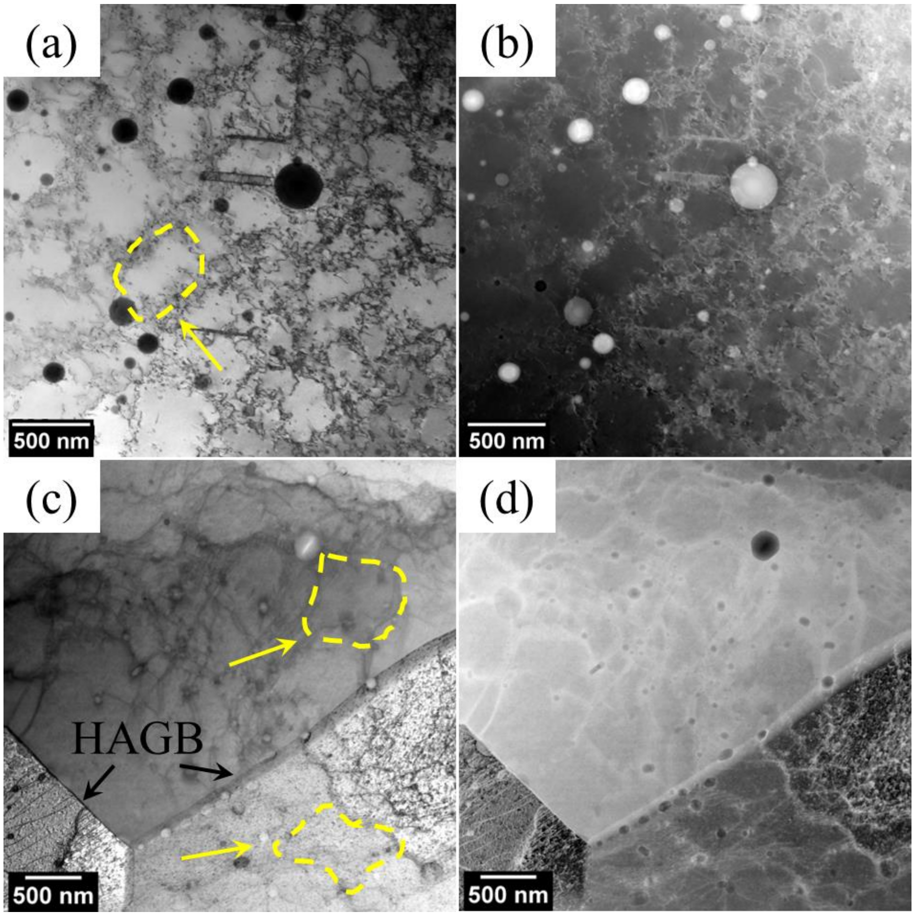

Fig. 5-12 Cellular structure in as-built and 1100°C-50hrs heat-treated 2 wt% Y_2O_3 L-PBF ODS steel. (a) BF (b) STEM/HAADF of as-built sample, (c) BF (d) STEM/HAADF of heat-treated sample reveal the cellular structure remained but showed different morphology from the as-built sample. The yellow arrow marks the cellular networks. Black arrows mark the high-angle grain boundaries.

Elemental segregation on the cellular boundary was not detected in as-built and heat-treated L-PBF ODS steel by TEM EDS analysis. It is possible that the contrast was from low-angle cell structure/grains with slightly different crystallographic orientations. During the annealing process, the dislocation cell structures are recovered and pinned by oxide particles and form cell/grain structures with low angle boundaries instead of maintaining the original cellular structures.

It has been shown that 600°C remains to be the temperature threshold above which AM 316L SS experiences thermal instability [130]. A clear drop in yield strength was observed by researchers, concurrent with an increased tensile ductility, leading to a substantial tradeoff in strength and ductility at the intermediate temperature range (600-1000°C). From 600-800°C, dislocation recovery contributes to the decrease in strength in AM 316L SS. When the temperature reaches 800-1000°C, cell walls disappear, but LAGBs remain stable. At higher temperatures >1000°C, grain coarsening and/or recrystallization can occur, leading to conventional 316L SS grain structure and mechanical properties. Different from AM 316L SS made by L-PBF, AM ODS SS by reactive AM showed enhanced mechanical properties and outstanding thermal stability at higher temperatures of 1100°C with extended time.

Since no nano or sub-nano clustering and solid solution strengthening were confirmed by TEM and APT, we believe the stabilized nano-size cellular boundaries can be the main contributor to the excellent thermal stability. In nanocrystalline (NC) metals [132,133], the stability of nanoscale grains can be enhanced by two approaches: a kinetics-driven process wherein the grain boundary mobility is reduced due to the presence of second phase particle by pinning and solute dragging and a thermodynamics-driven process, wherein the grain boundary energy is reduced due to the segregation of solute atoms at the grain boundaries. In this study, elemental segregation on the cellular boundaries was not confirmed. The redistribution of nano oxides in AM ODS SS suggests that the kinetic stabilization of grain boundaries by Zener pinning should be considered. In this case, a critical grain radius Rc can be calculated by the Zener equation [134], Rc=r/6f, here r and f (~0.008) are the radius and volume fraction of pinning particles. The estimated Rc in our AM ODS SS is about ~1.27±1.03 μm. Considering the oxides after heat treatment were mostly located along the cell walls, the local volume fraction of particles could be higher than the estimation. Thus, we believe nano oxides present in AM ODS SS can stabilize the cellular structures down to the sub-micron scale.

5.3.3 Micropillar Compression

EBSD-guided micropillar compression experiment was conducted to examine the deformation mechanisms of as-built and heat-treated AM ODS SS. The experiment was conducted by comparing grains with similar Schmid factors (SF). The selection of grains from both materials to conduct this study is based on the following three criteria: (1) large grain is desired, so the micropillar is made of a single crystal; (2) the grain with the largest SF is utilized to study the activation of the primary slip system; (3) the selected grain needs to have a large difference between the largest SF and second-largest SF so only one slip system can be activated by the experiment. For FCC system, slip occurs on {111} planes along <110> direction. Fig. 5-13 illustrates the grain selection process.

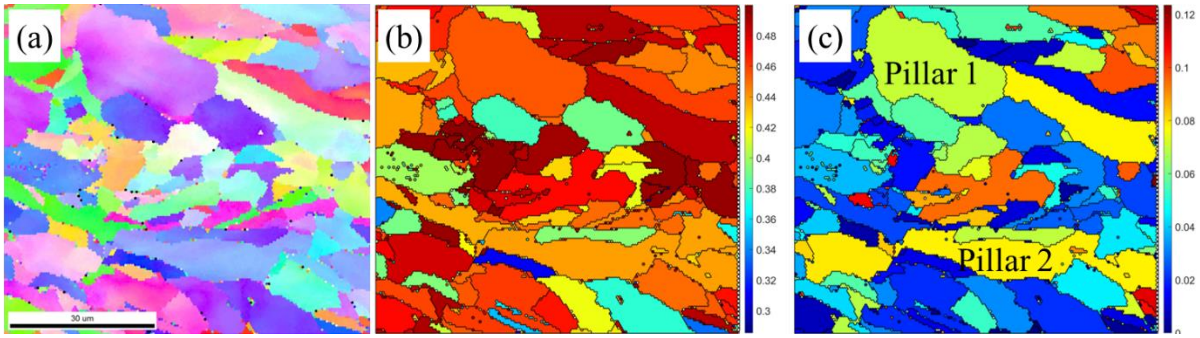

Fig. 5-13 Selection of micropillars: (a) EBSD shows the grain orientation, (b) largest Schmid Factor map processed from EBSD data, (c) largest SF minus second-largest SF map

Fig. 5-14 shows the stress-strain curve and snapshot of the pillar at different strains. The appearance of micropillar samples of as-built AM ODS SS was shown at the strain of 0 and 30% in Fig. 5-14(b). The sample was deformed uniformly, and there was no visible slip bands present on the deformed pillar. Similar deformation behavior was also reported in AM copper. This phenomenon was explained by the multiple cell wall-dislocation interaction where the long-range gliding of dislocations were restricted by stable dislocation cell boundaries [135].

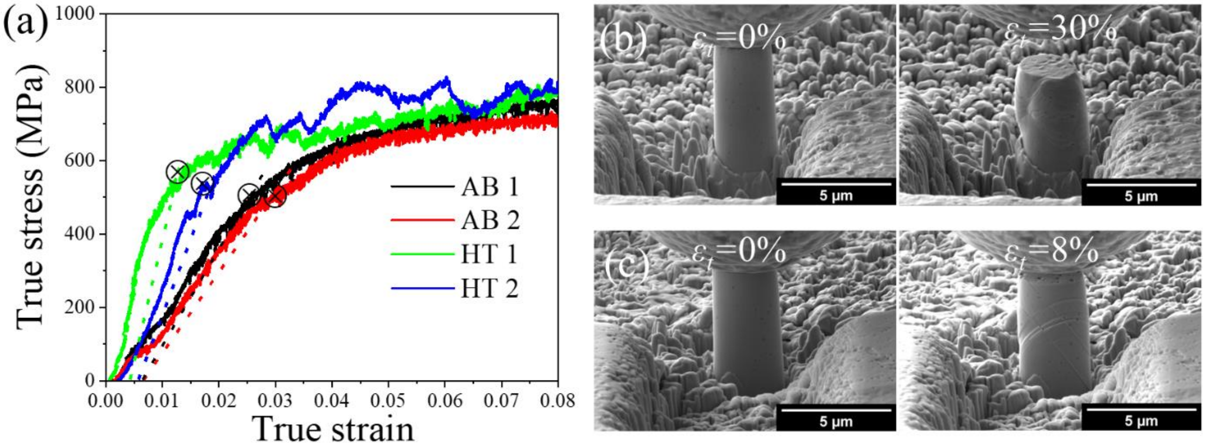

Fig. 5-14 In-situ micropillar compression tests at room temperature. (a) The true stress-strain curves. SEM snapshots of the micropillars at different strains (b) as-built and (c) heat-treated 2 wt% Y_2O_3 L-PBF ODS steel.

In heat-treated samples, after a short period of homogeneous plastic strain, the first slip band commences with a significant load drop. It's noted that even though such slip offset tends to reduce the load-bearing capability of the pillar, the slip only sustains a small amount without overall failure, and the flow stress starts to recover afterward. The several remarkable load drop on the stress-strain curve indicates that catastrophic shear-off happened quite often due to the escape of a large number of dislocations from the interactions of the same slip planes and the surface. In contrast, the as-built pillar had smoother plastic flow behavior. It indicates that the as-built sample had a much better ability of dislocation storage due to the dislocation networks. The difficulty of dislocations slipping out from the surface during glide enabled better plastic stability.

Generally, obtaining the yield stress from the stress-strain curves of micron pillars is rather challenging. Either taper or initial misalignment at the punch-pillar interface can lead to measurement deviation of the stress-strain profile. In former compressions, the flow stress at 0.2% offset or 2.5% axial strain has been extracted as a representation of yield stress[136,137]. Here, in order to minimize such issues, the yield strength at 0.2% offset has been chosen as the yield point (indicated as the dot lines in the stress-strain curve). The measured yield stress and calculated critical shear stress of as-built and heat-treated samples are summarized in Table 5-2. The little difference in yield stress between two pillars from one sample suggests the data was representative. The yield stress of the heat-treated sample is ~13% higher than the as-built one. The mechanical property of single-crystal grain obtained from the micropillar compression test is consistent with the bulk property evaluated by the Vickers hardness test.

Table 5-2 Summary of 0.2% offset yield stress and critical shear stress of as-built and 1100℃-50hrs heat-treated 2 wt% Y_2O_3 L-PBF ODS steel.

Sample	0.2% Yield stress (MPa)	Largest Schmid Factor	Critical Shear Stress (MPa)
AB 1	467	0.459	214
AB 2	489	0.445	216
HT 1	533	0.467	248
HT 2	537	0.447	240

5.3.4 4D STEM

With the suite of experimental evidences, we conclude that the hardness or strength increase in heat-treated AM ODS SS as compared to as-built AM ODS SS was NOT due to (1) solid solution strengthening, (2) dislocation hardening, (3) precipitation strengthening by nano oxides and clustering. The stabilization of cellular boundaries by nano oxides and hard-to-detect interstitials (maybe O) is the only possible contributor to the high thermal stability and improved mechanical properties at higher annealing temperatures. 4D STEM was utilized to characterize the subgrain cellular boundaries in AM ODS SS after heat treatment. Fig. 5-15 shows a 4D STEM data analysis from 256×256 diffraction patterns. We determine the pixel-per-pixel change in the center of intensity of the diffraction disk and come up with a vector map of local deflections of the electron probe. This is encoded in the "horizontal" and "vertical" images as components of the deflection vector. These images are then combined into the "composite color" image. Each color stands for the direction of deflection. While the electron deflection shown in these images is not directly correlated to the crystal orientation, the analysis has the potential to analyze small changes in crystal orientation in the material. As shown in the figure, different cells in the heat-treated sample clearly show different contrasts of electron beam deflection, suggesting that these cells may present orientation differences. More work is being conducted to quantify the misorientation of these cell walls.

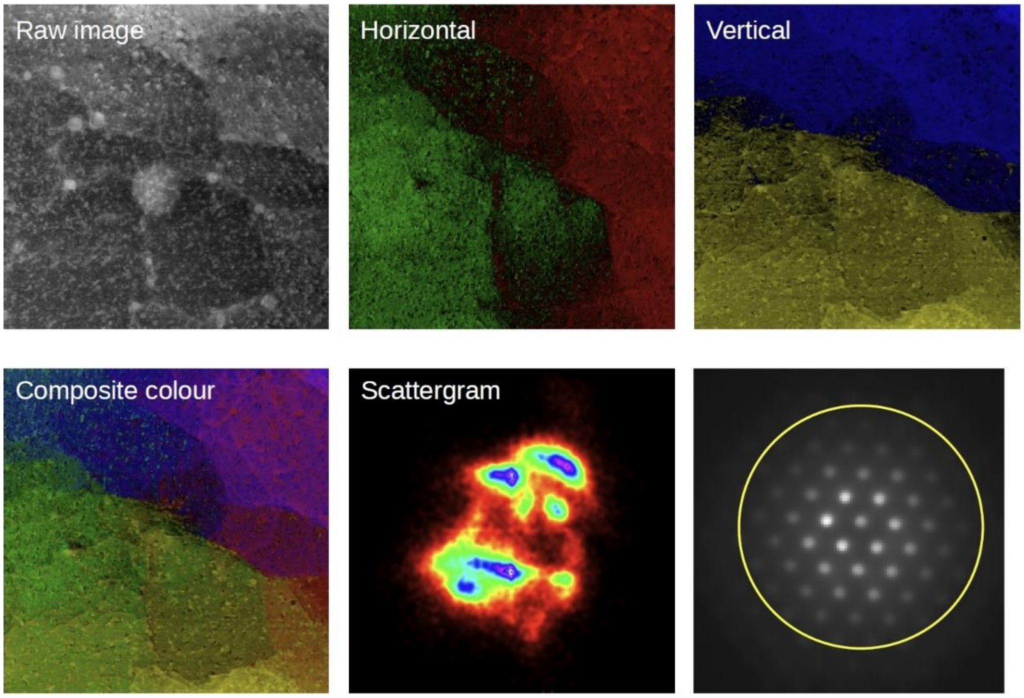

Fig. 5-15 Deflection of electron beam when passing through the sample with different orientation

5.4 Conclusion

A novel in-situ reactive additive manufacturing by using a low melting point solid-oxygen donor creates a new way to strengthen the ODS alloys and improve the thermal stability. Some specific conclusions are addressed as follows:

1) Uniformly dispersed oxide with an average size of ~50 nm and density of $10^{20}/m^3$ was obtained in AM ODS SS. No sub-nanoscale clusters were observed in either as-built or heat-treated samples.
2) The fast laser process generates inhomogeneous chemical distribution and metastable oxide precipitations. Cr, Mo, and P segregation were observed on the grain boundary. Metastable amorphous oxide with different compositions of Y-O, Y-Si-O, and Y-Si-

Mn-O existed in the as-built sample. After heat treatment, these oxides transferred into the crystalline structure with an identical composition of Y-Si-Mn-O.

3) Pre-alloyed yttrium concentration affects the thermal stability of the in-situ L-PBF ODS steel. Higher yttrium content yields high hardness after heat treatment.
4) The stabilization of cellular boundaries by nano oxides is a possible contributor to the high thermal stability and improved mechanical properties at the higher annealing temperature.

CHAPTER 6

EFFECTS OF PULSE WAVE LASER PARAMETERS ON THE QUALITY AND MECHANICAL PROPERTIES OF THE ADDITIVELY MANUFACTURED 316L SS

The oxides in size of ~50 nm with the density of 10^{19}-10^{20} m^{-3} were obtained in the in-situ reacted L-PBF ODS steel by using gas- or solid-oxygen donors in studies shown in Chapter 4 and 5. The L-PBF process was carried out using a Concept Laser M2 machine equipped with a continuous-wave (CW) laser. The relative coarser oxides compared to that in the PM materials indicates there is a large space to further optimize the oxide distribution in AM ODS steels. Recently, the pulse-wave (PW) laser has been applied to AM process and shows a vast potential and advantages over CW lasers, such as increasing part resolution, rapid cooling rate, reducing residual stresses, etc. [77,79,82,87]. We believe the enhanced cooling rate and different PW laser parameters could affect the oxide distribution in AM ODS steel. Due to the complexity of PW laser parameters, a parametric study is required to fabricate parts with reasonable quality. In this Chapter, the effects of PW laser parameters such as laser power (P), repetition rate (RR), pulse width, and pulse interval on the part quality of 316L SS were systematically studied. The microstructure and the mechanical property of AM 316L using PW laser were also evaluated.

6.1 Schematic of PW Laser with Different Parameters

The high number of parameters in PW laser make it challenging to understand how these variables affect the AM parts. Several important primary parameteres related to PW laser are laser power (P, W), pulse width (t_{on}) and repetition rate (RR). Other important primary parameters that affect the printing quality are scan speed (υ, mm/s) and hatch spacing (h, μm). Also, some secondary variables related to these independent ones can also influence the sample quality. For example, the duty cycle δ, which is defined as $\delta = t_{on} \times RR$; average power P_{avg}, which can be calculated as $P_{avg} = P_{peak} \times \delta$; linear energy input $E_{line} = P_{peak} \times t_{on} \times RR/\upsilon$; and pulse interval , $1/RR$. This section will discuss the key parameters of PW laser AM and try to figure out which has the most significant effect. In each individual parameter study, only the interested parameter was changed, while others are arbitrarily set as constant. Laser power, pulse width, and pulse interval will affect the single laser spot geometry and heat dissipation. When applying the same duty cycle (same energy input), the different combinations of repetition rate and pulse width are also investigated.

6.1.1 Laser Power

Fig. 6-1 shows the schematic representation of temporal and spatial disposition of PW laser with different power levels. Other parameters like scan speed, pulse width, and repetition rate were set as constant, and hence the duty cycle and the pulse interval will be constant. In this case, the energy input to a laser spot is different. A larger laser spot size and melt pool depth are expected at higher power.

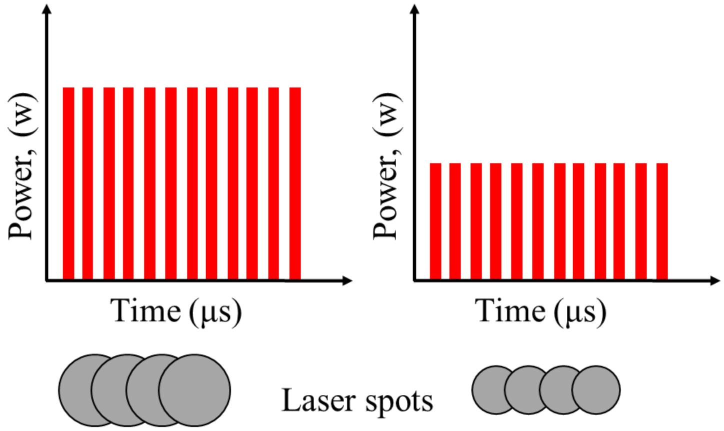

Fig. 6-1 Schematic representation of temporal and spatial disposition of PW laser with different powers.

6.1.2 Pulse Interval

As shown in Fig. 6-2, the pulse laser power and pulse width were set as constant. The scan speed was also fixed, and hence different repetition rates yielded different duty cycles (RR × Pulse width) and pulse intervals. The energy input to a laser spot is identical, but the spot density or the distance between two laser spots is different. The size and melt pool depth of each laser spot should be the same. But a larger spacing enables a longer cooling time for each laser spot, which will change the cooling rate.

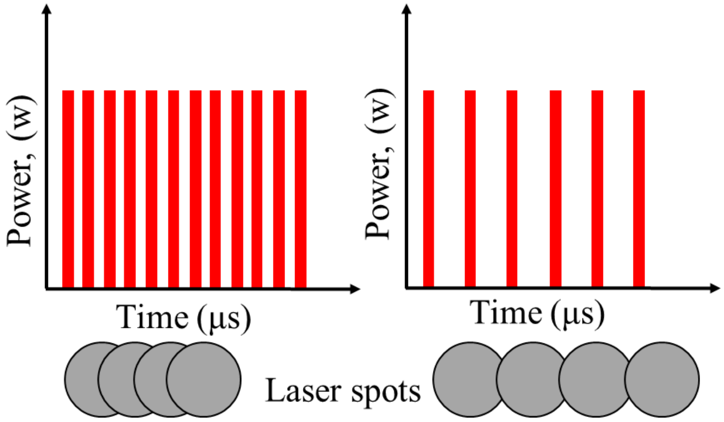

Fig. 6-2 Schematic representation of temporal and spatial disposition of PW laser with different pulse intervals.

6.1.3 Pulse Width

Fig. 6-3 shows the effect of pulse width change under the same power, repetition rate, and pulse interval applied. The extended pulse width will provide more energy to a laser spot and generate a larger and deeper melt pool. In this case, the duty cycle will change along with the pulse width. Longer pulse width can provide higher energy input to a laser spot and generate a melt pool with a higher peak temperature as well as a longer liquid phase duration time.

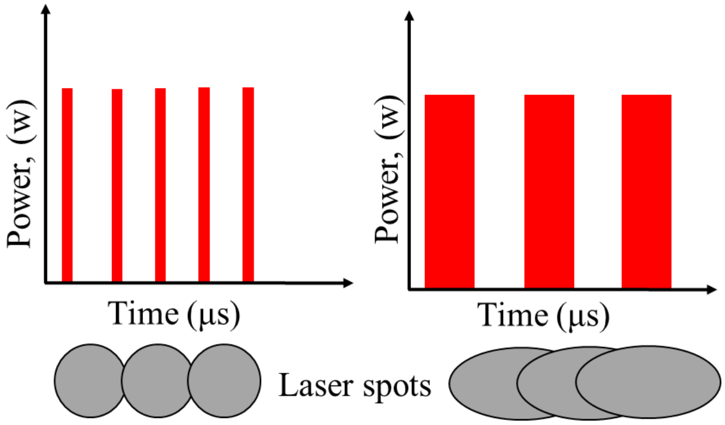

Fig. 6-3 Schematic representation of temporal and spatial disposition of PW laser with different pulse widths.

6.1.4 Repetition Rate

In Fig. 6-4, constant laser power and duty cycle are applied, but the repetition rate changes. In this case, the pulse width and interval will be different along with the change in repetition rate. The overall energy density put into the melt pool will be identical. However, the energy input for each laser spot is different, and hence the duration of metal in the liquid phase and the cooling rate for each laser spot are tailored.

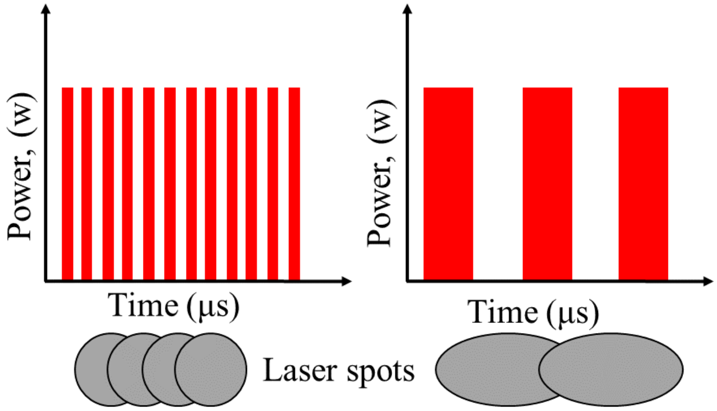

Fig. 6-4 Schematic representation of temporal and spatial disposition of PW laser with different pulse repetition rates.

6.2 Selection of PW Laser Parameter

A continuous laser track is a prerequisite for a quality AM part. Single-track scanning was applied to examine the melting quality. Fig.6-5 shows the tracks with different PW laser power, and the other parameters are arbitrarily chosen following the description in section 6.2.1. Laser power greatly affects the morphology of the track. At smaller laser power (120 W), the single track is not continuous, suggesting the energy is insufficient to melt the substrate. With the energy increasing to 150W, a serrated outline of the track can be observed. The small melt pool cannot enable sufficient overlap between laser spots. At higher power, continuous melt tracks are observed. Laser power from 150-270 W was chosen to fabricate bulk samples, and these samples are designated as “Power 1 to 5”, as shown in Table 6-1. Laser power of 210 W was chosen for studying the effects of other parameters, such as pulse interval, pulse width, and repetition rate.

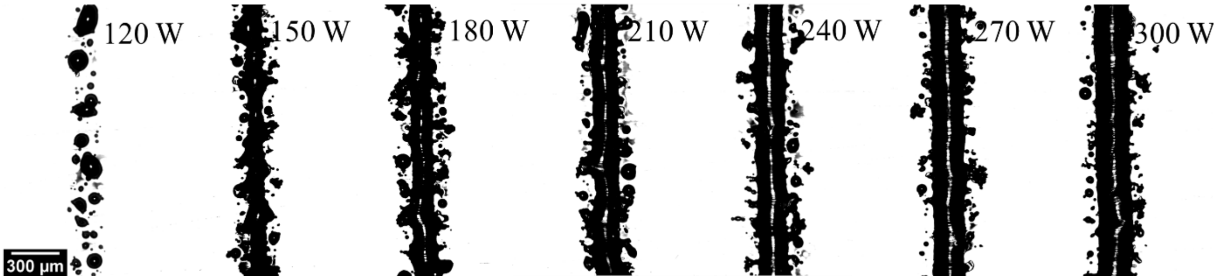

Fig. 6-5 Morphology of the single-track with different powers and detailed parameters are summarized in table 6-1 (#1-#7).

Fig. 6-6 shows the tracks with different pulse intervals. A longer interval of 500 µs between two laser spots lowers linear energy input and yields a discontinuous track. A decrease in pulse interval results in wider melt pools. The interval from 71-250 µs was selected to prepare bulk samples, and they are designated as “Interval 1-4” in Table 6-1.

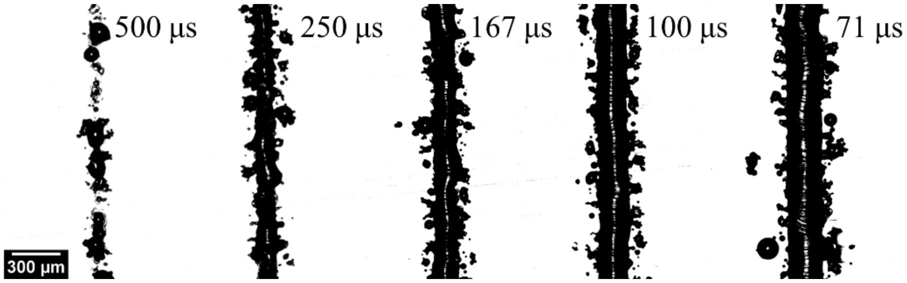

Fig. 6-6 Morphology of the single-track with different pulse intervals and detailed parameters are summarized in table 6-1 (#8-#12).

Fig. 6-7 reveals the tracks with different pulse widths. The longer pulse width produces a higher energy input, resulting in a wider melt pool. Pulse width from 20-60 µs was selected to prepare bulk samples, and they are designated as “width 1-5” in Table 6-1.

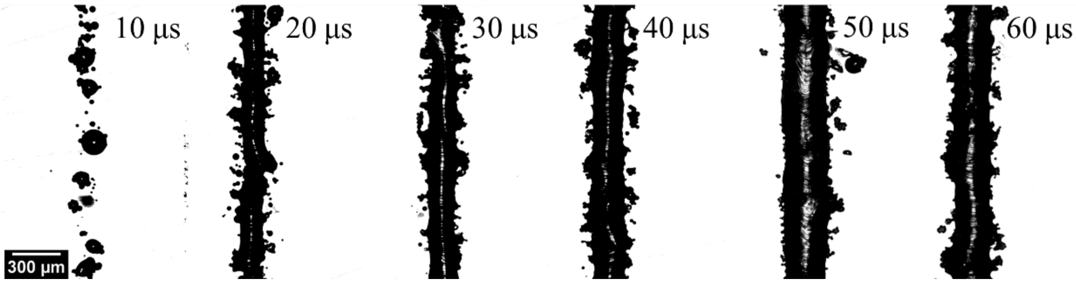

Fig. 6-7 Morphology of the single-track with different pulse widths and detailed parameters are summarized in table 6-1 (#13-#18).

Fig. 6-8 shows the tracks with different repetition rates. All the tracks have the same energy input, but some differences in the melt pool width can still be observed with varying repetition rates. Repetition rate from 5-50 kHz was selected to prepare bulk samples, and they are designated as “RR 1-4” in Table 6-1.

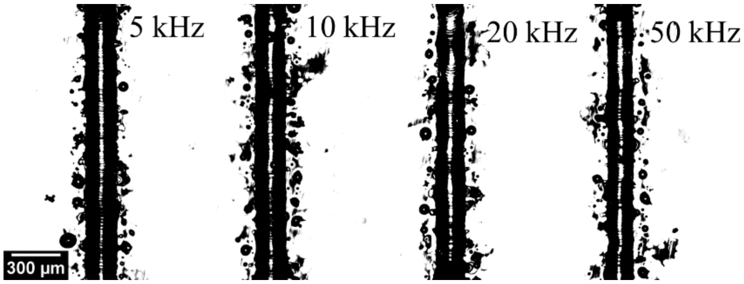

Fig. 6-8 Morphology of the single-track with different repetition rates and detailed parameters are summarized in table 6-1 (#19-#22).

Table 6-1 Summary of PW laser parameters with different power, pulse interval, pulse width, and repetition rate.

#	Laser mode	Power peak (W)	Power avg (W)	Speed (mm/s)	Duty cycle	Duration time/Pulse width(μs)	Repetition Rate	Linear Heat Input (J/m)	Spot/ mm	Interval/ μs	Designation
1	PW	120	48	80	0.4	20	20000	600	250	50	
2	PW	150	60	80	0.4	20	20000	750	250	50	Power 1
3	PW	180	72	80	0.4	20	20000	900	250	50	Power 2
4	PW	210	84	80	0.4	20	20000	1050	250	50	Power 3
5	PW	240	96	80	0.4	20	20000	1200	250	50	Power 4
6	PW	270	108	80	0.4	20	20000	1350	250	50	Power 5
7	PW	300	120	80	0.4	20	20000	1500	250	50	
8	PW	210	21	100	0.1	50	2000	210	20	500	
9	PW	210	42	100	0.2	50	4000	420	40	250	Interval 1
10	PW	210	63	100	0.3	50	6000	630	60	167	Interval 2
11	PW	210	105	100	0.5	50	10000	1050	100	100	Interval 3
12	PW	210	147	100	0.7	50	14000	1470	140	71	Interval 4
13	PW	210	31.5	100	0.15	10	15000	315	150	67	

14	PW	210	63	100	0.3	20	15000	630	150	67	Width 1
15	PW	210	94.5	100	0.45	30	15000	945	150	67	Width 2
16	PW	210	126	100	0.6	40	15000	1260	150	67	Width 3
17	PW	210	157.5	100	0.75	50	15000	1575	150	67	Width 4
18	PW	210	189	100	0.9	60	15000	1890	150	67	Width 5
19	PW	210	105	100	0.5	100	5000	1050	50	200	RR 1
20	PW	210	105	100	0.5	50	10000	1050	100	100	RR 2
21	PW	210	105	100	0.5	25	20000	1050	200	50	RR 3
22	PW	210	105	100	0.5	10	50000	1050	500	20	RR 4
23	CW	210	210	100	1			2100			CW

6.3 Effect on the Parts Quality

In the single track study, the widths of the continuous track obtained by appropriate laser parameters were in the range of 140-200 μm. To enable sufficient overlap (50-100%) between adjacent laser tracks, the hatch spacing of 70 μm was selected and the layer thickness of 30 μm was applied to print 3×5×10 mm^3 parts with various parameters listed in Table 6-1. Fig. 6-9 shows the optical images of AM 316L SS by L-PBF printed with different PW laser parameters. The black contrast indicates defects/pores in the sample.

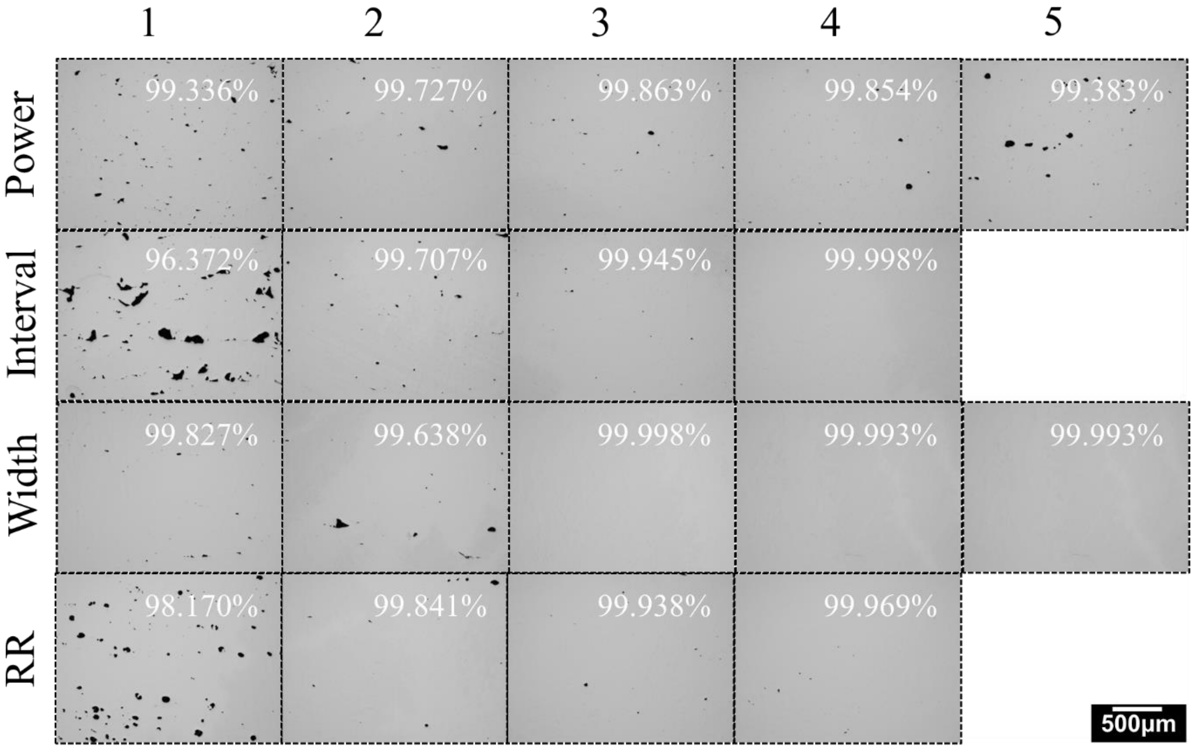

Fig. 6-9 Optical microscope images of L-PBF 316L SS by pulse laser with different power, interval, width, and repetition rate. Black contrast indicates the defects.

Three major defects in AM 316L SS are reported: lack of fusion (LOF), gas pores, and keyhole [138]. Lack of fusion encompasses irregular defects, elongated shapes, and sometimes unmelted powder particles present. Lack-of-fusion defects are a result of insufficient energy input. Gas-entrapped pores are characterized by their spherical shape. Pores form and evolve through gas entrapment, supersaturation of dissolved gases, and chemical reactions that produce gaseous species within the melt pool. Keyhole porosity is initiated by generating a deep V-shaped melt pool and vaporizing metal within the melt pool. Keyhole porosity for the L-PBF process results from the rapid local melting of powder, and usually, higher energy input causes more keyhole defects. Keyhole pores vary in shape and range in size.

In the samples under Power 1, Interval 1&2, and Width 1&2, irregular lack of fusion defects are observed, indicating the insufficient energy input of these conditions. The samples under Power 4&5 and RR 1 show primarily keyhole defects. Fig. 6-10 shows the part density as the functions of power, pulse interval, width, and repetition rate. The part density was measured by area fraction analysis in ImageJ software. A parabolic shape of the Density vs. Power relationship suggests an optimal power range for dense parts, with lack-of-fusion at low power and keyholing at high power. Reducing the pulse interval is beneficial to increasing the part quality under this set of parameters. Pulse width change from 20 to 60 μs didn't affect the density. Higher repetition rates yield denser parts.

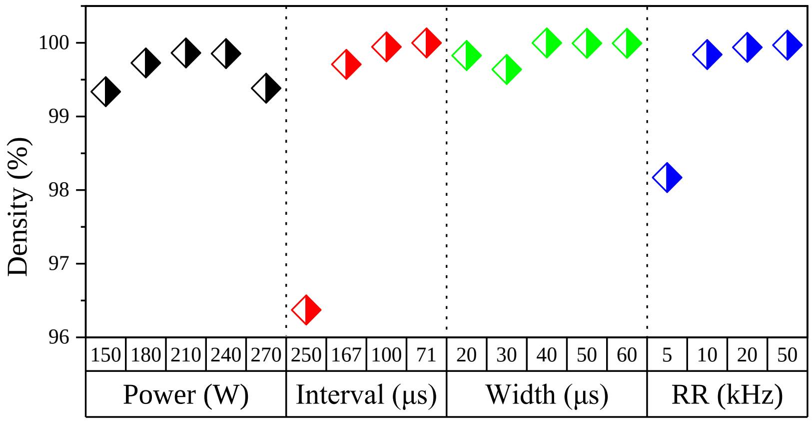

Fig. 6-10 Density of samples with different printing parameters, power, pulse interval width, and repetition rate.

It is logical to assume that the defect structures can be directly controlled by the input energy density. The plot of part density vs. linear energy input is shown in Fig. 6-11, which was calculated based on PW laser combinations listed in Table 6-1. Interestingly, nearly full dense material can be achieved in a wide range of energy input, from 650-1890 J/m. Lower energy at 400 J/m deteriorated the part density. In addition, at the same linear energy input, the part quality was not identical, from 98.17% to 99.99%. These results suggest that the linear energy input is critical to the part quality. However, the understandings of the combined effects of these parameters, for example, pulse width, pulse interval, and repetition rate are also essential.

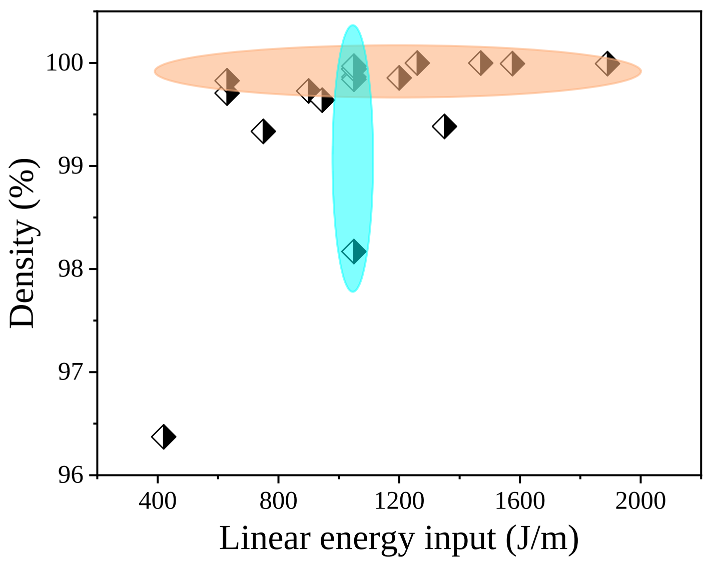

Fig. 6-11 L-PBF 316L parts density vs. linear energy input. Weak correlation between part density and energy input in pulse laser L-PBF.

6.4 Effect of PW laser parameters on the Mechanical Properties

Fig. 6-12 shows the nano hardness and modulus of AM 316L SS with different pulse laser parameters. For comparison, a CW laser-printed sample was also included. The parameter of CW laser was listed in Table 6-1, #23. We want to note that the same power and scan speed of CW sample lead to higher energy input compared to the PW samples, this may also cause the reduced hardness. Either increasing the scan speed or reducing the power to maintain the same energy input as the PW samples could make the comparison between CW and PW samples more reasonable in hardness and microstructure. The CW laser sample shows the lowest hardness among all the conditions. Nano hardness was not affected by the part density due to the small indent size of ~10 μm, but the modulus depended on the density of the part. The lowest density of two samples, “interval 1” and “RR 1,” show significantly lower modulus than others. And higher modulus is obtained in the sample with higher density.

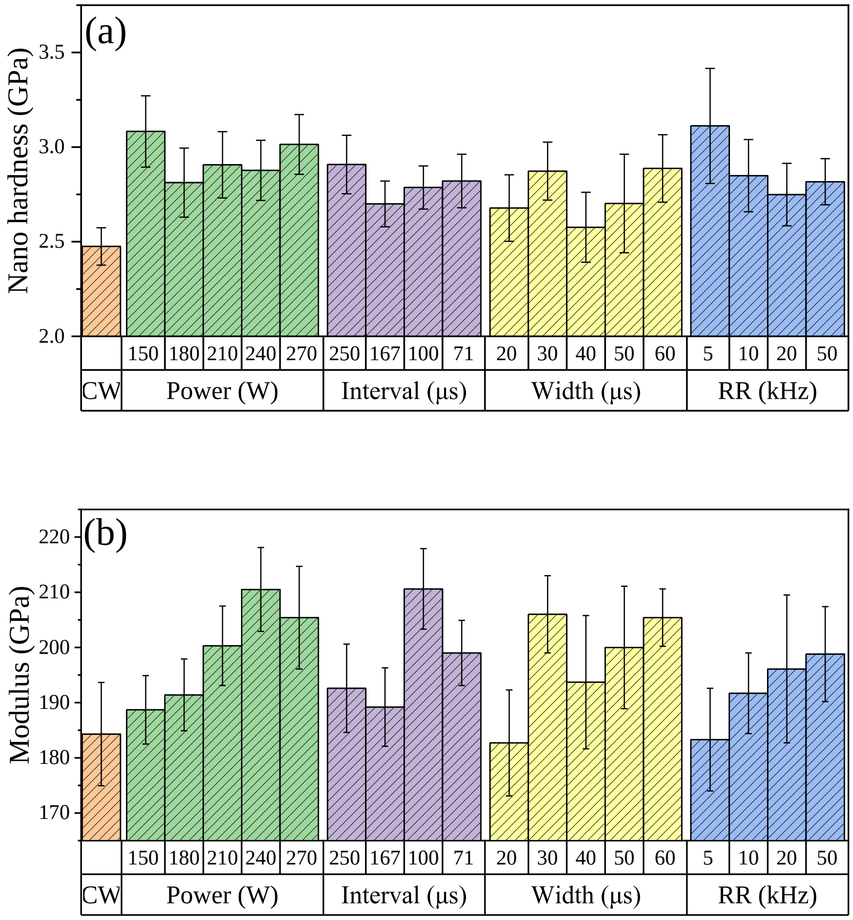

Fig. 6-12 Nano hardness (a) modulus (b) of L-PBF 316L SS with different printing parameters: power, pulse interval, pulse width, and repetition rate.

In summary, pulse laser, depending on the laser parameters, may or may not impact the mechanical properties. Laser power has little effect on nano hardness, causing insignificant differences in the range of the study. A longer pulse interval is beneficial to the mechanical properties of AM 316L SS by PW laser. Pulse width in the narrow range of 20-60 μs didn’t affect the nano hardness too much, but we expect that nanosecond, picosecond, or even femtosecond laser would have more profound effects on the mechanical properties. Nano hardness is sensitive to the repetition rate. With a 5 kHz pulse laser, the highest nano hardness, 3.11 GPa, was obtained among all the samples.

6.5 Effect on the Microstructure

Three sets of samples, “Power 1-5”, “RR 1-4”, and “Interval 1-4”, was characterized to understand how the pulse laser affects the microstructure. Fig. 6-13 shows the melt pool structure of the samples with different printing parameters: power, pulse interval, pulse width, and repetition rate. The laser energy, absorption efficiency, and the material’s thermal properties dictate the size and shape of the melt pool. It was concluded that melt pool boundary was the primary factor influencing anisotropy in AM parts [139], and melt pool boundary allows for preferential slip during deformation due to its low dislocation density [113]. Crack paths appeared to follow the melt pools rather than the grain boundaries, as reported by Wen et al. [140]. As discussed in section 6.1, the laser spot varies in shape and depth with different parameters. Higher PW laser power, e.g., Power 5 sample, created a larger melt region similar to the sample made by CW laser. In sample “RR 1”, a higher melt pool boundary density is observed. “RR 1” has the longest pulse width and can generate a deep melt pool and remelt previous solidified, and the distance between the two melt pool boundaries is close to the layer thickness of 30 μm. A longer pulse interval in sample “Interval 1” provides enough time for the adjacent melt region to solidify, and then the next laser spot partially remelts it and creates a melt pool boundary.

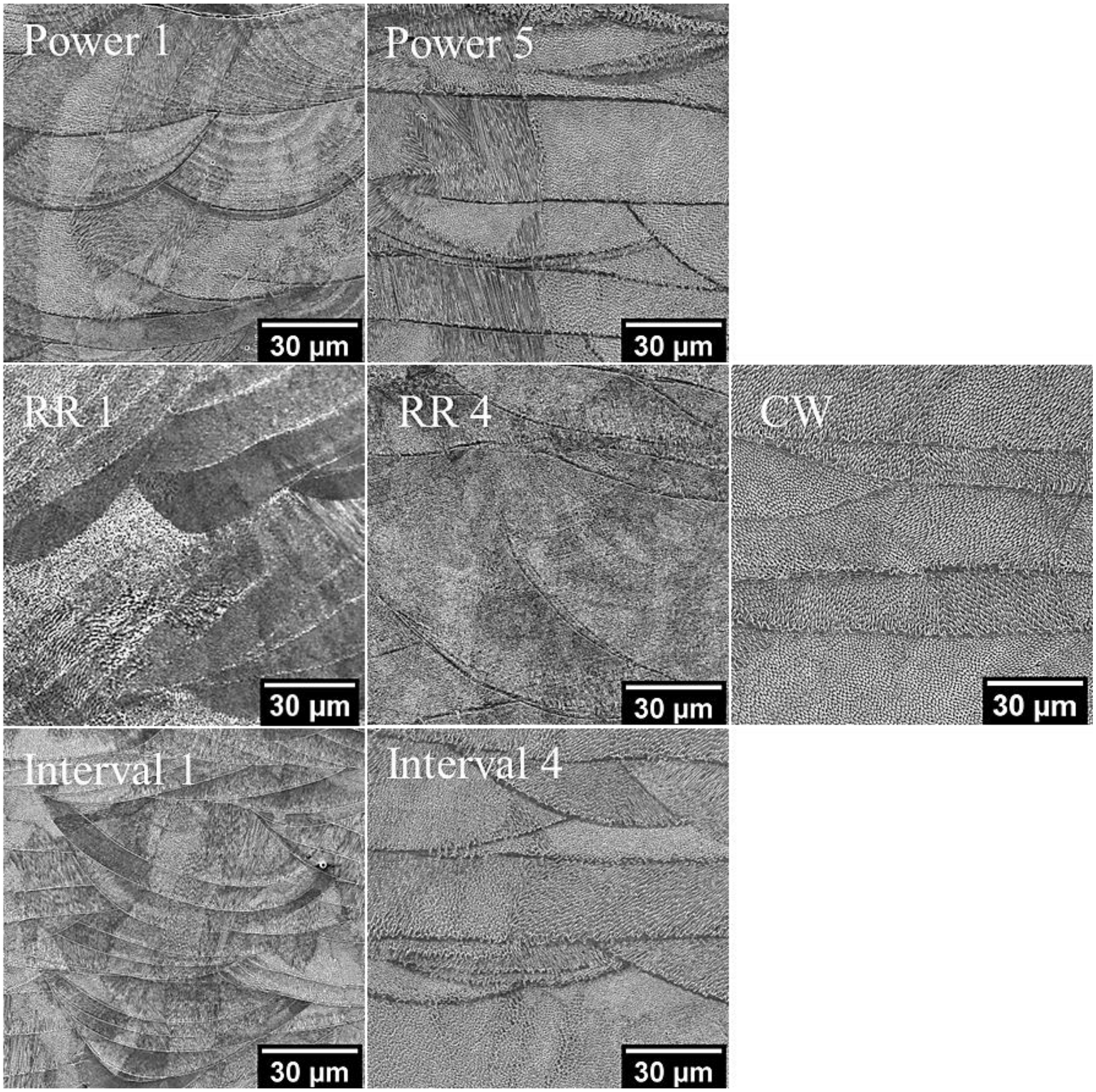

Fig. 6-13 Melt pool structure of pulse laser L-PBF 316L SS with different printing parameters: power, pulse interval, pulse width, and repetition rate.

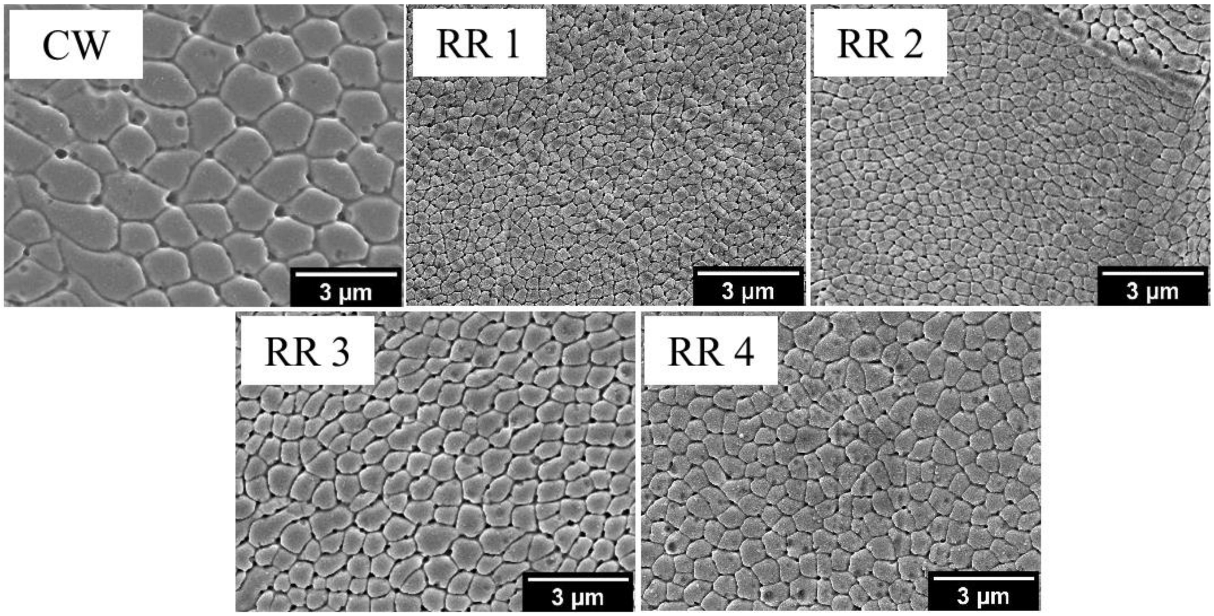

Fig. 6-14 Cellular structure of CW and pulse laser L-PBF 316L SS with different repetition rates.

Beyond the melt pool structure, subgrain dislocation cellular structures were also affected by PW laser parameters. The mechanical properties of AM 316L SS are primarily controlled by the cellular structures [124]. Fig. 6-14 shows the change of cellular structure in AM 316L SS as the function of PW laser repetition rate. Energy input was kept the same for these studies. Compared to CW laser AM, a significant decrease in cell size was obtained by a pulse laser.

Fig. 6-15 summarizes the average cell size with different PW and CW laser parameters. The cell size was calculated using Image J, based on the linear intercept method defined in ASTM E112. This analysis was performed only on the cellular/columnar structures oriented perpendicularly to the polished surface. Six to ten SEM images were randomly acquired from each specimen to arrive at a statistically meaningful description of the cellular structure. As shown in the figure, the cell size created by PW laser AM is finer than that created by CW laser AM. The comparison was done in the same AM system with other parameters to be fixed. A reduced laser power, repetition rate, or an increased pulse interval is beneficial to refine the cell size. The refined cell size suggests that higher cooling rates were achieved by a pulse laser.

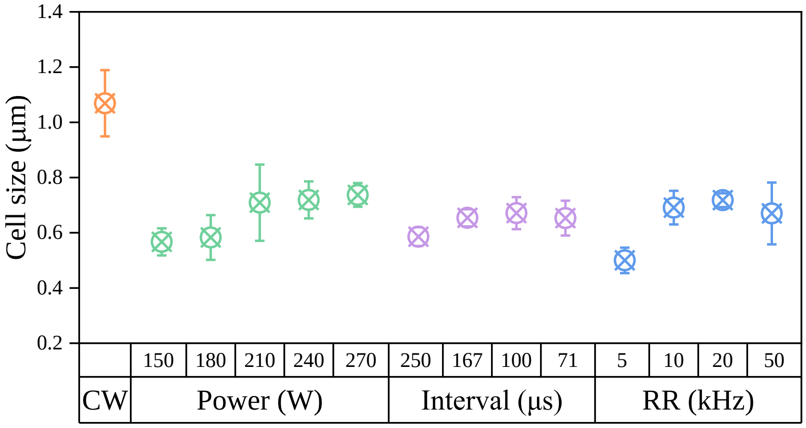

Fig. 6-15 Cell size of CW and pulse laser L-PBF 316L SS with different printing parameters: power, pulse interval, pulse width, and repetition rate.

6.6 Conclusion

The effects of pulse laser parameters, especially the power, pulse interval, pulse width, and repetition rate, on the quality, microstructure, and mechanical properties of AM 316L SS are studied. And the general conclusions are addressed below:

1) The single laser track scan provides valuable information for the parameters screening. The parameters generate a continuous and smooth laser track that could be used for fabricating bulk samples with appropriate layer thickness and hatch spacing.
2) Power, pulse interval, pulse width, and repetition rate all significantly affect the part density. Dense materials can be fabricated in a wide range of linear power densities with different combinations of pulse laser parameters.

3) Improved mechanical properties of PW L-PBF 316L with refined cell size suggest that pulse laser has the advantage of enhancing the cooling rate of the L-PBF process.

CHAPTER 7

EFFECTS OF PULSE WAVE LASER PARAMETERS ON IN-SITU AND EX-SITU L-PBF ODS STEEL

PW laser with different parameters has been used to fabricate dense 316L SS in Chapter 6. The refined microstructure and improved mechanical property indicate the PW can change the temperature field and cooling rate of the melt pool compared to the CW laser. We believe PW laser would also benefit the optimization of oxide distribution in the AM ODS steel. The melting point of the solid-oxygen donor was also hypothesized to affect the efficiency of fabricating ODS steel by L-PBF. In this chapter, the effects of different PW laser parameters on the densification behavior, oxide size, distribution, and mechanical properties of L-PBF ODS steels were studied. Low melting point solid-donor Fe_2O_3 nanoparticles provide oxygen for in-situ reacted ODS steel. Sample fabricated by using a mixture of 316L SS powder and Y_2O_3 nanoparticles is designated as ex-situ ODS steel.

7.1 Density of AM ODS SS as the function of PW laser parameters

Fig. 7-1 shows the part density of both in-situ and ex-situ AM ODS SS made with different PW laser parameters. The targeted Y_2O_3 amount in both in-situ and ex-situ AM ODS SS was 2 wt.%. For in-situ AM ODS SS, 1.57 wt.% yttrium powder and 3.3 wt.% Fe_2O_3 nanoparticles were mixed with 316L SS feedstock powders. For ex-situ AM ODS SS, 2 wt.% Y_2O_3 was milled with 316L SS feedstock powder. In both processes, part density improved with the increase of PW laser power, pulse width, and the decrease in pulse interval. At laser power of 150 W, the part density of AM ODS SS samples was significantly lower than that of AM 316L SS (see Fig. 6-10). This suggests that higher energy is required for ODS SS to obtain a similar quality of 316L SS due to the high melting points of the additives such as yttrium (T_m=1526°C) and Y_2O_3 (T_m=2425°C), and Fe_2O_3 (T_m=1565°C). In many cases, in-situ ODS SS made by reactive AM developed a lower part density than ex-situ ODS SS, which may be caused by the higher amount of oxides in the feedstock powder.

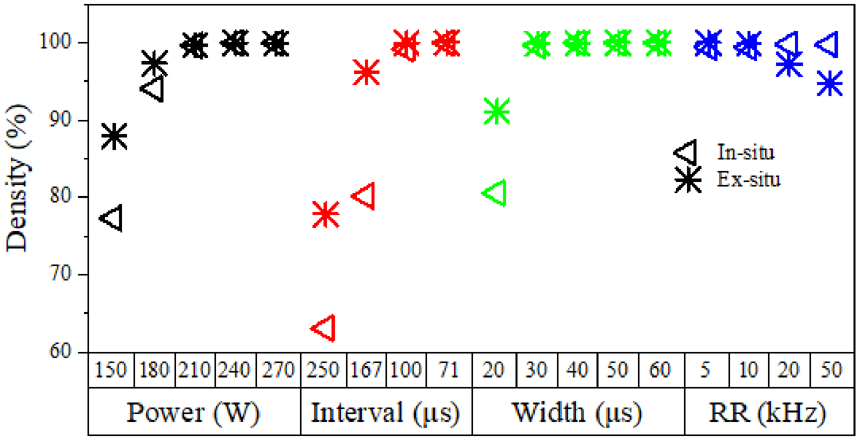

Fig. 7-1 Density of in-situ and ex-situ L-PBF ODS samples with different printing parameters, power, pulse interval width, and repetition rate.

Samples with a density lower than 90% affect mechanical properties, especially for the in-situ ODS steel. No reaction or partial reaction between yttrium and oxygen donor may occur under low energy conditions. In many conditions, fully dense parts can be obtained without defects and agglomeration.

7.2 Effects on the Mechanical Properties

Nanoindentation was performed on AM ODS SS by PW laser AM. The effects of laser power, pulse interval, pulse width, and repetition rate on the in-situ and ex-situ L-PBF ODS steels are discussed.

7.2.1 Power Effect

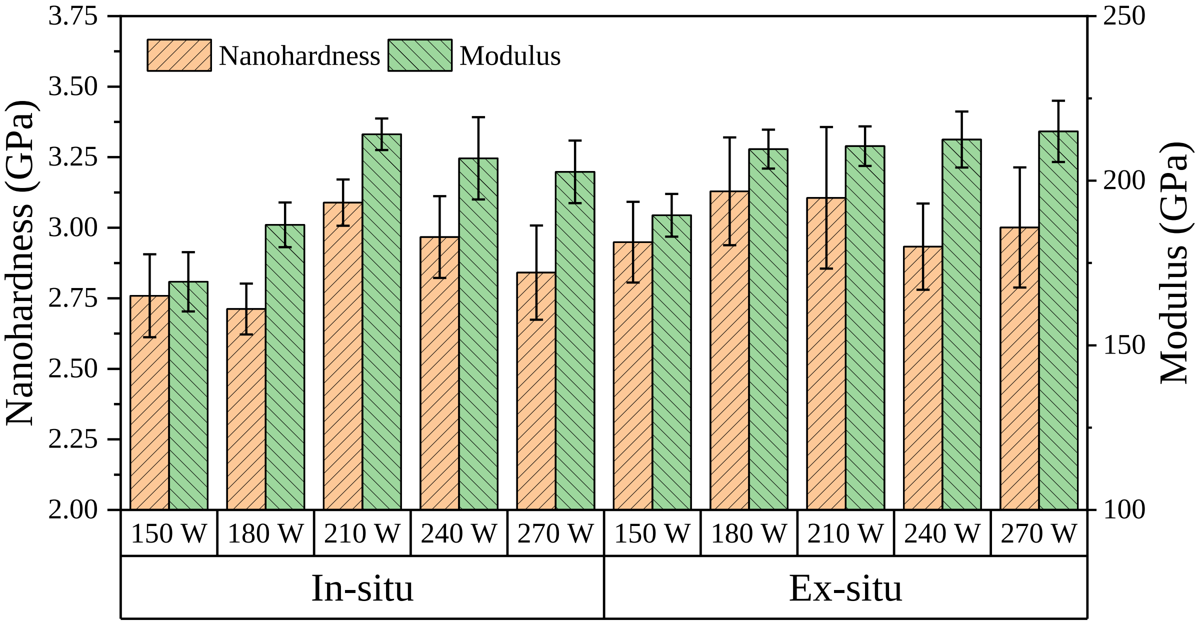

Fig. 7-2 Nano hardness and modulus of pulse laser L-PBF in-situ and ex-situ ODS steel with different powers.

At a lower laser power of 150 and 180 W, the in-situ ODS samples show remarkably lower hardness and modulus than the others, and their hardness of ~2.75 GPa was even lower than that of AM 316L SS made by PW laser (Fig. 6-10), which was likely due to high porosity and less oxide formation. A reduction of hardness was also observed with high laser power. A similar trend was observed in the ex-situ AM ODS SS samples.

7.2.2 Pulse Interval Effect

An increased modulus of the in-situ samples was observed by reducing the pulse interval from 250 to 71 μs, which is probably due to the high sensitivity of modulus to part density (Fig. 7-1). Hardness peaked at 3.25 GPa when the pulse interval reached 71 μs. The relationship between hardness and pulse intervals of the in-situ AM ODS SS is identical to AM 316L SS by PW laser (Fig. 6-12(a)). Ex-situ AM ODS SS presented a different trend than in-situ formed material. The reduction of pulse interval reduced the overall hardness. The relationship between nano hardness and pulse interval cannot be derived from the figure in the in-situ AM ODS steel, as the in-situ reaction was affected by the total energy input.

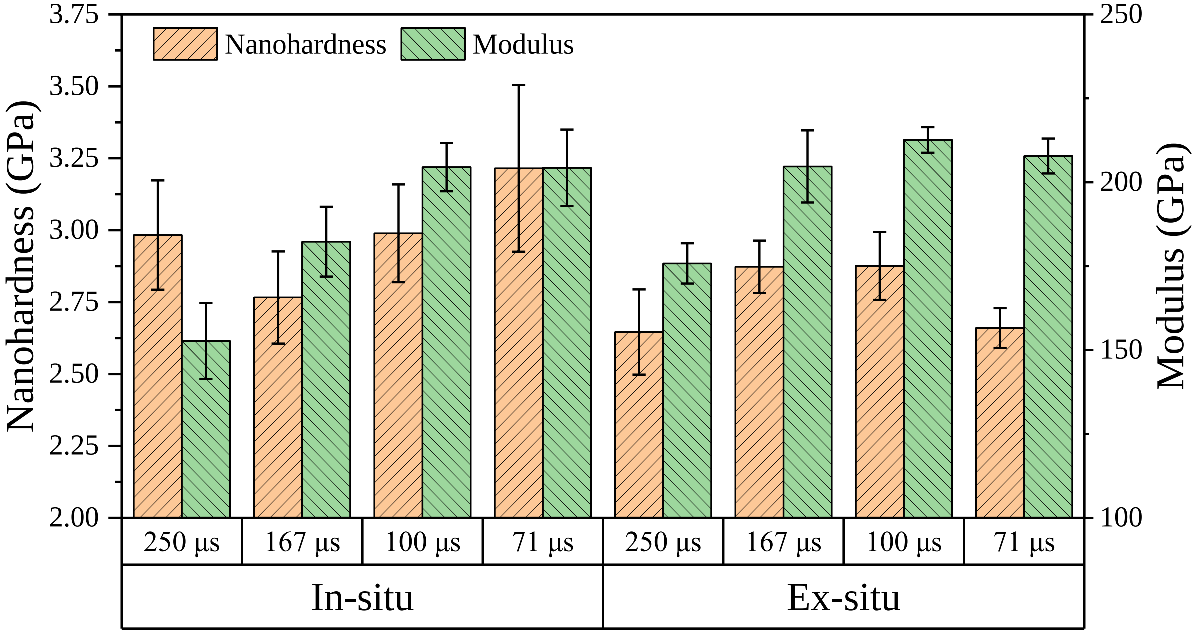

Fig. 7-3 Nano hardness and modulus of pulse laser L-PBF in-situ and ex-situ ODS steel with different pulse intervals.

7.2.3 Pulse width Effect

Nano hardness and modulus of the in-situ and ex-situ PW ODS steel with different pulse width is shown in Fig. 7-4. Dense parts with a pulse width higher than 30 μs show a slight difference in the nano hardness, but an increase in modulus of the in-situ samples was observed. An apparent drop in the hardness of the ex-situ samples was observed when the pulse width increased to 40 μs. Due to the limitation of the laser generator, the change from 20 μs to 60 μs may not affect the hardness too much, especially for the in-situ ODS steel and PW 316L SS (Fig. 6-12 (a)). Three orders difference in pulse width from 800 ps to 500 fs was reported to increase ~27.5% hardness in Al-Si alloy [83].

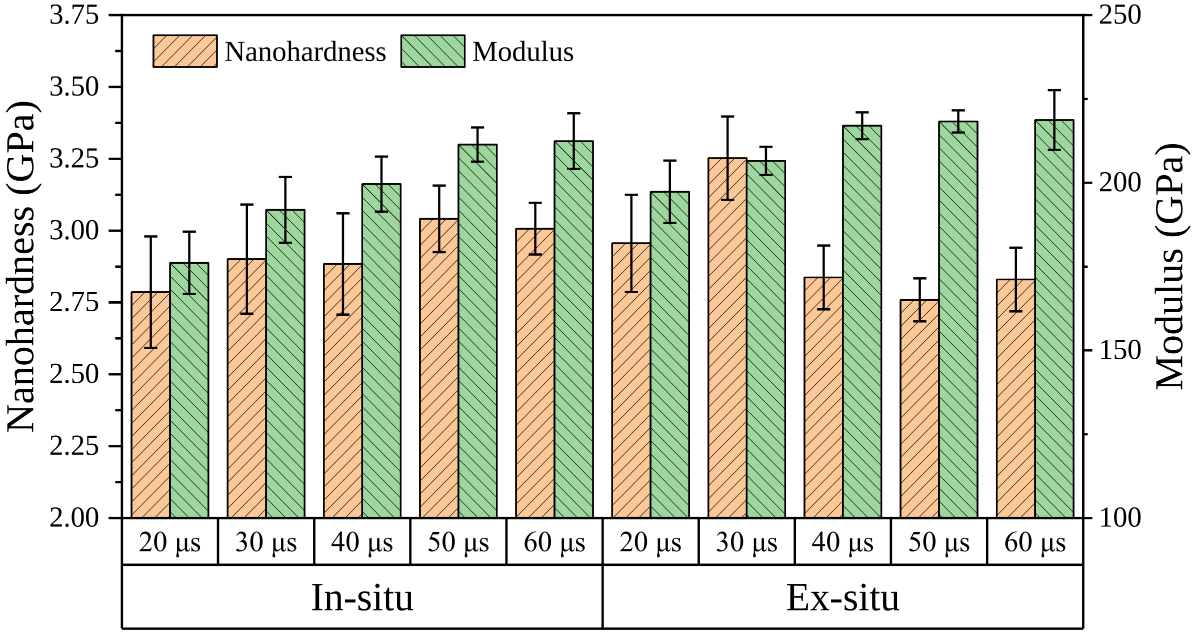

Fig. 7-4 Nano hardness and modulus of pulse laser L-PBF in-situ and ex-situ ODS steel with different pulse widths.

7.2.4 Repetition rate Effect

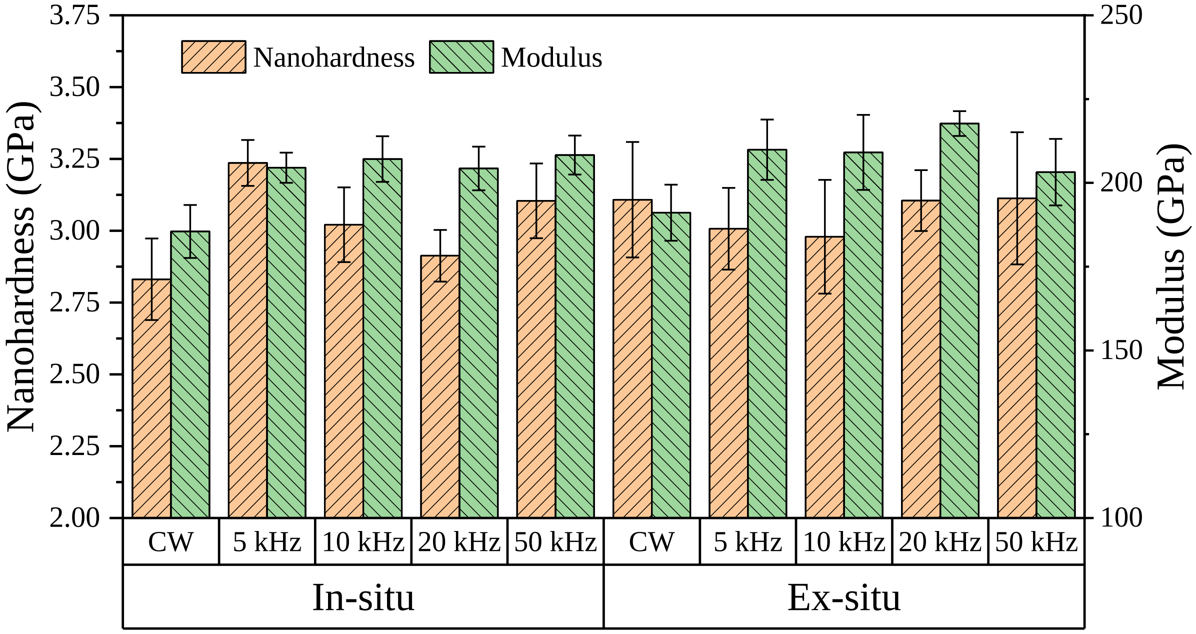

Fig. 7-5 Nano hardness and modulus of pulse laser L-PBF in-situ and ex-situ ODS steel with different repetition rates.

Fig. 7-5 shows the effects of repetition rates on the nano hardness and modulus of the in-situ and ex-situ PW ODS steels. The CW condition was also plotted together to compare with the PW conditions. All the samples shown in Fig 7-5 have good quality, and the effects of defects/density on the hardness can be neglected. In the in-situ samples, PW samples with different repetition rates have higher hardness than the CW sample. And the hardness decreases when the repetition rate increases from 5 kHz to 20 kHz, but a different trend was observed when continuing to increase the repetition rate to 50 kHz. A non-linear relation between the hardness and repetition rate of in-situ ODS steel is expected as the PW laser parameters are complicated. The pulse width and pulse interval will change with the repetition rate as the linear energy input is a constant among these samples. The hardness of the ex-situ PW samples with different repetition rates and a CW sample is very close.

In general, the mechanical response of the in-situ PW ODS steel was very similar to that of PW 316L SS (discussed in Chapter 6). The effects of pulse interval and repetition rate on the mechanical properties of the in-situ and ex-situ PW ODS were different. This suggests that in some conditions, the oxide and microstructure evolution during the L-PBF process of the in-situ and ex-situ samples can be different due to the different melting pointing points between the Y_2O_3 (T_m=2425°C) and Fe_2O_3 (T_m=1565°C) oxides.

7.3 Oxide Distribution

Fig. 7-6 shows SEM images of the in-situ and ex-situ samples with different laser and printing parameters. The black dots were oxide particles embedded in the steel matrix. Spherical oxides were randomly distributed in the matrix in all samples. Coarse oxides are observed under the CW mode of both in-situ and ex-situ ODS steels. In contrast, fine oxide particles are formed under PW mode, and different repetition rates also affect the oxide size and density. It’s also evident that oxide density in the ex-situ sample is much less than that in the in-situ sample under the same printing conditions. The kinetics of oxide particles precipitation in the melt pool is not well understood. Some researchers have performed parametric studies such as the effect of AM parameters and alloy composition on the oxide particle size distribution[141–143]. Comparative studies were also reported between different AM processes [4] to understand particle formation and evolution processes. However, methods to reduce the size of the oxide particle have not been found, and analysis of nucleation and growth behavior of the oxide particles in the L-PBF process is lacking. The oxide size and distributions of different PW laser parameters, especially with different repetition rates and pulse intervals, were summarized and a possible pathway to refine the oxide size in L-PBF ODS steel is proposed.

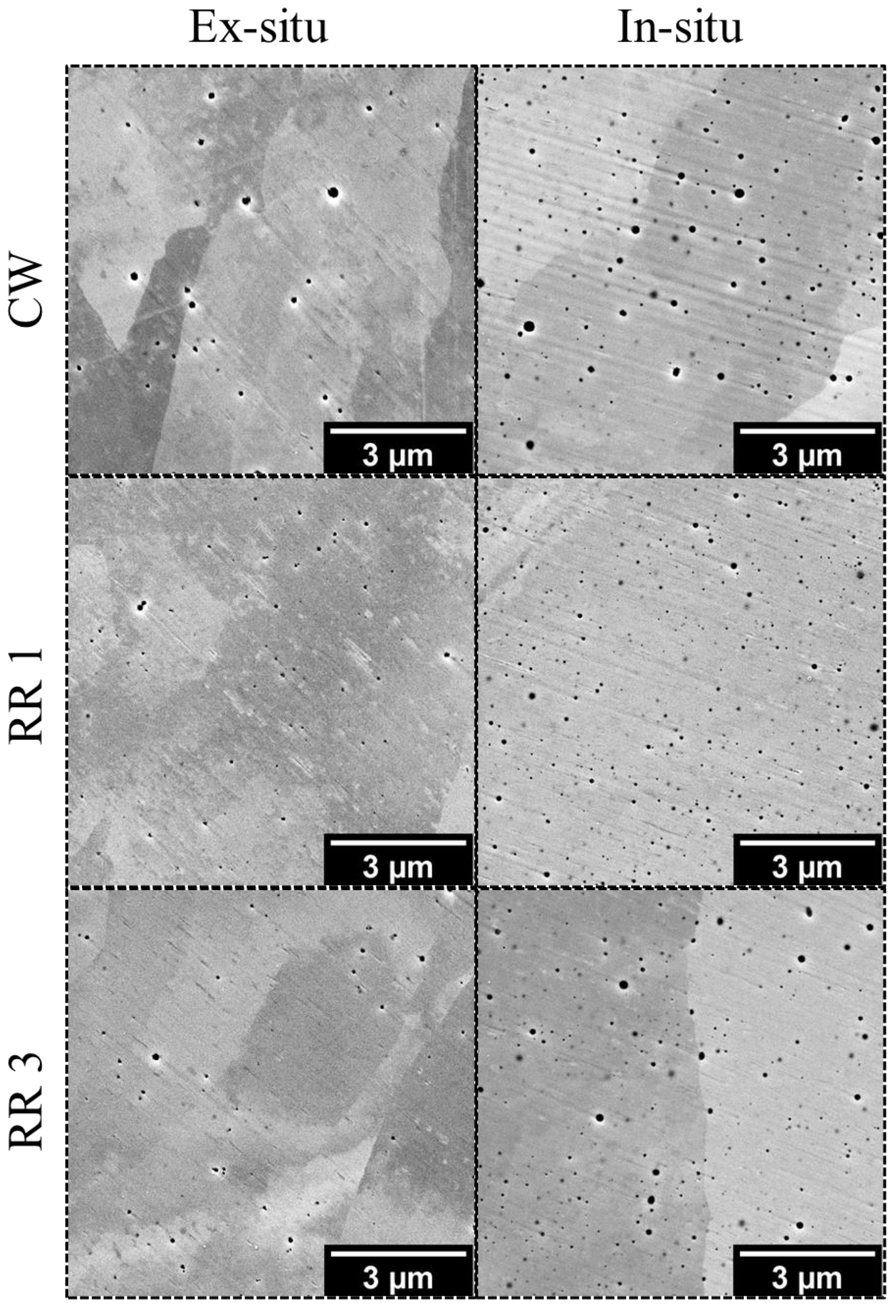

Fig. 7-6 SEM images show the distribution of oxide (black dots) in-situ and ex-situ L-PBF ODS samples with CW and PW laser.

Fig. 7-7 shows the oxide distribution and summary of oxide size and density in CW and PW in-situ samples with different repetition rates. The oxide size and density were analyzed from the SEM images by using open-source software ImageJ. Due to the resolution limit of the SEM, oxide with a size less than two pixels (~18 nm) cannot be detected; hence the actual mean oxide size should be smaller, and the oxide density should be higher than the results shown below. The average oxide size in diameter of the CW sample is ~75 nm. The size can be refined to ~48 nm using a PW laser with a repetition rate of 5 kHz. When the repetition rate increases from 5 kHz to 20 kHz, the peak frequency of oxide size shifts to a larger value, and the number density decreases. Further increase in the repetition rate will alter the trend and refine the oxide again. The highest oxide density is 5 per micron square with a repetition rate of 5 kHz.

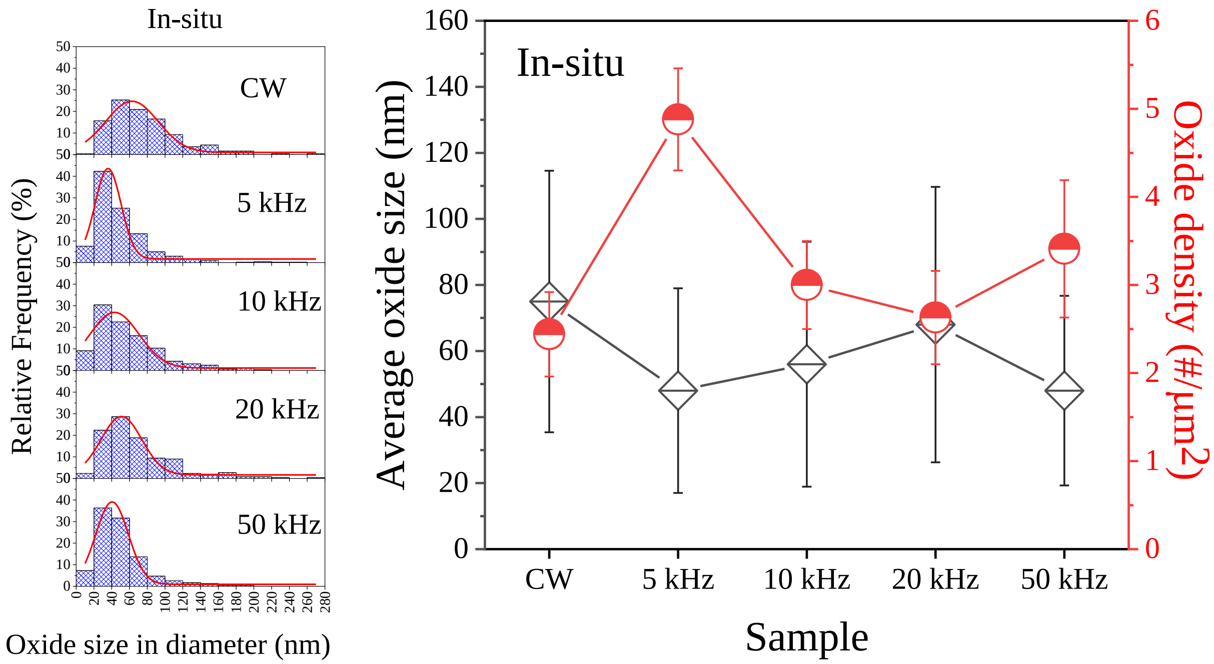

Fig. 7-7 Oxide distribution and density of in-situ L-PBF ODS samples with different repetition rates.

In the ex-situ L-PBF ODS sample, CW laser generates much larger oxides with an average diameter of ~81 nm, about two times larger than PW counterparts with repetition rates of 5 kHz. The size was also larger than that of the feedstocks Y_2O_3 nanoparticles (30-45 nm), suggesting that the Y_2O_3 melted and reprecipitated during the laser process. The oxide density in the ex-situ ODS steel is about 5-10 times less than that of the in-situ samples, which shows the advantage of increasing oxide density by using in-situ reaction methods. The effects of repetition rate on the oxide size and density in the ex-situ samples are almost identical to that on the in-situ sample.

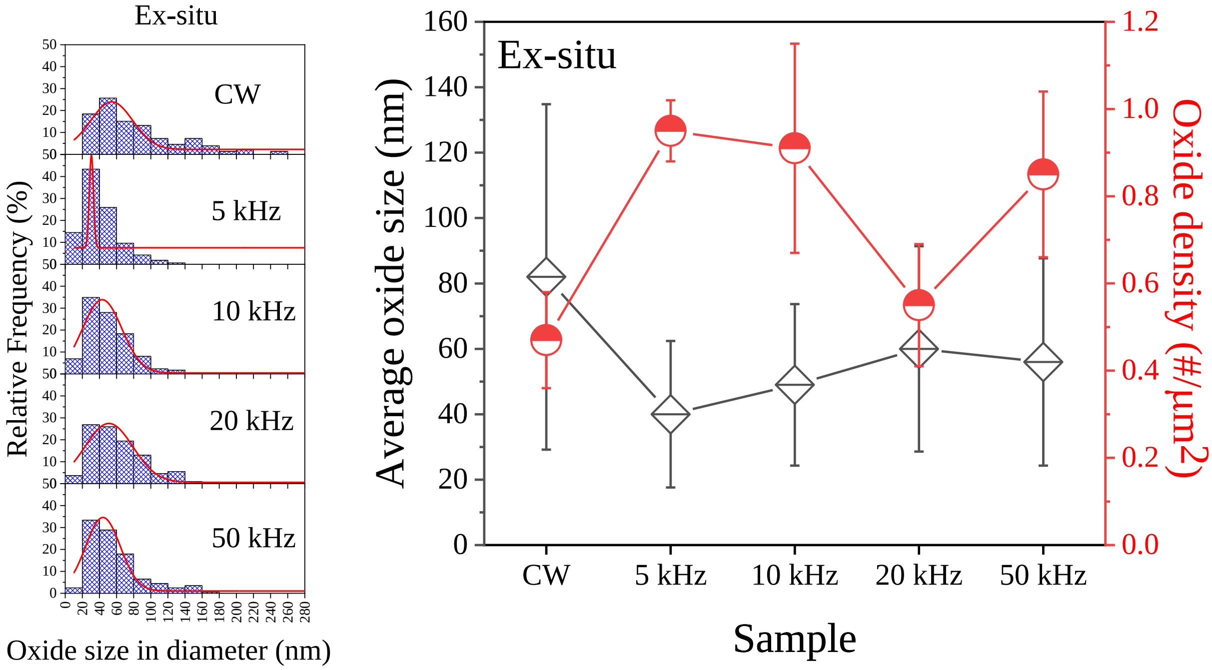

Fig. 7-8 Oxide distribution and density of ex-situ L-PBF ODS samples with different repetition rates.

The effects of the pulse intervals on the oxide distribution and number density of in-situ samples are shown in Fig. 7-9. The extremely low density (Fig. 7-1) of the samples with pulse intervals of 250 μs and 167 μs suggests the powders are not fully melted, and hence the reaction between the oxygen and yttrium is insufficient. The oxides observed in the sample can be from the feedstock 316L SS powders. The reduction of the pulse interval also provided higher energy for melting the powders and reaction between oxygen and yttrium, but it also reduces the cooling time between two laser spots, and hence the oxide can grow larger. A shorter pulse interval of 71 μs yields ~27% larger oxide size compared to that in samples with a 100 μs interval. This is further proved in the ex-situ samples, as shown in Fig. 7-10.

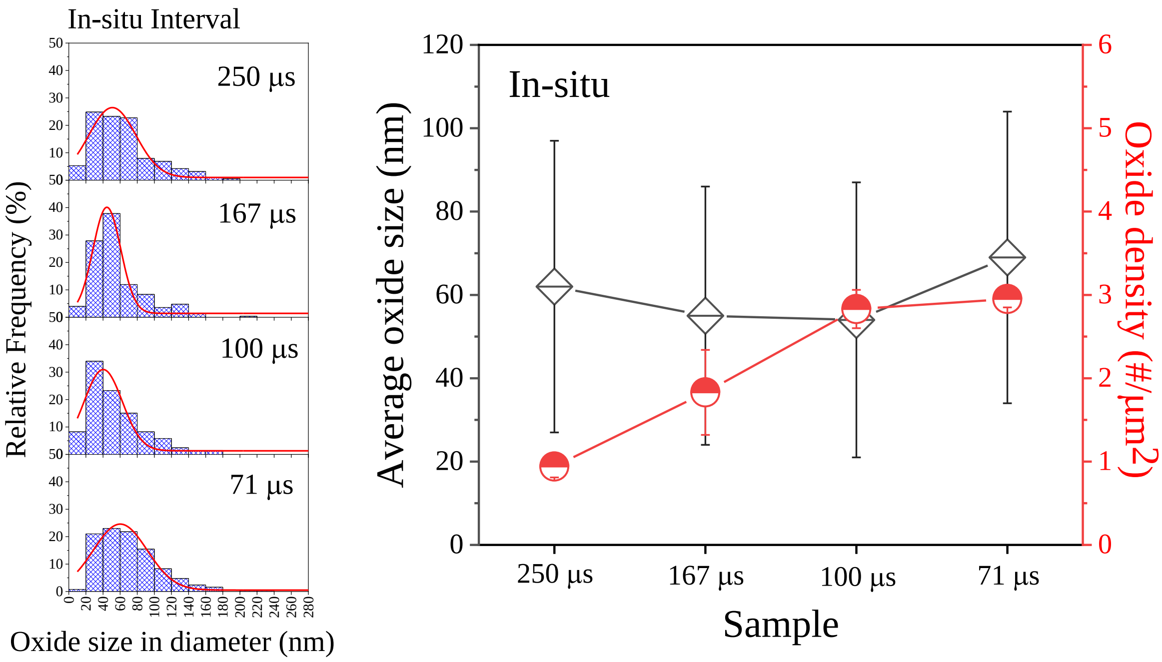

Fig. 7-9 Oxide distribution and density of in-situ L-PBF ODS samples with different pulse intervals.

In the ex-situ L-PBF ODS steel, the pulse interval affects the oxide size significantly, a remarkable refinement of the oxides is achieved in the sample with a 250 μs pulse interval. A negative correlation between oxide size and pulse interval is apparent as shown in Fig. 7-10. The cooling time/pulse interval between two laser spots will affect the temperature profile of a fixed point in the melt pool, and it would be very interesting to understand whether the pulse interval modified the duration of the metal in the liquid phase or the cooling rate. This can provide guidance for L-PBF ODS steel with PW laser. A melt pool simulation with Flow-3D under different parameters was conducted, and a representative temperature profile at different depths of the melt pool is shown and discussed in chapter 8.

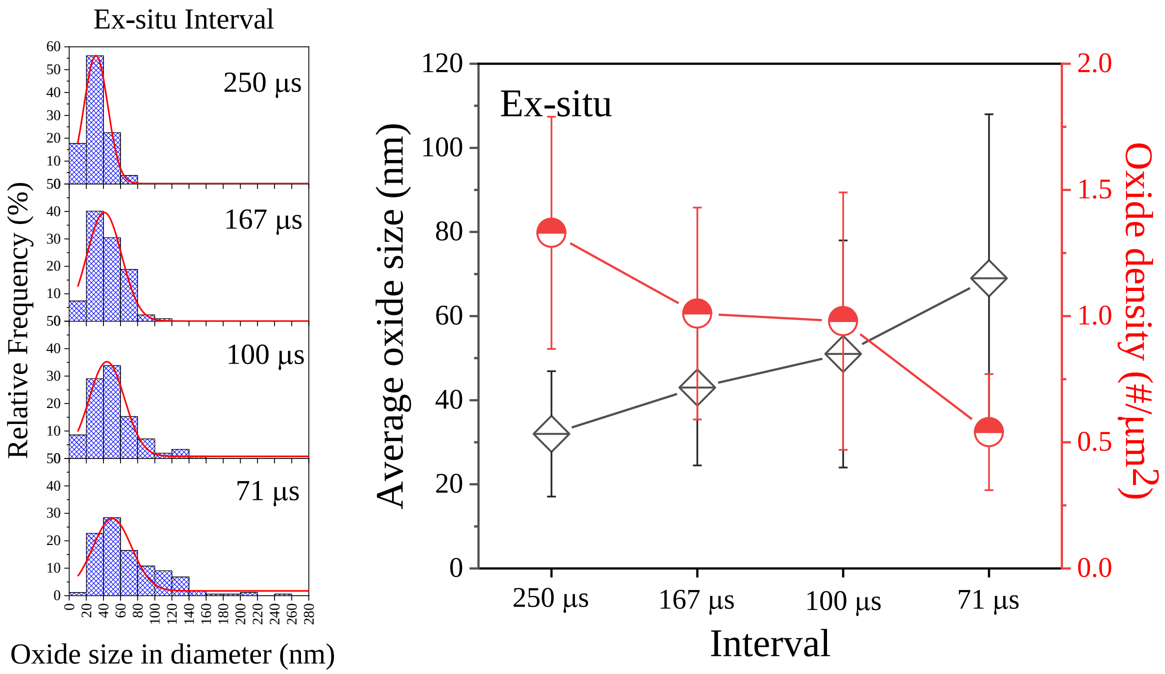

Fig. 7-10 Oxide distribution and density of ex-situ L-PBF ODS samples with different pulse intervals.

7.4 Spatter Powders

Fig. 7-11 shows the ball-milled feedstock powder and spatter powders of the ex-situ ODS sample. The spatters carried away by shield gas flow and piled up on the edge of the chamber were collected. The ball-milled powder with the ball to powder ratio of 5:1 and speed of 200 rpm for 2 h remains spherical shape, as shown in Fig. 7-11(a). Most fine Y_2O_3 particles were found sticking on the steel particles, whereas some also formed micro-sized agglomerates. The observed spatters are slightly larger than the feedstock powder. Some of the spatters have a rougher surface, while others are smooth but with a satellite or hemispherical cap on the surface. The energy dispersion spectroscopy (EDS) analysis carried out on the feedstock powder and spatter surface marked as "Y-O" and "Spatter Y-O" in Fig. 7-11 (b) and (d) are shown in Fig. 7-12. The Y:O ratio of 20.3: 79.7 in the feedstock powder is almost identical to the stoichiometric ratio in Y_2O_3. In the spatter powder, the Y:O ratio changed, and Fe was also detected in the agglomerate.

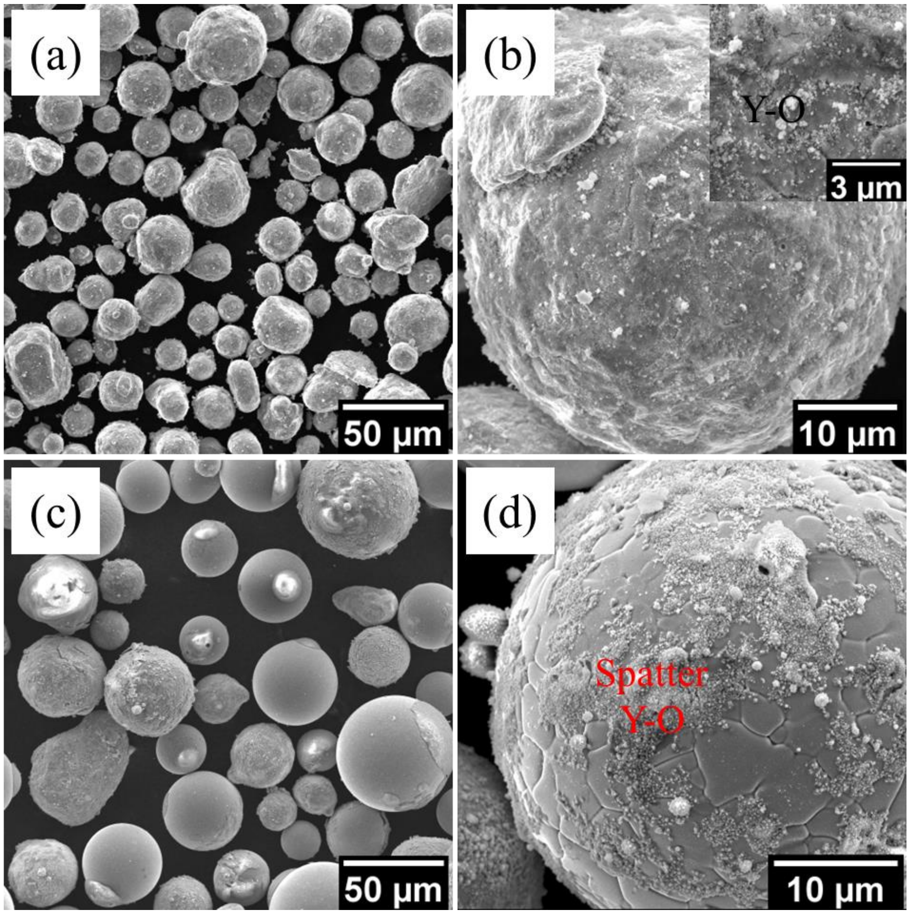

Fig. 7-11 Feedstock powders and spatters of ex-situ sample.

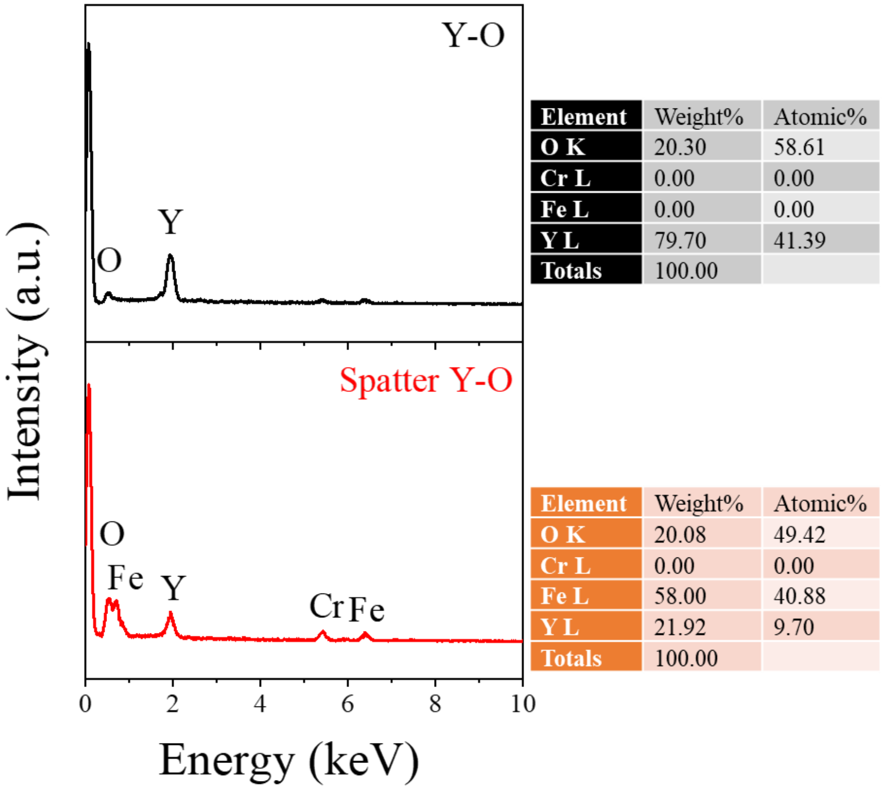

Element	Weight%	Atomic%
O K	20.30	58.61
Cr L	0.00	0.00
Fe L	0.00	0.00
Y L	79.70	41.39
Totals	100.00	

Element	Weight%	Atomic%
O K	20.08	49.42
Cr L	0.00	0.00
Fe L	58.00	40.88
Y L	21.92	9.70
Totals	100.00	

Fig. 7-12 EDS point analyses marked with “Y-O” and “Spatter Y-O” in Fig. 7-11.

Like the ex-situ feedstock power, the in-situ one has a similar size and morphology but with different decorates of Fe_2O_3 and yttrium powder on a 316L SS powder surface. The spatters of the in-situ sample have a much larger size than the feedstock and can be ~120 µm, two or three times larger than the feedstock powder. A larger hemispherical cap than that in the ex-situ spatter with thickness up to 20 µm can be observed in the in-situ spatter. EDS point analysis shows oxide agglomerates with different compositions. The hemispherical cap is Y-Si-Mn-O agglomerate, while the spots on the spatter surface are Y-Si-O agglomerate. Alloying elements from 316L SS powder like Cr and Fe were also detected in the large agglomerates. Different composition of agglomerates in the in-situ and ex-situ spatters suggests that the oxygen transferring or oxide evolution in these two different samples can be different and might be affected by the melting points of the oxides and oxygen content in the melt pool. Spatters with large oxide agglomerates will consume a lot of oxygen and reduce the oxygen content in the melt pool, which is harmful to increasing the oxide density in the L-PBF ODS steels.

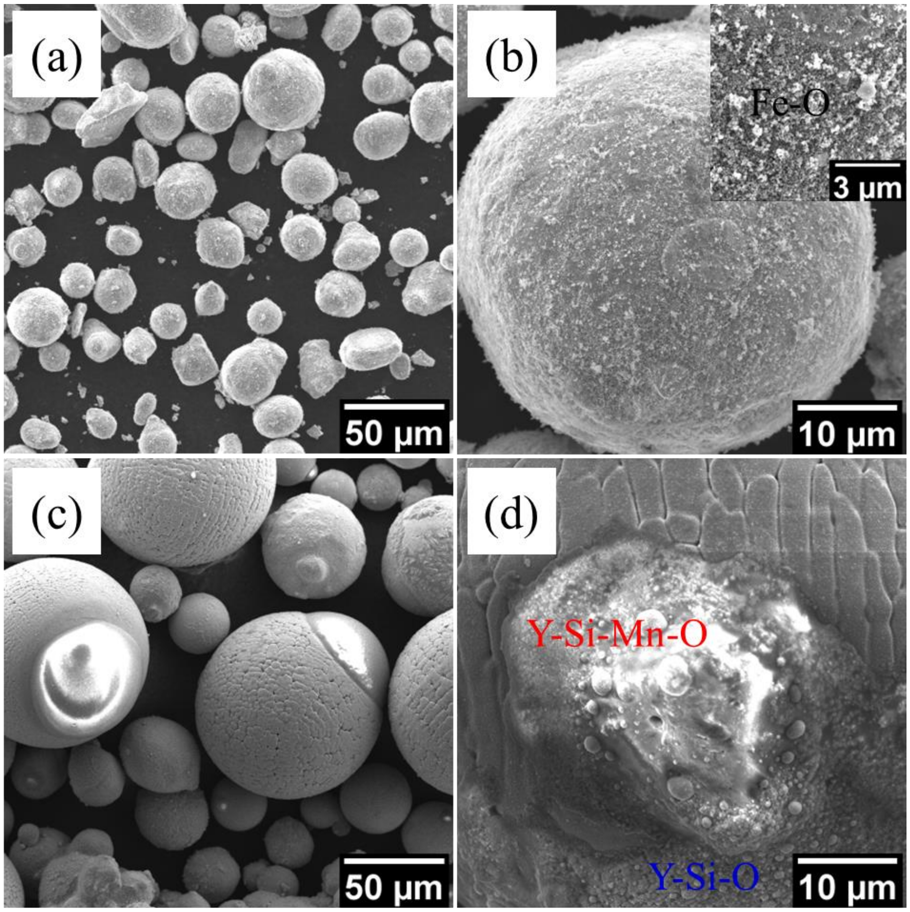

Fig. 7-13 Feedstock powders and spatters of the in-situ sample.

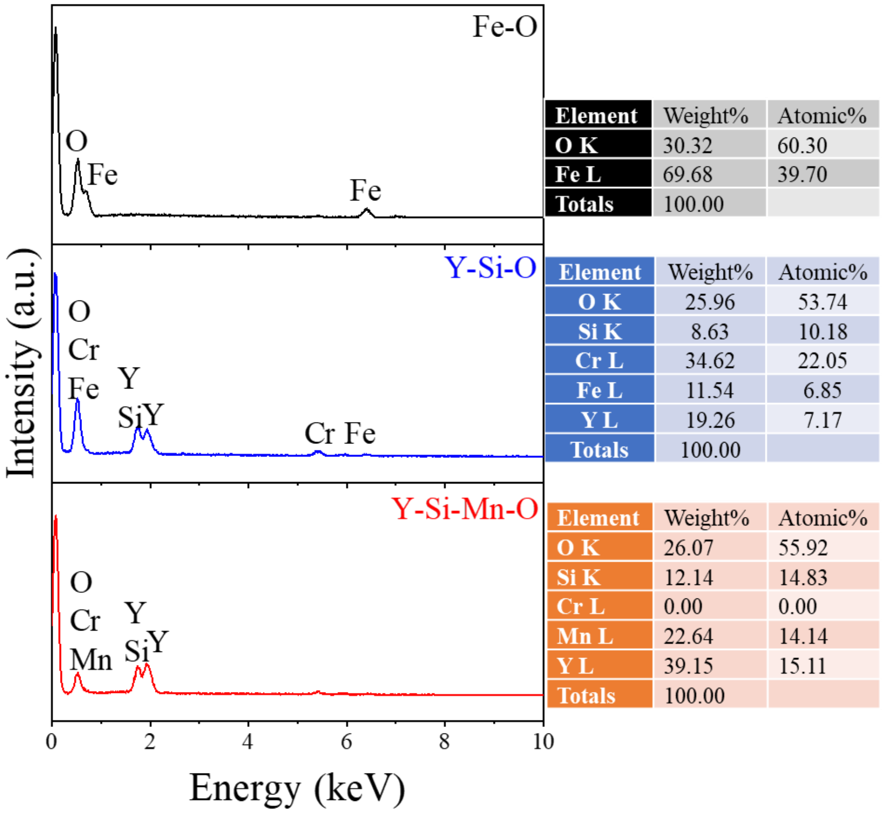

Element	Weight%	Atomic%
O K	30.32	60.30
Fe L	69.68	39.70
Totals	100.00	

Element	Weight%	Atomic%
O K	25.96	53.74
Si K	8.63	10.18
Cr L	34.62	22.05
Fe L	11.54	6.85
Y L	19.26	7.17
Totals	100.00	

Element	Weight%	Atomic%
O K	26.07	55.92
Si K	12.14	14.83
Cr L	0.00	0.00
Mn L	22.64	14.14
Y L	39.15	15.11
Totals	100.00	

Fig. 7-14 EDS point analyses marked with “Fe-O,” “Y-Si-O,” and “Y-Si-Mn-O” in Fig. 7-13.

7.5 Conclusion

In this chapter, the effects of PW laser parameters on the part quality, oxide size, distribution, and mechanical properties of the in-situ and ex-situ ODS steel were studied. The main conclusions are listed below:

1) Nearly defects-free bulk ODS steels can be fabricated by the L-PBF process with CW and PW lasers. Both the in-situ and ex-situ feedstock powder work for L-PBF ODS steels. PW laser has the advantage of reducing the oxide size, and the in-situ reaction method is superior to the ex-situ one in increasing the oxide density.

2) The modulus was sensitive to the part density, while the nano hardness was more affected by different pulse laser parameters. The different mechanical response and oxide distribution between the in-situ and ex-situ samples under the same parameters suggest that the oxide evolution during the PW L-PBF process is different.
3) The spatters with large oxide agglomerates on the powder surface suggest oxygen loss during the L-PBF process, which is harmful to increasing the oxide density of L-PBF ODS steel.

CHAPTER 8

MECHANISTIC INSIGHTS TOWARDS ENABLING SUCCESSFUL NANO OXIDE DISPERSION DURING LASER MELTING

Oxide refinement and improving the oxide volume fraction are two optimal goals in AM ODS steel. Refined oxides achieved by PW laser suggest the changing of the thermal history of the melt pool, which influences the oxide formation kinetically. However, directly monitoring the temperature field of the melt pool is challenging. In addition, heavily oxidized spatters generated during the fabrication of ODS steel by L-PBF indicate a possible oxygen loss pathway by spattering. Reduced spattering was reported by using PW laser [144], but how different PW laser affects the spattering was not discussed. In this chapter, melt pool modeling of samples printed with different parameters was conducted to understand how the temperature field affects the oxide evolution. The spattering behavior of AM ODS steel with different PW laser parameters was also evaluated.

8.1 Spattering

Spatter creation has been reported in several laser-assisted manufacturing works [97]. Visible light, IR videography, and simulation have been used to determine the cause of spatter formation during the L-PBF process with continuous-wave lasers [98,145,146]. The oxidation of spatters was reported in AM 316L SS and AM Al alloys [97,147], contributing to the defect accumulation in the final parts. Within the laser welding of metal sheets, studies have shown that pulse lasers are beneficial in reducing spatter generation, porosity formation, and improvement of weld surface finish [144]. Very limited work to date has been conducted using pulse laser to process metal powders. There is still a gap in knowledge and an apparent need for a systematic analysis of spatter formation during the L-PBF process with pulse wave lasers. In this chapter, high-speed photography is utilized to realize the formation and behavior of spatter particles during the L-PBF process with different PW laser parameters.

8.1.1 Spattering of 316L SS and ODS Powders

Fig .8-1 shows the high-speed camera images of the melt pool spattering of different feedstock powders during the L-PBF AM process with the same set of CW laser parameters. The intensity of spattering near the melt pool could be evaluated visually. Six consecutive frames of the spattering event within 5 milliseconds are shown here to document the process. Results show that the fabrication of both in-situ and ex-situ AM ODS SS generates more spatters during the L-PBF process. The spattering height of AM 316L SS is slightly lower than AM ODS SS, with much less spattering density. Severe spattering during the manufacturing of ODS SS is concerning because it can not only induce more defects in the AM parts but also remove the oxides from the melt pool and reduce the overall oxygen level in the parts. Thus, it’s necessary to reduce the melt-pool spattering of AM ODS SS.

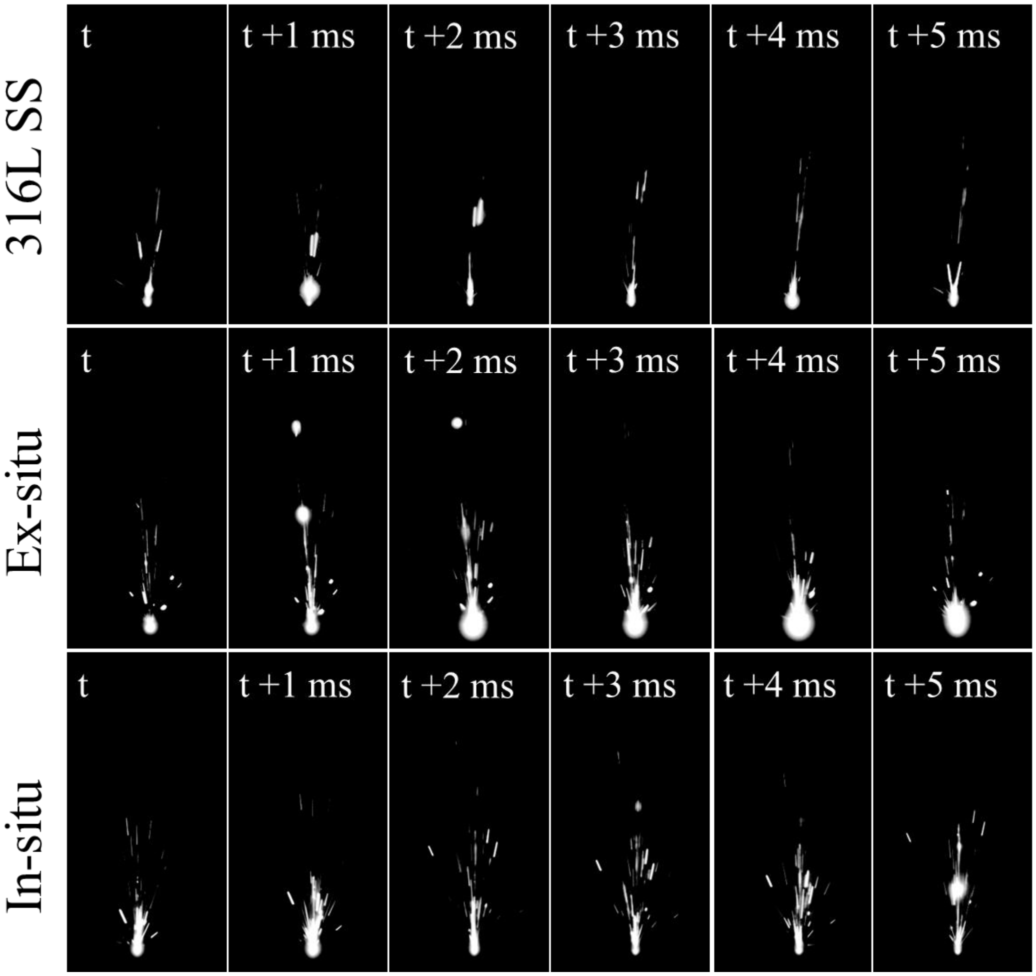

Fig. 8-1 High-speed camera images capture the dynamic variation of spattering with different feedstock powders: 316L SS, ex-situ, and in-situ ODS powders. (Images taken from the direction parallel to the scan direction)

8.1.2 Effects of Pulse Laser Power on Spattering

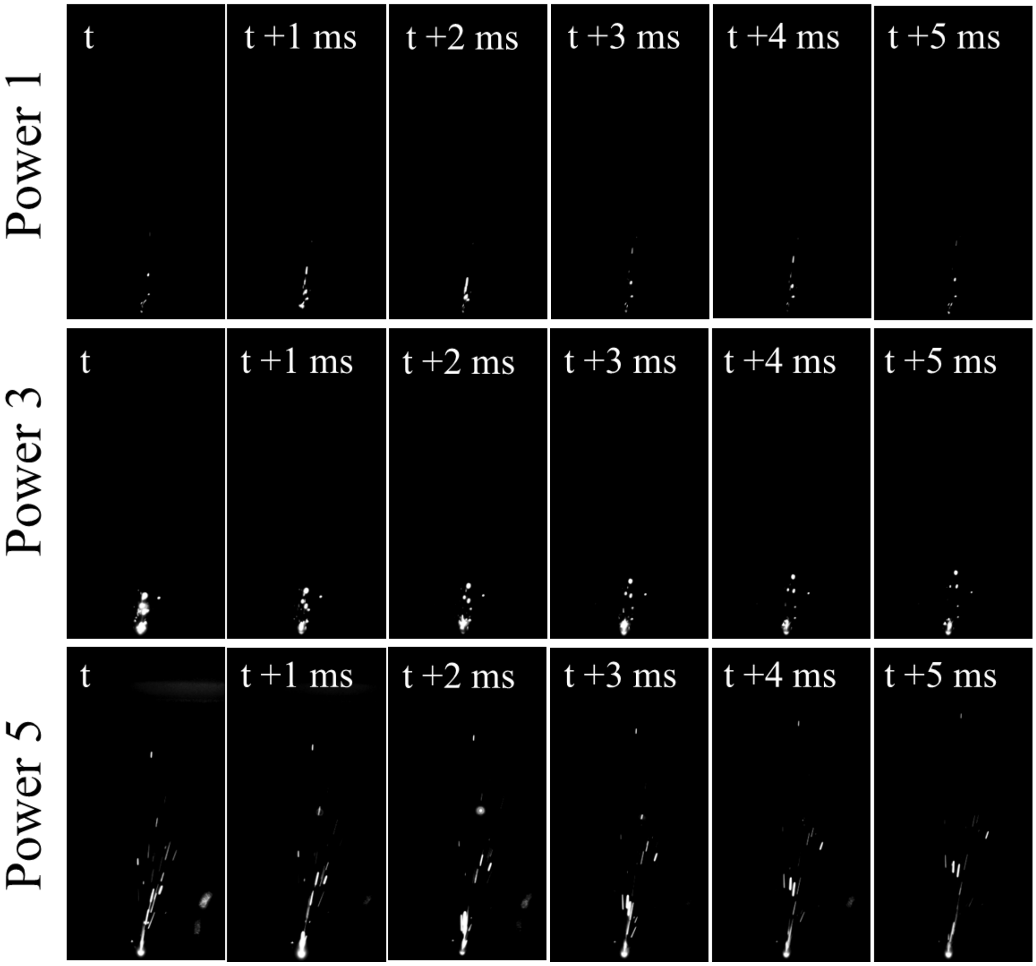

Fig. 8-2 High-speed camera images capture the dynamic variations of a spattering of in-situ ODS steel with different pulse laser power.

The roles of different pulse laser parameters on the spattering behavior of in-situ AM ODS SS were studied. The results were summarized in Fig. 8-2 to Fig. 8-5. In Fig. 8-2, different pulse laser powers were evaluated as other parameters were fixed constant. While the spattering angle was not changed much by laser power, high laser power increased the spattering height. The spatters created by higher laser power carried higher velocity. We estimated velocity by the travel distance of a particular spatter within the exposure time of 700 μs as shown in the figure. With the assumption that spatters carried oxides, high-velocity spattering removed more oxygen from the melt pool. We emphasize that PW laser reduced the melt-pool spattering as compared to CW laser, which benefits to retaining oxygen in the material.

8.1.3 Effects of Pulse Interval on Spattering

Pulse interval also affects the spattering behavior during the fabrication of in-situ AM ODS SS, as shown in Fig. 8-3. In this study, laser power and pulse width were fixed at 210W and 50 μs, respectively. A longer pulse interval of 250 μs (Interval 1) generates fewer spatters than a shorter one of 71 μs. At 71 μs, a wider spattering angle suggests an unstable melt pool was developed during laser melting. Pulse interval seems to affect the recoil pressure and/or the temperature distribution within the melt pool.

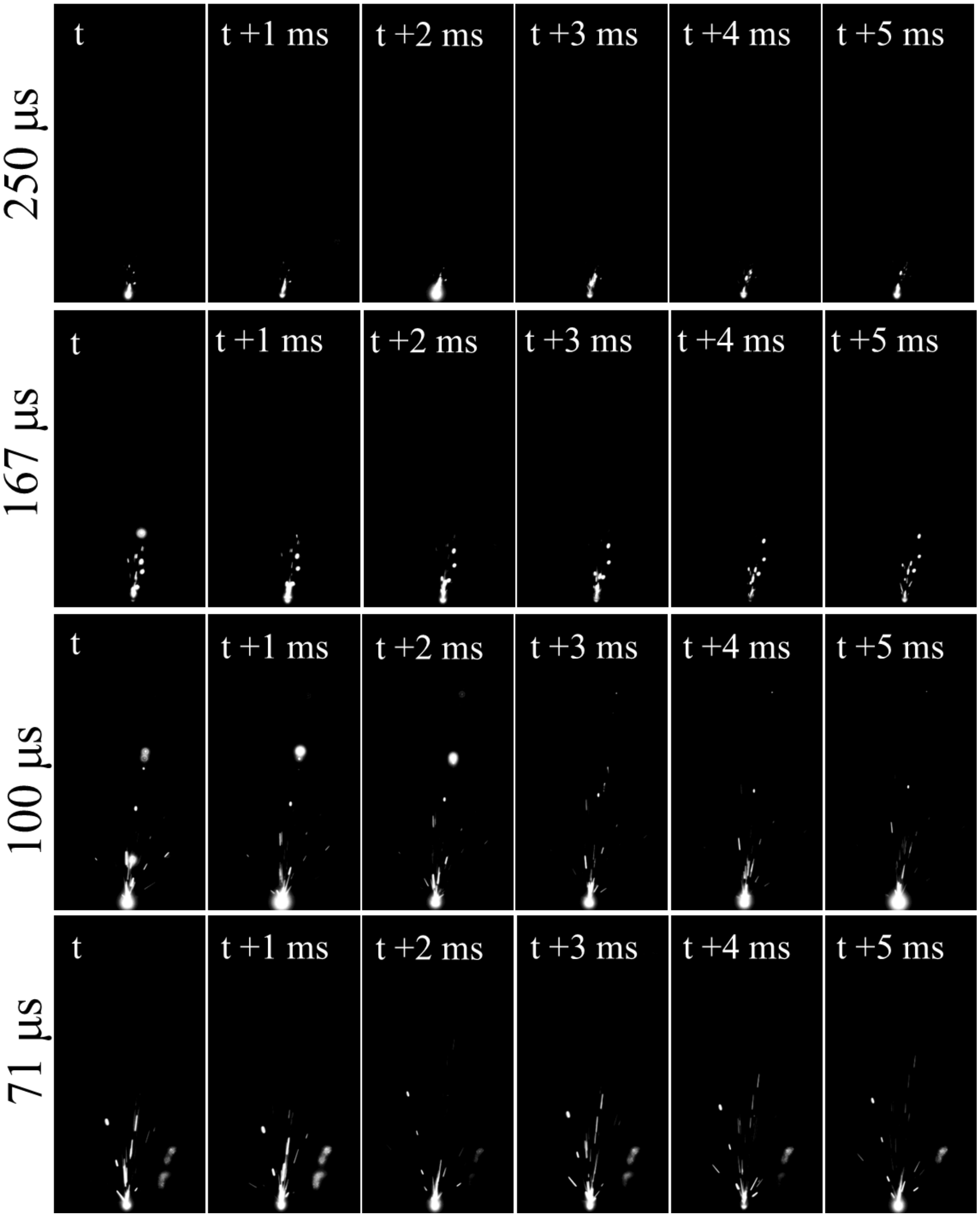

Fig. 8-3 High-speed camera images capture the dynamic variations of a spattering of in-situ ODS steel with different pulse intervals, 71, 100, 167, and 250µs.

8.1.4 Effects of Pulse Width on Spattering

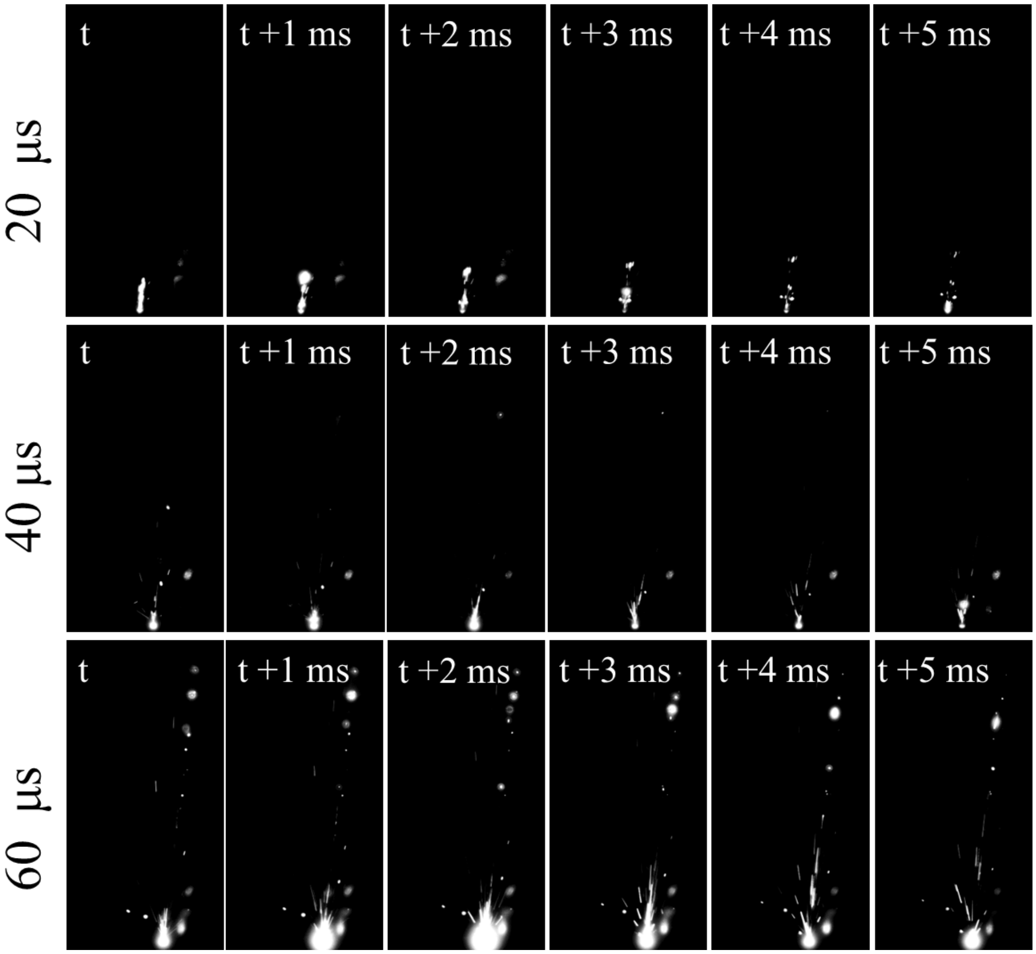

Fig. 8-4 High-speed camera images capture the dynamic variations of a spattering of in-situ ODS steel with different pulse widths, 20 40, and 60 μs.

In Fig. 8-4, the spattering velocity and spattering angle can both be increased by pulse width. In this study, laser power and pulse interval were fixed at 210W and 67 μs, respectively. At the longest pulse width of 60 μs, the melt pool became very unstable, leading to the melt droplet ejection in the farther distance along with both vertical and horizontal directions. The results in Sections 8.1.3 and 8.1.4 suggest that PW laser, if not being adjusted correctly, may reduce the stability of melt pool as compared to CW laser. A frequent on and off of local heating during laser scanning modifies the direction of recoil pressure and the pattern of spattering.

8.1.5 Effects of Pulse Laser Repetition Rate on the Spattering

The study of PW laser repetition rate in Fig. 8-5 was conducted under a constant linear energy input to the melt pool. Clearly, the constant energy input or the same “laser on” time during the process did not guarantee the similar scattering behavior. From RR1 to RR3, an increased repetition rate with the decreased pulse width worsened the melt spattering, confirming that higher frequency of pulse can reduce the stability of melt pool. However, at RR4, the spattering was suppressed by a noticeable amount. The fundamental reason will be discussed later through melt pool simulation.

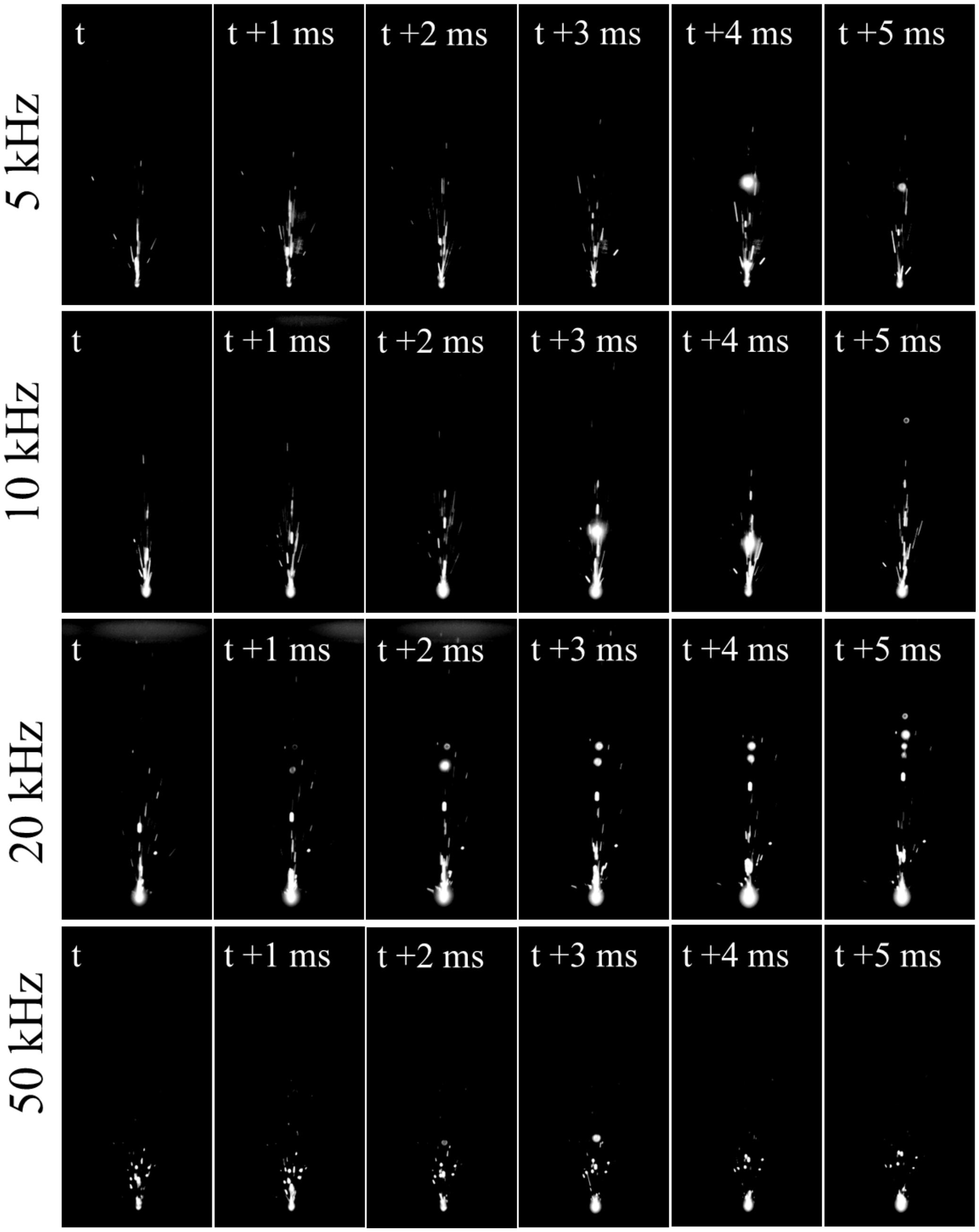

Fig. 8-5 High-speed camera images capture the dynamic variations of a spattering of in-situ ODS steel with different repetition rates, 5, 10, 20, and 50 kHz.

8.1.6 Spattering speed of different PW Laser Parameters

Fig. 8-6 summarizes the spattering speed of the in-situ and ex-situ L-PBF ODS SS under different pulse laser parameters. The spatter speed was estimated from the travel distance during the exposure time of 700 us in each frame. Two imaging directions, parallel and perpendicular to the scan direction, reveal the spatter moving distance projection in X and Y direction. Ten consecutive frames were used to analyze the spatter speed, which covered the laser track of 1 mm. We note that this method shows the projected speed in the X and Y direction, not the actual spatter speed in 3D. However, the projection in two directions still provide a reasonable comparison of spattering speed. In all conditions, spatters in the in-situ samples have a lower ejection speed than the ex-situ samples, suggesting that the in-situ reaction in the melt pool reduces the recoil pressure in the melt pool. Increased laser power and pulse width will drastically increase the speed of spatters as both of them contribute more energy to the melt pool. A longer pulse interval could reduce the spattering due to the decrease in the linear energy input. In comparison, the repetition rate study was conducted under the same linear energy input. This study highlights the ability of laser pulse shaping to modify spattering patterns and microstructure while the energy input is not reduced. In this case, a higher repetition rate reduced the spattering speed. We emphasize a reduced spattering without a loss of input energy is desired in pulse laser AM.

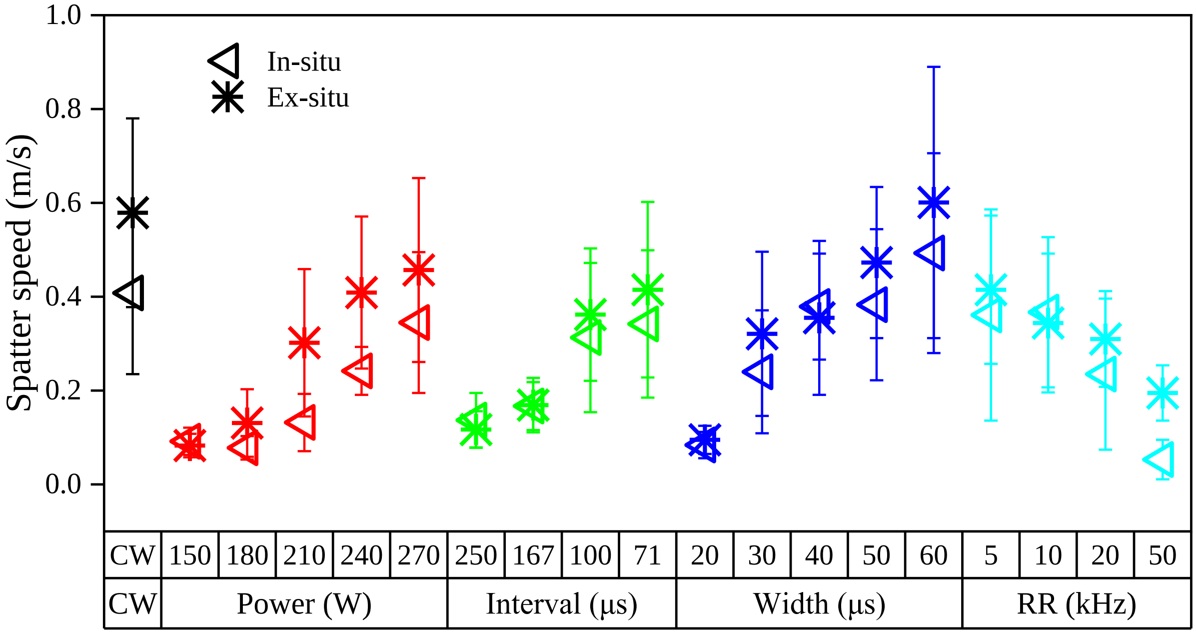

Fig. 8-6 Spatter speed of the in-situ and ex-situ ODS steels with different printing parameters.

8.1.7 Spattering Mechanism

In L-PBF AM, the localized laser melting creates melt pool instability, leading to the formation of several different types of defects and spatters. As the high-energy laser beam impinges on the powders, the localized laser heating causes surface boiling to develop a strong vapor jet. The recoil pressure created by the vapor jet pushes the melt surface downward to develop a vapor depression. It is also known as the depression zone or keyhole [148]. The high speed of the upward vapor flow ejects surrounding powders and liquid droplets away to form spatters. The recoil pressure is usually nonuniform due to the nonuniform energy absorption as the laser absorptivity strongly depends on the incident angle. The vapor depression fluctuation induced by the liquid breakup and spatter colliding can cause the formation of larger spatters [149], which can create major defects and oxygen loss during manufacturing.

The recoil pressure exponentially depends on temperature, which can be expressed as [150]:

$$P(T) = 0.54P_a \exp\left(\frac{\lambda}{K_B}\left(\frac{1}{T} - \frac{1}{T_B}\right)\right)$$

Where $P_a = 1\ bar$, is the ambient pressure, $\lambda = 4.3\ ev/atom$ is the evaporation energy per particle, $K_B = 8.617 \times 10^{-5} ev/K$ is the Boltzmann constant, T is the surface temperature and T_B is the boiling temperature of a given material, for 316L SS, $T_B = 3086\ K$. The spatter's early trajectory is determined by the large expulsion force, which can generate acceleration of $\sim 1 \times 10^5 m/s^2$. The trajectory may be altered later in time in the presence of gas entrainment or getting caught by the vapor plume.

The strong temperature gradient below the laser enables temperature-dependent surface tension $(T) = 3.282 - 8.9e^{-4}T$, where T is the temperature in Kelvin. This creates Marangoni effects. The Marangoni convection drive melts flow from the hot laser spot toward the cold rear and creates spattering as liquid metal with low viscosity ejects away from the surface [99]. The general spattering behavior during the L-PBF process can be affected by the combination of the Marangoni convection and recoil pressure. These two major factors are all temperature-dependent. Thus, it's necessary to understand the temperature distribution in the melt pool with different printing parameters. The finite volume method (FVM) was used to estimate the melt pool temperature using commercial software, FLOW-3D (FLOW SCIENCE Inc., USA). The temperature fields on the XZ plane parallel with the scan direction printed with CW laser and PW laser with repetition rates of 5 kHz and 10 kHz are shown in Fig. 8-7. Note CW laser here used the same laser power as the PW laser trails, thus leading to higher linear energy input. The simulation visualized a larger melting zone and higher peak temperature by CW laser melting. The temperature difference can significantly affect the recoil pressure and Marangoni convection, leading to different spattering behavior.

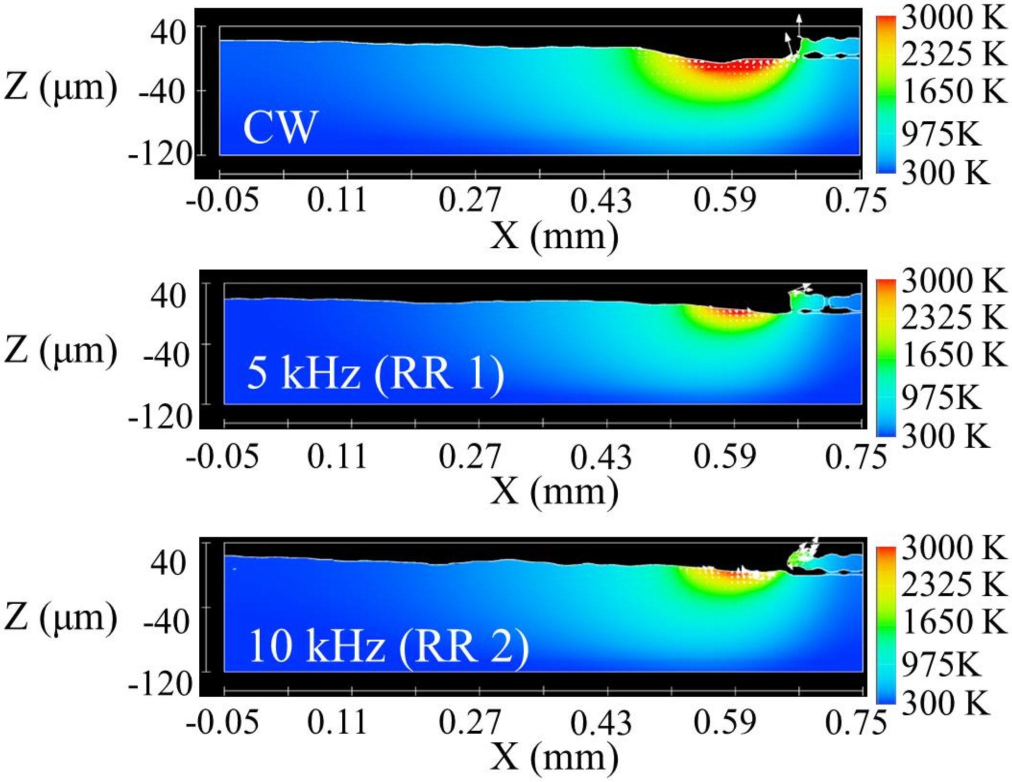

Fig. 8-7 Temperature fields of the melt pools with different printing parameters.

8.1.8 Oxide Volume Fraction

Oxide volume fraction analyzed from SEM images of different pulse laser parameters is shown in Fig. 8-8. The in-situ samples have a remarkably higher oxide volume fraction than the ex-situ samples when being manufactured under the same processing condition. This can be attributed to the melting temperature difference between Y_2O_3 and Fe_2O_3 and the more uniform nucleation of nano oxides by in-situ reaction. Since Y_2O_3 is hard to melt, the chance of ejecting unmelted Y_2O_3 agglomerates by spattering is also higher in the ex-situ sample.

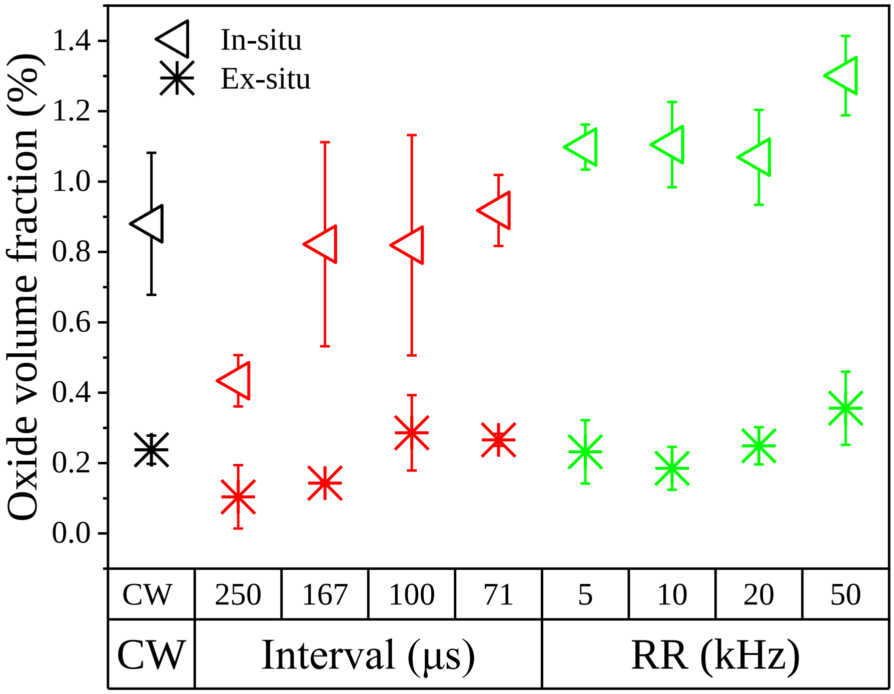

Fig. 8-8 Oxide volume fractions of samples with different pulse laser parameters.

Compared to CW laser AM, PW laser AM showed an increased fraction of nano oxides present in the material. At the repetition rate of 50 kHz, ~40% increase in the amount of oxides was achieved by PW laser as compared to CW laser. This remarkable increase in the oxide production was translated to the higher indentation hardness shown in Fig. 7-5. In the repetition rate study, the linear energy input was kept the same with a variation in PW laser settings. It is interesting to note that no significant change was observed when the repetition rate was between 5-20 kHz. As the repetition rate reached 50 kHz, an increase in oxide was observed. This result highlights the importance of a short pulse in managing the oxide nucleation and loss. We have reason to believe that a nanosecond or femtosecond laser has the potential to increase oxide dispersion by orders of magnitude. It should be emphasized that the total oxide amount in samples made by different PW laser settings varied, which trended well with the nanohardness data and the spattering behavior that were reported before. The results confirmed the melt pool spattering contributes to the oxygen loss during reactive AM of ODS SS.

8.2 Mechanistic Insights on Oxide Formation Under Pulse Laser Melting

Regardless a large amount of work being performed towards laser AM of ODS alloys [66,70,100,151–153], the oxide density is AM ODS alloys are generally lower than that of PM counterparts by 2-3 orders of magnitude. Pulse laser shows an advantage in refining oxide size and increasing oxide density. In this section, we use thermodynamic calculation and melt pool dynamic simulation to understand the oxide formation process and reveal the controlling factors.

8.2.1 Oxide formation in 316L SS with Different Oxygen Contents

In a multi-element alloy system, the formation of oxide inclusions highly depends on the alloy composition and oxygen level in the system. Research has shown different types of oxides can form as the availability of oxygen changes. Here, we assume the pre-mixed oxides can be fully dissociated under laser melting in both in-situ and ex-situ AM ODS SS. This assumption is backed by the fact that the nanoscale Y_2O_3 present in AM ODS SS is typically much smaller than the precursor oxides added to the starting powder, both shown in this work and other literature [100]. The oxide dissociation released oxygen and uniformly distributed it to react with more reactive oxygen getters. Assuming oxygen and other alloying elements are uniformly distributed, we use CALPHAD to predict the oxide formation in the melt and the solid phase during laser solidification.

Pandat™ software with the PanFe database was used to perform this calculation. To conduct this calculation, the oxide description in the liquid phase was revised by Pandat. The calculation is based on 17.7 wt% Cr, 13.93 wt% Ni, 2.29 wt% Mo, 0.002 wt% C, 0.02 wt% Mn, 0.74 wt% Si, and 1.57 wt% Y, and balance Fe, but different oxygen contents 0.43 wt% and 1 wt% O. As shown in Fig. 8-9, slag (Y-Si-O) and Y_2O_3 co-exist above the liquidus temperature, suggesting that the nucleation of oxide can occur at a very fast rate and very high temperature in the liquid metal. The oxide slag can precipitate from the liquid at 2847 K, a much higher temperature than Y_2O_3 nucleation temperature (2083 K). The early formation of slag and Y_2O_3 in the liquid is harmful to the quality of AM ODS SS in two ways, First, the low-density slag and oxides tend to float on the melt pool surface and can be ejected by the recoil pressure. This process decreases the oxygen level in the metal. Second, the element diffusion in the liquid is faster. The diffusivity of oxygen in liquid iron was estimated to be $2.5{\sim}5.5 \times 10^{-5} cm^2/s$ at 1560 °C [154], which is several orders faster than that in solid steel. Thus, the oxide growth is substantial in the liquid, leading to larger oxide size and lower oxide density in the final part. In addition, due to the excess oxygen in the feedstock powders, other oxides like Cr_2O_3 and spinel ($CrMn_2O_4$) can also form during the process. The thermal stability of these oxides is inferior to the Y_2O_3 and may deteriorate the mechanical properties.

When reducing the oxygen level to 0.43 wt%, the slag formation temperature dropped to a much lower temperature of 1920 K, and the content decreased dramatically. However, the Y_2O_3 formation temperature increased to around 2600 K. This may increase the oxygen loss and facilitate the oxide growth. In summary, to achieve high-quality AM ODS SS, a more careful design and control of oxygen level in the starting powder should be the focus of the study to minimize the overall oxide nucleation temperatures.

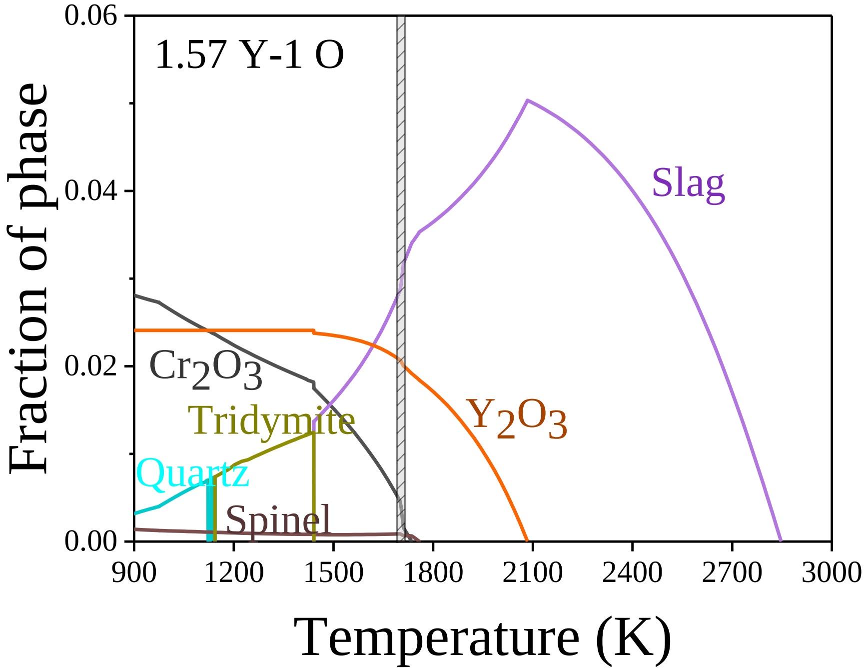

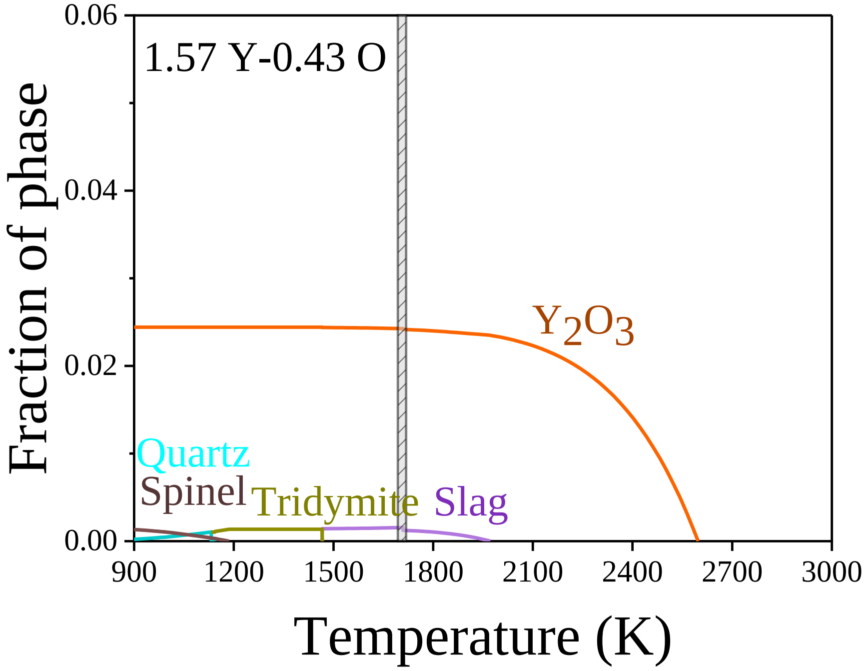

Fig. 8-9 Variation of oxide content in the in-situ ODS steel with different oxygen content.

8.2.2 Representative Temperature Profile of Melt Pool

The temperature profile in the middle of the XY plane (middle of the melt pool) at different Z heights of CW and PW samples of 5, 10 kHz are shown in Fig. 8-10. The peak temperature close to the melt pool surface (Z= +2.5 μm) is higher than that in the melt pool interior (Z= -16.67 μm). The temperature profile of the CW sample is discontinuous at the surface (Z= +2.5 μm) because liquid metal is predicted to be absent on the surface due to the high pressure from the intense laser-liquid interaction. The peak temperature of the CW sample is higher than that of the PW ones. The PW laser causes the oscillation of temperature above the liquidus line, which may result in frequent solid-liquid transitions beneath the liquid surface. No clear difference between 5 kHz and 10 kHz PW laser was observed at both locations, which might be due to the same linear energy input in this study.

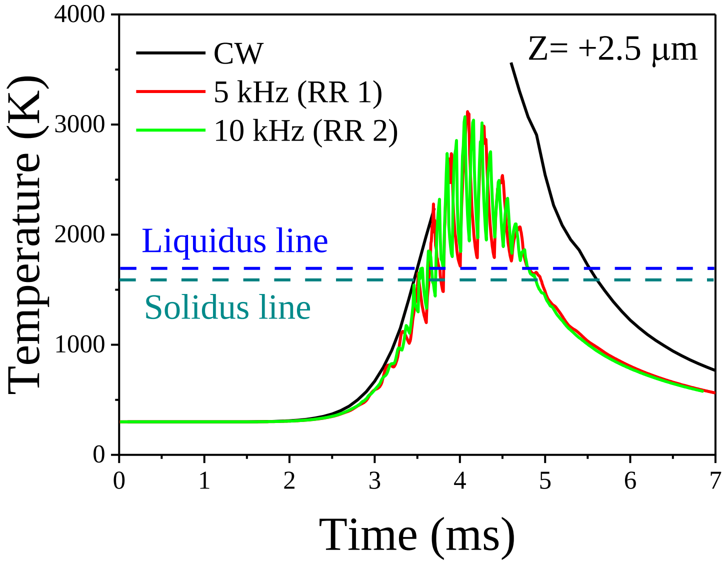

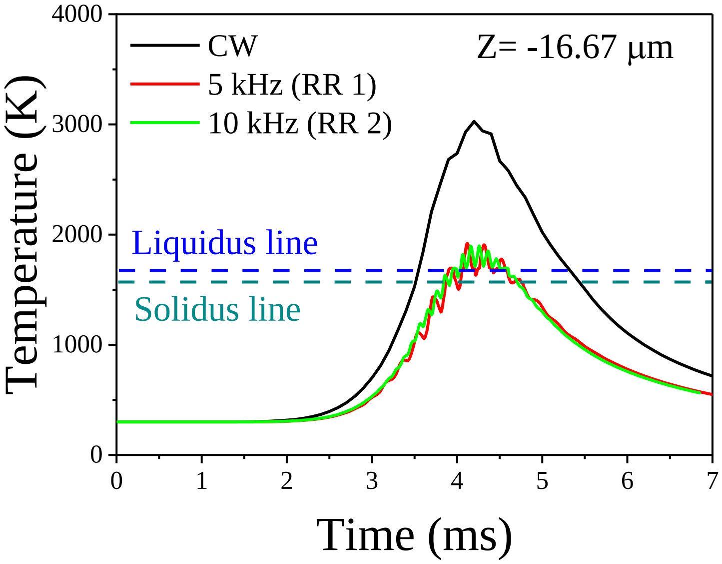

Fig. 8-10 The temperature profile at different Z heights with different parameters.

The mean cooling rate was estimated from the temperature profile. One is from the last cooling cycle between the peak oxide formation temperature ~2100 K and the solidus line ~1568 K to discuss the oxide nucleation rate. Another is between the liquiduis line of ~l678 K and the solidus line ~1568 K to estimate the solidification structure. Generally, the cooling rate estimated from these two ranges show very simialr value. The duration of the melt pool in the liquid phase (above the solidus line) was also summarized in Table 8-1. The liquid phase duration in the CW laser sample is about 2~4 times longer than that in the PW laser ones, depending on location in the melt pool. 2-3 times higher cooling rate can be achieved by using a PW laser under 5 kHz compared to the CW sample. A shorter liquid phase duration can suppress the rapid oxide growth and reduce melt pool spattering. A faster cooling rate is also desired to refine dislocation cellular structure. However, we emphasize the particle morphology differences in Fig. 7-7 of CW, 5 kHz, and 10 kHz samples did not correlate well with the liquid phase duration shown here among these materials. Thus, liquid phase duration may not have primary responsibility for oxide growth under these conditions. The average temperature of the liquid phase and liquid phase duration both need to be considered. The faster cooling rate also supports the refined cellular structure shown in Fig. 6-15.

Table 8-1 Cooling rates and duration of melt pool in the liquid phase of CW sample and PW samples with different repetition rates.

	Sample	Cooling rate (x10^6 K/s)		Liquidus time (ms)
		Liquidus-solidus line	Last cooling cycle between oxide formation temperature to solidus line	
Z= 2.5 μm	CW	1.21	1.20	2.1
	5 kHz (RR 1)	3.63	3.58	1.17
	10 kHz (RR 1)	1.62	1.93	1.19
Z= -16.67 μm	CW	0.96	1.04	1.78
	5 kHz (RR 1)	2.03	2.06	0.53
	10 kHz (RR 1)	1.32	1.07	0.61

Fig. 8-11 shows the effects of pulse interval on the temperature profile at different heights. The peak temperature of the sample with 71 μs pulse interval can reach 3500 K, while the 250 μs sample has a remarkably lower temperature, slightly higher than the liquidus line at the Z height of 2.5 μm. Near the bottom of the melt pool with a Z height of –16.67 μm, the temperature of the 250 μs sample was lower than the solidus line, which suggests that the energy input is insufficient to fabricate full dense parts. This was also confirmed by the density analysis in Chapter 6 and 7.

A longer pulse interval of 250 μs dramatically reduces the liquid phase duration to 0.16 ms at a Z height of 2.5 μm, and the mean cooling rate reaches 16.6×10^{6} K/s, which is ~8 times faster than a longer pulse interval of 71 µs (Table 8-2). These features of the melt pool finally yield an average oxide size of ~32 nm in the ex-situ ODS steel, 50% smaller than that in the 71 µs sample.

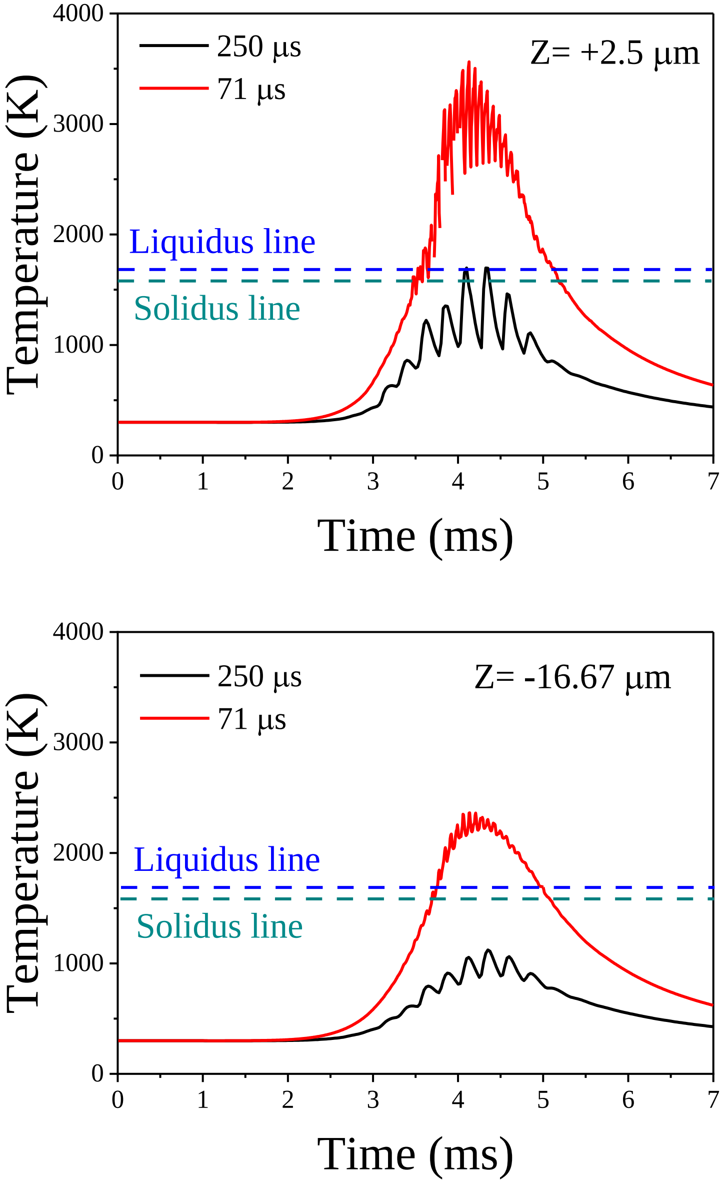

Fig. 8-11 The temperature profile at different Z heights with different pulse intervals.

Table 8-2 Cooling rates and duration of melt pool in the liquid phase of PW samples with different pulse intervals.

	Sample	Cooling rate (x10^6 K/s)		Liquidus time (ms)
		Liquidus-solidus line	Last cooling cycle between oxide formation temperature to solidus line	
Z= +2.5 μm	250 μs (Interval 1)	16.64	5.6	0.16
	71 μs (Interval 2)	2.36	1.35	1.54
Z= -16.67 μm	250 μs (Interval 1)	-	-	-
	71 μs (Interval 2)	1.33	1.06	1.36

In summary, a faster cooling rate and shorter duration time of melt pool in the liquid phase can be achieved by using PW lasers. High pulse frequency also increases the average temperature during the liquid phase duration. Different PW laser parameters can also affect the temperature fields of the melt pool and hence the oxide distribution in the ODS steel. We emphasize the melt pool simulation in this section was based on the physical properties of 316L SS, and the results can be slightly different if the basic physical properties of in-situ or ex-situ ODS feedstock powders can be obtained.

8.3 Strengthening Mechanism of L-PBF ODS steels

One of the main strengthening mechanisms is Orowan strengthening σ_{OR}, given by Ref. [155]:

$$\sigma_{Orowan} = \frac{0.4MGb}{\pi(1-\upsilon)^{0.5}L}\ln(\frac{\sqrt{\frac{2}{3}}d_p}{b})$$

Where $L = \sqrt{\frac{2}{3}} d_p (\sqrt{\frac{\pi}{4 \upsilon_p} - 1})$, and M is the Taylor factor for 316L (3.06), υ is Poisson's ratio (0.26), G is the shear modulus (78 GPa), L is the interparticle spacing, b is the Burgers vector (0.254 nm), d_p denotes the average particle diameter, and υ_p represents the volume fraction of the particles. It demonstrates that higher volume fraction and smaller interparticle spacing of reinforcement in a composite material will significantly increase the strength. In the in-situ L-PBF ODS SS, an oxide volume fraction of 0.01 and an average oxide size of 45 nm were used to estimate the strength caused by Orowan strengthening. The calculated value is ~137 MPa, which is significantly lower than the Orowan strengthening contribution in conventional PM ODS steel. If we assume the oxides in AM ODS SS are all in the form of Y_2O_3, the estimated oxygen concentration in AM ODS steel is ~1200 ppm. This value is comparable to the oxygen level in commercial PM 2000 (1080 ppm) and MA 950 (910 ppm) ODS alloys [120]. Reducing the oxide size should be considered to increase the strengthening effect by oxide precipitates in L-PBF ODS steels. If we assume the reduction of oxide size to 20, 10, and 5 nm can be achieved during the L-PBF process, it will contribute to the strength of 260, 433, and 694 MPa, respectively.

The grain size also significantly affects the strength of metal because grain boundaries hinder the dislocation motion. The grain boundary strengthening is described by the Hall-Petch relation, $\sigma_{H-P} = \sigma_0 + k_y {d_m}^{-1/2}$where σ_0 is the friction stress in the absence of grain boundaries, k_y represents the strength coefficient, and d_m is the grain size of the matrix. In AM 316L SS, Wang [113] found that not the grain size but the cellular size fit well with the Hall-Petch relation.

To improve the mechanical properties of L-PBF ODS steel, the following approaches can be considered: 1) Reduce the duration time of the melt pool in the liquid phase by changing appropriate PW laser parameters; 2) Increase the oxygen content of the melt pool by minimizing the spattering behavior; 3) Increase the cooling rate by choosing shorter pulse laser, e.g., nanosecond, femtosecond or even picosecond pulse laser.

8.4 Conclusion

The mechanistic insights on enabling L-PBF ODS were discussed by experimental and modeling work. The spattering behavior of L-PBF ODS steel was evaluated and correlated to the oxide volume fraction in the matrix. The temperature field of the melt pool modeled by Flow 3D provide insight into how it affects the oxide evolution during the L-PBF process with different parameters.

Oxide formation with different oxygen content in the melt pool was also simulated. The main conclusions are summarized below:

1) PW laser can reduce the spattering during the L-PBF process, and hence higher oxide volume fraction in the matrix was obtained.
2) Temperature fields of the melt pool with different printing parameters suggest a shorter duration of the melt pool in the liquid phase, and an enhanced cooling rate can be achieved during the L-PBF process by using PW lasers, which contribute to the refined oxides with a higher density in the PW ODS steel.
3) High oxygen content in the melt pool will lead to the formation of slag during laser melting, and the slag can be spattered hence causing the oxygen loss. Appropriate oxygen content is essential for AM ODS steel.
4) Comparable oxygen content to that in PM ODS steel can be induced during the L-PBF process. Oxide refinement is the main challenge for AM process to fabricate ODS steels.

CHAPTER 9

GLOBAL VIEW OF THE L-PBF ODS STEELS AND RECOMMENDATIONS

9.1 Summary

The aim of this work is to develop methods and mechanistic understandings of fabricating ODS steel by AM process. Different oxygen sources, e.g., gas- and solid-phase oxygen donors, were utilized to form nano oxides in the steel during laser solidification. The strengthening mechanism of AM ODS steels with excellent thermal stability was discussed. Oxide distribution optimization and part quality improvement were explored by using PW lasers. Melt pool modeling provides insights on enabling fine oxide dispersion strengthening steel by AM. The main conclusions are summarized below. The efficiency of in-situ oxidation by reacting with gas-phase oxygen donor (oxygen in the shielding gas) was affected by the oxygen affinity of getter elements, oxygen level in the shielding gas, and getter concentration as well as printing parameters. Oxygen intrusion through melt pool oxidation was restricted by the thick oxide layer formed on the melt pool surface under high oxygen levels with more reactive elements. No AM ODS steels by using gas-phase oxygen donor showed comparable oxide density to that in PM ODS steels. Reactive AM methods by reacting Y-contained SS powders with solid-phase oxygen donor of low melting point Fe_2O_3 oxide show an advantage in improving oxide density of the in-situ reacted ODS steel. Excellent thermal stability of the in-situ AM ODS steel stems from the stabilizing of unique cellular structure. Enormous oxides with sub-micron interparticle spacing pined the dislocations during heat treatment and a stable subgrain structure formed. Compared to the L-PBF process using CW laser, PW laser shows great potential in fabricating ODS steel by L-PBF due to the advantages of reducing spattering and shortening the duration time of melt pool in the liquid phase, and enhancing cooling rate.

9.2 Challenge for L-PBF ODS steels

Laser powder bed fusion is a rapid fabrication process with a fast-cooling rate, but the duration time of the melt pool in the liquid phase can still be in the range of milliseconds by using the commercial 3D printers equipped with CW laser and PW laser with microseconds duration. The liquid duration time significantly affects the oxide growths, and hence no AM ODS steels show comparable fine oxide and density as the conventional ODS alloy fabricated using PM methods. Oxygen loss during the L-PBF process is reported and needs to be addressed in the future. Due to the lower density and higher surface energy of nano oxides, they tend to float to the melt pool surface and form agglomerations during the L-PBF process. The intense laser beam could cause selective evaporation, spatter ejecting, or a combination of these factors and lead to oxygen loss. The residual oxide agglomerates will also deteriorate the part quality due to the poor interface between the oxide clusters and liquid metal. These challenges will limit the application of AM ODS steel before they are addressed.

9.3 Recommendations

Although both phenomenological and mechanistic understandings of the L-PBF ODS steel has been obtained based on this research, more work needs to be done to further optimize the oxide density and part quality. The mechanical properties of L-PBF ODS steels also need to be evaluated to satisfy the field application requirements. Some suggestions related to the strengthening mechanism of AM ODS steel, oxide refinement by modifying the oxide compositions, and printing using different lasers and processing parameters are provided in the following:

I. Strengthening mechanism

   1) Time-resolved study by in-situ heating in the electron microscope or short-duration ex-situ heating could be utilized to track the oxides evolution and oxides-cellular boundary interactions during the heat treatment. This could help better understand the advanced thermal stability of AM ODS steels.
   2) Extensive work needs to be performed to evaluate the mechanical properties of AM ODS steel at room and elevated temperatures to understand the deformation mechanism of AM ODS steel. The interactions between dislocation, amorphous oxides, cellular boundaries in as-built AM ODS steel, and dislocation, crystalline oxides, and low-angle boundaries in the heat-treated sample are still unclear.

II. Modify the oxide composition

   1) Ti, Zr, and Hf may improve the dispersion of Y_2O_3 by forming complex $Y_2Ti_2O_7$, $Y_4Zr_3O_{12}$, and $Y_2Hf_2O_7$ oxides. The effects of these elements on the refinement of Y_2O_3 during AM process need to be explored.
   2) The buoyance of the Y_2O_3 is inevitable due to its lower density than the liquid metal and hence results in oxygen loss by spattering. Higher density oxides like CeO_2, Er_2O_3, and Gd_2O_3 can be used as alternative reinforcements for AM ODS steels.
   3) Decreasing the interfacial energy between the oxide nuclei and molten steel by modify the oxide composition can reduce the oxide size and increase the number density.

4) Though the oxide evolution during the L-PBF process was discussed, the analysis of oxide nucleation and growth behavior during the L-PBF process is still needed.

III. Manufacturing science

1) Ultrashort pulse laser such as ns, ps, and fs could significantly refine the precipitate size and was reported recently [82,91], and it could also help refine the oxide size and improve the density in AM ODS steels.
2) Due to the complexity of the pulse laser parameters, for example, scan speed, hatch spacing, laser power, duty cycle, pulse duration/width, pulse repetition rate, etc., it is challenging to understand which has a significant effect on the microstructures and mechanical properties. Machine learning/data science can be utilized to clarify the contribution of each parameter and guide the parameter selection.
3) The laser intensity shape modulation was recently reported beneficial for microstructural control [88,156], but their effects on the AM parts, especially for AM ODS steels, haven't been studied.

REFERENCE

[1] G.R. Odette, M.J. Alinger, B.D. Wirth, Recent Developments in Irradiation-Resistant Steels, (2008). https://doi.org/10.1146/annurev.matsci.38.060407.130315.

[2] S.J. Zinkle, Fusion materials science: Overview of challenges and recent progressa), Phys. Plasmas. 12 (2005) 058101. https://doi.org/10.1063/1.1880013.

[3] S.J. Zinkle, N.M. Ghoniem, Operating temperature windows for fusion reactor structural materials, Fusion Eng. Des. 51–52 (2000) 55–71. https://doi.org/10.1016/S0920-3796(00)00320-3.

[4] K. Ehrlich, The development of structural materials for fusion reactors, Philos. Trans. R. Soc. London. Ser. A Math. Phys. Eng. Sci. 357 (1999) 595–623. https://doi.org/10.1098/RSTA.1999.0343.

[5] J.B. Roberto, T.D. de la Rubia, Basic research needs for advanced nuclear energy systems, JOM 2007 594. 59 (2007) 16–19. https://doi.org/10.1007/S11837-007-0048-X.

[6] S. Ukai, S. Ohtsuka, T. Kaito, Y. de Carlan, J. Ribis, J. Malaplate, Oxide dispersion-strengthened/ferrite-martensite steels as core materials for Generation IV nuclear reactors, Struct. Mater. Gener. IV Nucl. React. (2017) 357–414. https://doi.org/10.1016/B978-0-08-100906-2.00010-0.

[7] H. Tanigawa, E. Gaganidze, T. Hirose, M. Ando, S.J. Zinkle, R. Lindau, E. Diegele, Development of benchmark reduced activation ferritic/martensitic steels for fusion energy applications, Nucl. Fusion. 57 (2017) 092004. https://doi.org/10.1088/1741-4326/57/9/092004.

[8] A. Hirata, T. Fujita, Y.R. Wen, J.H. Schneibel, C.T. Liu, M.W. Chen, Atomic structure of

nanoclusters in oxide-dispersion-strengthened steels, Nat. Mater. 10 (2011) 922–926. https://doi.org/10.1038/nmat3150.

[9] G.R. Odette, M.J. Alinger, B.D. Wirth, Recent Developments in Irradiation-Resistant Steels, (2008). https://doi.org/10.1146/annurev.matsci.38.060407.130315.

[10] E.A. Kenik, D. Hoelzer, P.J. Maziasz, M.K. Miller, Characterization of Nanoscale Clusters in Ods Iron-Based Alloys, Microsc. Microanal. 7 (2001) 550–551. https://doi.org/10.1017/S1431927600028828.

[11] D.J. Larson, P.J. Maziasz, I.S. Kim, K. Miyahara, Three-dimensional atom probe observation of nanoscale titanium-oxygen clustering in an oxide-dispersion-strengthened Fe-12Cr-3W-0.4Ti+Y2O3 ferritic alloy, Scr. Mater. 44 (2001) 359–364. https://doi.org/10.1016/S1359-6462(00)00593-5.

[12] M.K. Miller, E.A. Kenik, K.F. Russell, L. Heatherly, D.T. Hoelzer, P.J. Maziasz, Atom probe tomography of nanoscale particles in ODS ferritic alloys, Mater. Sci. Eng. A. 353 (2003) 140–145. https://doi.org/10.1016/S0921-5093(02)00680-9.

[13] S. Ukai, M. Fujiwara, Perspective of ODS alloys application in nuclear environments, J. Nucl. Mater. 307–311 (2002) 749–757. https://doi.org/10.1016/S0022-3115(02)01043-7.

[14] T.K. Kim, S. Noh, S.H. Kang, J.J. Park, H.J. Jin, M.K. Lee, J. Jang, C.K. Rhee, Current Status and Future Prospective of Advanced Radiation Resistant Oxide Dispersion Strengthened Steel (ARROS) Development for Nuclear Reactor System Applications, Nucl. Eng. Technol. 48 (2016) 572–594. https://doi.org/10.1016/J.NET.2015.12.005.

[15] F. Masoumi, D. Shahriari, M. Jahazi, J. Cormier, A. Devaux, Kinetics and Mechanisms of γ′ Reprecipitation in a Ni-based Superalloy, Sci. Reports 2016 61. 6 (2016) 1–16.

https://doi.org/10.1038/srep28650.

[16] S.J. Zinkle, J.T. Busby, Structural materials for fission & fusion energy, Mater. Today. 12 (2009) 12–19. https://doi.org/10.1016/S1369-7021(09)70294-9.

[17] V. Chawla, S. Prakash, B.S. Sidhu, State of the Art: Applications of Mechanically Alloyed Nanomaterials—A Review, Http://Dx.Doi.Org/10.1080/10426910701235900. 22 (2007) 469–473. https://doi.org/10.1080/10426910701235900.

[18] J.P. Wharry, M.J. Swenson, K.H. Yano, A review of the irradiation evolution of dispersed oxide nanoparticles in the b.c.c. Fe-Cr system: Current understanding and future directions, J. Nucl. Mater. 486 (2017) 11–20. https://doi.org/10.1016/J.JNUCMAT.2017.01.009.

[19] M.S. El-Genk, J.M. Tournier, A review of refractory metal alloys and mechanically alloyed-oxide dispersion strengthened steels for space nuclear power systems, J. Nucl. Mater. 340 (2005) 93–112. https://doi.org/10.1016/J.JNUCMAT.2004.10.118.

[20] 왕만. Dispersoid Precipitation and Creep Behavior of Nickel-Based Oxide Dispersion Strengthened Alloys. Diss. 서울대학교 대학원, 2018.

[21] R. Gao, L.L. Xia, T. Zhang, X.P. Wang, Q.F. Fang, C.S. Liu, Oxidation resistance in LBE and air and tensile properties of ODS ferritic steels containing Al/Zr elements, J. Nucl. Mater. 455 (2014) 407–411. https://doi.org/10.1016/J.JNUCMAT.2014.07.028.

[22] A. Deschamps, F. De Geuser, J. Malaplate, D. Sornin, When do oxide precipitates form during consolidation of oxide dispersion strengthened steels?, J. Nucl. Mater. 482 (2016) 83–87. https://doi.org/10.1016/j.jnucmat.2016.10.017.

[23] T. Okuda, M. Fujiwara, Dispersion behaviour of oxide particles in mechanically alloyed

ODS steel, J. Mater. Sci. Lett. 1995 1422. 14 (1995) 1600–1603. https://doi.org/10.1007/BF00455428.

[24] M. Klimiankou, R. Lindau, A. Möslang, Energy-filtered TEM imaging and EELS study of ODS particles and Argon-filled cavities in ferritic–martensitic steels, Micron. 36 (2005) 1–8. https://doi.org/10.1016/J.MICRON.2004.08.001.

[25] H. Kishimoto, M.J. Alinger, G.R. Odette, T. Yamamoto, TEM examination of microstructural evolution during processing of 14CrYWTi nanostructured ferritic alloys, J. Nucl. Mater. 329–333 (2004) 369–371. https://doi.org/10.1016/J.JNUCMAT.2004.04.044.

[26] J.H. Schneibel, C.T. Liu, M.K. Miller, M.J. Mills, P. Sarosi, M. Heilmaier, D. Sturm, Ultrafine-grained nanocluster-strengthened alloys with unusually high creep strength, Scr. Mater. 61 (2009) 793–796. https://doi.org/10.1016/J.SCRIPTAMAT.2009.06.034.

[27] M.K. Miller, K.F. Russell, D.T. Hoelzer, Characterization of precipitates in MA/ODS ferritic alloys, J. Nucl. Mater. 351 (2006) 261–268. https://doi.org/10.1016/J.JNUCMAT.2006.02.004.

[28] G.R. Odette, M.J. Alinger, B.D. Wirth, Recent Developments in Irradiation-Resistant Steels, Http://Dx.Doi.Org/10.1146/Annurev.Matsci.38.060407.130315. 38 (2008) 471–503. https://doi.org/10.1146/ANNUREV.MATSCI.38.060407.130315.

[29] S. Yamashita, N. Akasaka, S. Ukai, S. Ohnuki, Microstructural development of a heavily neutron-irradiated ODS ferritic steel (MA957) at elevated temperature, J. Nucl. Mater. 367–370 (2007) 202–207. https://doi.org/10.1016/J.JNUCMAT.2007.03.145.

[30] M.J. Alinger, G.R. Odette, D.T. Hoelzer, On the role of alloy composition and processing

parameters in nanocluster formation and dispersion strengthening in nanostuctured ferritic alloys, Acta Mater. 57 (2009) 392–406. https://doi.org/10.1016/J.ACTAMAT.2008.09.025.

[31] H. Sakasegawa, L. Chaffron, F. Legendre, L. Boulanger, T. Cozzika, M. Brocq, Y. de Carlan, Correlation between chemical composition and size of very small oxide particles in the MA957 ODS ferritic alloy, J. Nucl. Mater. 384 (2009) 115–118. https://doi.org/10.1016/J.JNUCMAT.2008.11.001.

[32] P. Dou, A. Kimura, R. Kasada, T. Okuda, M. Inoue, S. Ukai, S. Ohnuki, T. Fujisawa, F. Abe, TEM and HRTEM study of oxide particles in an Al-alloyed high-Cr oxide dispersion strengthened steel with Zr addition, J. Nucl. Mater. 444 (2014) 441–453. https://doi.org/10.1016/J.JNUCMAT.2013.10.028.

[33] M. Gong, Z. Zhou, H. Hu, G. Zhang, S. Li, M. Wang, Effects of aluminum on microstructure and mechanical behavior of 14Cr–ODS steels, J. Nucl. Mater. 462 (2015) 502–507. https://doi.org/10.1016/J.JNUCMAT.2014.12.079.

[34] G. Zhang, Z. Zhou, K. Mo, Y. Miao, S. Li, X. Liu, M. Wang, J.S. Park, J. Almer, J.F. Stubbins, The comparison of microstructures and mechanical properties between 14Cr-Al and 14Cr-Ti ferritic ODS alloys, Mater. Des. 98 (2016) 61–67. https://doi.org/10.1016/J.MATDES.2016.02.117.

[35] R. Rahmanifard, H. Farhangi, A.J. Novinrooz, Effect of zirconium and tantalum on the microstructural characteristics of 12YWT ODS steel nanocomposite, J. Alloys Compd. 622 (2015) 948–952. https://doi.org/10.1016/J.JALLCOM.2014.11.018.

[36] H. Xu, Z. Lu, D. Wang, C. Liu, Effect of zirconium addition on the microstructure and

mechanical properties of 15Cr-ODS ferritic Steels consolidated by hot isostatic pressing, Fusion Eng. Des. 114 (2017) 33–39. https://doi.org/10.1016/J.FUSENGDES.2016.11.011.

[37] J. Ren, L. Yu, Y. Liu, C. Liu, H. Li, J. Wu, Effects of Zr Addition on Strengthening Mechanisms of Al-Alloyed High-Cr ODS Steels, Materials (Basel). 11 (2018) 118. https://doi.org/10.3390/ma11010118.

[38] J. Wang, S. Liu, B. Xu, J. Zhang, M. Sun, D. Li, Research progress on preparation technology of oxide dispersion strengthened steel for nuclear energy, Int. J. Extrem. Manuf. 3 (2021) 032001. https://doi.org/10.1088/2631-7990/ABFF1A.

[39] G. Robert Odette, N.J. Cunningham, T. Stan, M. Ershadul Alam, Y. De Carlan, Nano-Oxide Dispersion-Strengthened Steels, Struct. Alloy. Nucl. Energy Appl. (2019) 529–583. https://doi.org/10.1016/B978-0-12-397046-6.00012-5.

[40] F. Bergner, I. Hilger, J. Virta, J. Lagerbom, G. Gerbeth, S. Connolly, Z. Hong, P.S. Grant, T. Weissgärber, Alternative Fabrication Routes toward Oxide-Dispersion-Strengthened Steels and Model Alloys, Metall. Mater. Trans. A Phys. Metall. Mater. Sci. 47 (2016) 5313–5324. https://doi.org/10.1007/S11661-016-3616-2/FIGURES/6.

[41] J. Wang, W. Yuan, R.S. Mishra, I. Charit, Microstructural evolution and mechanical properties of friction stir welded ODS alloy MA754, J. Nucl. Mater. 442 (2013) 1–6. https://doi.org/10.1016/J.JNUCMAT.2013.08.012.

[42] C.L. Chen, A. Richter, R. Kögler, M. Griepentrog, P. Reinstädt, Ion-irradiation effects on dissimilar friction stir welded joints between ODS alloy and ferritic stainless steel, J. Alloys Compd. 615 (2014) S448–S453. https://doi.org/10.1016/J.JALLCOM.2013.11.123.

[43] K. Verhiest, S. Mullens, I. De Graeve, N. De Wispelaere, S. Claessens, A. De Bremaecker, K. Verbeken, Advances in the development of corrosion and creep resistant nano-yttria dispersed ferritic/martensitic alloys using the rapid solidification processing technique, Ceram. Int. 40 (2014) 14319–14334. https://doi.org/10.1016/J.CERAMINT.2014.06.023.

[44] Z. Hong, X. Zhang, Q. Yan, Y. Chen, A new method for preparing 9Cr-ODS steel using elemental yttrium and Fe2O3 oxygen carrier, J. Alloys Compd. 770 (2019) 831–839. https://doi.org/10.1016/j.jallcom.2018.08.196.

[45] D. Herzog, V. Seyda, E. Wycisk, C. Emmelmann, Additive manufacturing of metals, Acta Mater. 117 (2016) 371–392. https://doi.org/10.1016/J.ACTAMAT.2016.07.019.

[46] W.E. Frazier, Metal additive manufacturing: A review, J. Mater. Eng. Perform. 23 (2014) 1917–1928. https://doi.org/10.1007/s11665-014-0958-z.

[47] T. DebRoy, H.L. Wei, J.S. Zuback, T. Mukherjee, J.W. Elmer, J.O. Milewski, A.M. Beese, A. Wilson-Heid, A. De, W. Zhang, Additive manufacturing of metallic components – Process, structure and properties, Prog. Mater. Sci. 92 (2018) 112–224. https://doi.org/10.1016/J.PMATSCI.2017.10.001.

[48] A. 52900:2015, Standard Terminology for Additive Manufacturing – General Principles – Terminology, ASTM Int. i (2015) 1–9. http://compass.astm.org/EDIT/html_annot.cgi?ISOASTM52900+15.

[49] EN ISO/ASTM 52900:2017 - Additive manufacturing - General principles - Terminology (ISO/ASTM. https://standards.iteh.ai/catalog/standards/cen/c5a8f80e-af79-4ae1-b3d8-82da6395b5bc/en-iso-astm-52900-2017 (accessed May 16, 2022).

[50] H. Fayazfar, M. Salarian, A. Rogalsky, D. Sarker, P. Russo, V. Paserin, E. Toyserkani, A critical review of powder-based additive manufacturing of ferrous alloys: Process parameters, microstructure and mechanical properties, Mater. Des. 144 (2018) 98–128. https://doi.org/10.1016/j.matdes.2018.02.018.

[51] L.E. Murr, E. Martinez, K.N. Amato, S.M. Gaytan, J. Hernandez, D.A. Ramirez, P.W. Shindo, F. Medina, R.B. Wicker, Fabrication of Metal and Alloy Components by Additive Manufacturing: Examples of 3D Materials Science, J. Mater. Res. Technol. 1 (2012) 42–54. https://doi.org/10.1016/S2238-7854(12)70009-1.

[52] H.J. Lee, S.P. Cho, S. in Na, S.S. Kim, Thin metal top electrode and interface engineering for efficient and air-stable semitransparent perovskite solar cells, J. Alloys Compd. 797 (2019) 65–73. https://doi.org/10.1016/J.JALLCOM.2019.05.051.

[53] S.R. Narasimharaju, W. Zeng, T.L. See, Z. Zhu, P. Scott, X. Jiang, S. Lou, A comprehensive review on laser powder bed fusion of steels: Processing, microstructure, defects and control methods, mechanical properties, current challenges and future trends, J. Manuf. Process. 75 (2022) 375–414. https://doi.org/10.1016/J.JMAPRO.2021.12.033.

[54] P. Deng, M. Karadge, R.B. Rebak, V.K. Gupta, B.C. Prorok, X. Lou, The origin and formation of oxygen inclusions in austenitic stainless steels manufactured by laser powder bed fusion, Addit. Manuf. 35 (2020) 101334. https://doi.org/10.1016/j.addma.2020.101334.

[55] F. Yan, W. Xiong, E. Faierson, G.B. Olson, Characterization of nano-scale oxides in austenitic stainless steel processed by powder bed fusion, Scr. Mater. 155 (2018) 104–108. https://doi.org/10.1016/J.SCRIPTAMAT.2018.06.011.

[56] K. Saeidi, X. Gao, Y. Zhong, Z.J. Shen, Hardened austenite steel with columnar sub-grain structure formed by laser melting, Mater. Sci. Eng. A. 625 (2015) 221–229. https://doi.org/10.1016/j.msea.2014.12.018.

[57] K. Saeidi, L. Kvetková, F. Lofaj, Z. Shen, Austenitic stainless steel strengthened by the in situ formation of oxide nanoinclusions, RSC Adv. 5 (2015) 20747–20750. https://doi.org/10.1039/c4ra16721j.

[58] Q. Chao, V. Cruz, S. Thomas, N. Birbilis, P. Collins, A. Taylor, P.D. Hodgson, D. Fabijanic, On the enhanced corrosion resistance of a selective laser melted austenitic stainless steel, Scr. Mater. 141 (2017) 94–98. https://doi.org/10.1016/j.scriptamat.2017.07.037.

[59] J.C. Walker, K.M. Berggreen, A.R. Jones, C.J. Sutcliffe, Fabrication of Fe-Cr-Al oxide dispersion strengthened pm2000 alloy using selective laser melting, Adv. Eng. Mater. 11 (2009) 541–546. https://doi.org/10.1002/adem.200800407.

[60] T. Boegelein, S.N. Dryepondt, A. Pandey, K. Dawson, G.J. Tatlock, Mechanical response and deformation mechanisms of ferritic oxide dispersion strengthened steel structures produced by selective laser melting, Acta Mater. 87 (2015) 201–215. https://doi.org/10.1016/j.actamat.2014.12.047.

[61] T. Boegelein, E. Louvis, K. Dawson, G.J. Tatlock, A.R. Jones, Characterisation of a complex thin walled structure fabricated by selective laser melting using a ferritic oxide dispersion strengthened steel, Mater. Charact. 112 (2016) 30–40. https://doi.org/10.1016/j.matchar.2015.11.021.

[62] M. Ghayoor, K. Lee, Y. He, C.-H. Chang, B.K. Paul, S. Pasebani, Microstructural

Analysis of Additively Manufactured 304L Stainless Steel Oxide Dispersion Strengthened Alloy, Microsc. Microanal. 25 (2019) 2019. https://doi.org/10.1017/S1431927619013709.

[63] M. Ghayoor, S. Mirzababaei, K. Lee, Y. He, C.-H. Chang, B.K. Paul, S. Pasebani, Strengthening of 304L Stainless Steel by Addition of Yttrium Oxide and Grain Refinement during Selective Laser Melting, n.d.

[64] W. Zhai, W. Zhou, S.M.L. Nai, J. Wei, Characterization of nanoparticle mixed 316 L powder for additive manufacturing, J. Mater. Sci. Technol. 47 (2020) 162–168. https://doi.org/10.1016/j.jmst.2020.02.019.

[65] B.M. Arkhurst, J.-J. Park, C.-H. Lee, J.H. Kim, Direct Laser Deposition of 14Cr Oxide Dispersion Strengthened Steel Powders Using Y 2 O 3 and HfO 2 Dispersoids, 대한금속·재료학회지 (Korean J. Met. Mater.). 55 (2017) 550–558. https://doi.org/10.3365/KJMM.2017.55.8.550.

[66] C. Kenel, G. Dasargyri, T. Bauer, A. Colella, A.B. Spierings, C. Leinenbach, K. Wegener, Selective laser melting of an oxide dispersion strengthened (ODS) γ-TiAl alloy towards production of complex structures, Mater. Des. 134 (2017) 81–90. https://doi.org/10.1016/j.matdes.2017.08.034.

[67] S. Mirzababaei, M. Ghayoor, R.P. Doyle, S. Pasebani, In-situ manufacturing of ODS FeCrAlY alloy via laser powder bed fusion, Mater. Lett. 284 (2021) 129046. https://doi.org/10.1016/j.matlet.2020.129046.

[68] M.P. Haines, N.J. Peter, S.S. Babu, E.A. Jägle, In-situ synthesis of oxides by reactive process atmospheres during L-PBF of stainless steel, Addit. Manuf. 33 (2020) 101178.

https://doi.org/10.1016/j.addma.2020.101178.

[69] C. Qiu, A new approach to synthesise high strength nano-oxide dispersion strengthened alloys, J. Alloys Compd. 790 (2019) 1023–1033. https://doi.org/10.1016/j.jallcom.2019.03.221.

[70] D. Riabov, M. Rashidi, E. Hryha, S. Bengtsson, Effect of the powder feedstock on the oxide dispersion strengthening of 316L stainless steel produced by laser powder bed fusion, Mater. Charact. 169 (2020) 110582. https://doi.org/10.1016/j.matchar.2020.110582.

[71] P. Chen, C. Yang, S. Li, M.M. Attallah, M. Yan, In-situ alloyed, oxide-dispersion-strengthened CoCrFeMnNi high entropy alloy fabricated via laser powder bed fusion, Mater. Des. 194 (2020) 108966. https://doi.org/10.1016/j.matdes.2020.108966.

[72] D.R. Eo, S.H. Park, J.W. Cho, Inclusion evolution in additive manufactured 316L stainless steel by laser metal deposition process, Mater. Des. 155 (2018) 212–219. https://doi.org/10.1016/j.matdes.2018.06.001.

[73] M. Song, X. Lin, F. Liu, H. Yang, W. Huang, Effect of environmental oxygen content on the oxide inclusion in laser solid formed AISI 420 stainless steel, Mater. Des. 90 (2016) 459–467. https://doi.org/10.1016/j.matdes.2015.11.003.

[74] M. Ghayoor, S. Mirzababaei, A. Sittiho, I. Charit, B.K. Paul, S. Pasebani, Thermal stability of additively manufactured austenitic 304L ODS alloy, J. Mater. Sci. Technol. 83 (2021) 208–218. https://doi.org/10.1016/j.jmst.2020.12.033.

[75] M. Ghayoor, K. Lee, Y. He, C. hung Chang, B.K. Paul, S. Pasebani, Selective laser melting of austenitic oxide dispersion strengthened steel: Processing, microstructural

evolution and strengthening mechanisms, Mater. Sci. Eng. A. 788 (2020) 139532. https://doi.org/10.1016/j.msea.2020.139532.

[76] J. Deckers, S. Meyers, J.P. Kruth, J. Vleugels, Direct Selective Laser Sintering/Melting of High Density Alumina Powder Layers at Elevated Temperatures, Phys. Procedia. 56 (2014) 117–124. https://doi.org/10.1016/J.PHPRO.2014.08.154.

[77] C.A. Biffi, J. Fiocchi, P. Bassani, A. Tuissi, Continuous wave vs pulsed wave laser emission in selective laser melting of AlSi10Mg parts with industrial optimized process parameters: Microstructure and mechanical behaviour, Addit. Manuf. 24 (2018) 639–646. https://doi.org/10.1016/J.ADDMA.2018.10.021.

[78] J.M. Lonergan, W.G. Fahrenholtz, G.E. Hilmas, Zirconium Diboride with High Thermal Conductivity, J. Am. Ceram. Soc. 97 (2014) 1689–1691. https://doi.org/10.1111/JACE.12950.

[79] W.Y. Yeong, A.B. Kaligar, H.A. Kumar, A. Ali, W. Abuzaid, M. Egilmez, M. Alkhader, F. Abed, A.S. Alnaser, Femtosecond Laser-Based Additive Manufacturing: Current Status and Perspectives, Quantum Beam Sci. 2022, Vol. 6, Page 5. 6 (2022) 5. https://doi.org/10.3390/QUBS6010005.

[80] L. Caprio, A.G. Demir, B. Previtali, Comparative study between CW and PW emissions in selective laser melting, J. Laser Appl. 30 (2018) 032305. https://doi.org/10.2351/1.5040631.

[81] H. Shipley, D. McDonnell, M. Culleton, R. Coull, R. Lupoi, G. O’Donnell, D. Trimble, Optimisation of process parameters to address fundamental challenges during selective laser melting of Ti-6Al-4V: A review, Int. J. Mach. Tools Manuf. 128 (2018) 1–20.

https://doi.org/10.1016/J.IJMACHTOOLS.2018.01.003.

[82] T. Ullsperger, D. Liu, B. Yürekli, G. Matthäus, L. Schade, B. Seyfarth, H. Kohl, R. Ramm, M. Rettenmayr, S. Nolte, Ultra-short pulsed laser powder bed fusion of Al-Si alloys: Impact of pulse duration and energy in comparison to continuous wave excitation, Addit. Manuf. 46 (2021) 102085. https://doi.org/10.1016/J.ADDMA.2021.102085.

[83] A.J. Pinkerton, L. Li, An investigation of the effect of pulse frequency in laser multiple-layer cladding of stainless steel, Appl. Surf. Sci. 208–209 (2003) 405–410. https://doi.org/10.1016/S0169-4332(02)01420-4.

[84] A.J. Pinkerton, L. Li, The effect of laser pulse width on multiple-layer 316L steel clad microstructure and surface finish, Appl. Surf. Sci. 208–209 (2003) 411–416. https://doi.org/10.1016/S0169-4332(02)01422-8.

[85] G.A. Ravi, C. Qiu, M.M. Attallah, Microstructural control in a Ti-based alloy by changing laser processing mode and power during direct laser deposition, Mater. Lett. 179 (2016) 104–108. https://doi.org/10.1016/J.MATLET.2016.05.038.

[86] S. Li, H. Xiao, K. Liu, W. Xiao, Y. Li, X. Han, J. Mazumder, L. Song, Melt-pool motion, temperature variation and dendritic morphology of Inconel 718 during pulsed- and continuous-wave laser additive manufacturing: A comparative study, Mater. Des. 119 (2017) 351–360. https://doi.org/10.1016/J.MATDES.2017.01.065.

[87] H. Xiao, P. Xie, M. Cheng, L. Song, Enhancing mechanical properties of quasi-continuous-wave laser additive manufactured Inconel 718 through controlling the niobium-rich precipitates, Addit. Manuf. 34 (2020) 101278. https://doi.org/10.1016/J.ADDMA.2020.101278.

[88] M. Cheng, X. Xiao, G. Luo, L. Song, Effect of laser intensity profile on the microstructure and texture of Inconel 718 superalloy fabricated by direct energy deposition, J. Mater. Res. Technol. (2022). https://doi.org/10.1016/J.JMRT.2022.03.035.

[89] H. Xiao, S.M. Li, W.J. Xiao, Y.Q. Li, L.M. Cha, J. Mazumder, L.J. Song, Effects of laser modes on Nb segregation and Laves phase formation during laser additive manufacturing of nickel-based superalloy, Mater. Lett. 188 (2017) 260–262. https://doi.org/10.1016/J.MATLET.2016.10.118.

[90] L. Eidam, O. Boine-Frankenheim, D. Winters, Cooling rates and intensity limitations for laser-cooled ions at relativistic energies, Nucl. Instruments Methods Phys. Res. Sect. A Accel. Spectrometers, Detect. Assoc. Equip. 887 (2018) 102–113. https://doi.org/10.1016/J.NIMA.2018.01.038.

[91] J. Kim, S. Ji, Y. Yun, J. Yeo, A Review : Melt Pool Analysis for Selective Laser Melting with Continuous Wave and Pulse Width Modulated Lasers, 27 (2018) 113–119. https://doi.org/10.5757/ASCT.2018.27.6.113.

[92] A.G. Demir, P. Colombo, B. Previtali, From pulsed to continuous wave emission in SLM with contemporary fiber laser sources: effect of temporal and spatial pulse overlap in part quality, Int. J. Adv. Manuf. Technol. 2017 915. 91 (2017) 2701–2714. https://doi.org/10.1007/S00170-016-9948-7.

[93] A. Bin Anwar, Q.C. Pham, Study of the spatter distribution on the powder bed during selective laser melting, Addit. Manuf. 22 (2018) 86–97. https://doi.org/10.1016/J.ADDMA.2018.04.036.

[94] Z.A. Young, Q. Guo, N.D. Parab, C. Zhao, M. Qu, L.I. Escano, K. Fezzaa, W. Everhart,

T. Sun, L. Chen, Types of spatter and their features and formation mechanisms in laser powder bed fusion additive manufacturing process, Addit. Manuf. 36 (2020) 101438. https://doi.org/10.1016/J.ADDMA.2020.101438.

[95] M. Simonelli, C. Tuck, N.T. Aboulkhair, I. Maskery, I. Ashcroft, R.D. Wildman, R. Hague, A Study on the Laser Spatter and the Oxidation Reactions During Selective Laser Melting of 316L Stainless Steel, Al-Si10-Mg, and Ti-6Al-4V, Metall. Mater. Trans. A 2015 469. 46 (2015) 3842–3851. https://doi.org/10.1007/S11661-015-2882-8.

[96] M. Taheri Andani, R. Dehghani, M.R. Karamooz-Ravari, R. Mirzaeifar, J. Ni, A study on the effect of energy input on spatter particles creation during selective laser melting process, Addit. Manuf. 20 (2018) 33–43. https://doi.org/10.1016/J.ADDMA.2017.12.009.

[97] M. Taheri Andani, R. Dehghani, M.R. Karamooz-Ravari, R. Mirzaeifar, J. Ni, Spatter formation in selective laser melting process using multi-laser technology, Mater. Des. 131 (2017) 460–469. https://doi.org/10.1016/J.MATDES.2017.06.040.

[98] D. Wang, S. Wu, F. Fu, S. Mai, Y. Yang, Y. Liu, C. Song, Mechanisms and characteristics of spatter generation in SLM processing and its effect on the properties, Mater. Des. 117 (2017) 121–130. https://doi.org/10.1016/J.MATDES.2016.12.060.

[99] S.A. Khairallah, A.T. Anderson, A. Rubenchik, W.E. King, Laser powder-bed fusion additive manufacturing: Physics of complex melt flow and formation mechanisms of pores, spatter, and denudation zones, Acta Mater. 108 (2016) 36–45. https://doi.org/10.1016/J.ACTAMAT.2016.02.014.

[100] Y. Zhong, L. Liu, J. Zou, X. Li, D. Cui, Z. Shen, Oxide dispersion strengthened stainless steel 316L with superior strength and ductility by selective laser melting, J. Mater. Sci.

Technol. 42 (2020) 97–105. https://doi.org/10.1016/j.jmst.2019.11.004.

[101] E. Getto, B. Tobie, E. Bautista, A.L. Bullens, Z.T. Kroll, M.J. Pavel, K.S. Mao, D.W. Gandy, J.P. Wharry, Thermal Aging and the Hall–Petch Relationship of PM-HIP and Wrought Alloy 625, JOM. 71 (2019) 2837–2845. https://doi.org/10.1007/s11837-019-03532-6.

[102] K. Saeidi, X. Gao, Y. Zhong, Z.J. Shen, Hardened austenite steel with columnar sub-grain structure formed by laser melting, Mater. Sci. Eng. A. (2015). https://doi.org/10.1016/j.msea.2014.12.018.

[103] X. Lou, P.L. Andresen, R.B. Rebak, Oxide inclusions in laser additive manufactured stainless steel and their effects on impact toughness and stress corrosion cracking behavior, J. Nucl. Mater. 499 (2018) 182–190. https://doi.org/10.1016/j.jnucmat.2017.11.036.

[104] P. Deng, M. Song, J. Yang, Q. Pan, S. McAllister, L. Li, B.C. Prorok, X. Lou, On the thermal coarsening and transformation of nanoscale oxide inclusions in 316L stainless steel manufactured by laser powder bed fusion and its influence on impact toughness, Mater. Sci. Eng. A. 835 (2022) 142690. https://doi.org/10.1016/J.MSEA.2022.142690.

[105] P. Deng, H. Yin, M. Song, D. Li, Y. Zheng, B.C. Prorok, X. Lou, On the Thermal Stability of Dislocation Cellular Structures in Additively Manufactured Austenitic Stainless Steels: Roles of Heavy Element Segregation and Stacking Fault Energy, JOM. 72 (2020) 4232–4243. https://doi.org/10.1007/s11837-020-04427-7.

[106] M. Godec, S. Zaefferer, B. Podgornik, M. Šinko, E. Tchernychova, Quantitative multiscale correlative microstructure analysis of additive manufacturing of stainless steel

316L processed by selective laser melting, Mater. Charact. 160 (2020) 110074. https://doi.org/10.1016/j.matchar.2019.110074.

[107] F.C. Pinto, L.S. Aota, I.R. Souza Filho, D. Raabe, H.R.Z. Sandim, Recrystallization in non-conventional microstructures of 316L stainless steel produced via laser powder-bed fusion: effect of particle coarsening kinetics, J. Mater. Sci. (2022) 1–23. https://doi.org/10.1007/S10853-021-06859-1/FIGURES/7.

[108] T. Horn, C. Rock, D. Kaoumi, I. Anderson, E. White, T. Prost, J. Rieken, S. Saptarshi, R. Schoell, M. DeJong, S. Timmins, J. Forrester, S. Lapidus, R. Napolitano, D. Zhang, J. Darsell, Laser powder bed fusion additive manufacturing of oxide dispersion strengthened steel using gas atomized reaction synthesis powder, Mater. Des. 216 (2022) 110574. https://doi.org/10.1016/J.MATDES.2022.110574.

[109] M. Song, X. Lin, F. Liu, H. Yang, W. Huang, Effect of environmental oxygen content on the oxide inclusion in laser solid formed AISI 420 stainless steel, Mater. Des. 90 (2016) 459–467. https://doi.org/10.1016/J.MATDES.2015.11.003.

[110] D.R. Eo, S.G. Chung, J.H. Yang, I.H. Jung, J.W. Cho, Numerical modeling of oxide particle evolution during additive manufacturing, Addit. Manuf. 51 (2022) 102631. https://doi.org/10.1016/J.ADDMA.2022.102631.

[111] U. Scipioni Bertoli, G. Guss, S. Wu, M.J. Matthews, J.M. Schoenung, In-situ characterization of laser-powder interaction and cooling rates through high-speed imaging of powder bed fusion additive manufacturing, Mater. Des. 135 (2017) 385–396. https://doi.org/10.1016/j.matdes.2017.09.044.

[112] L. Tan, J.T. Busby, Formulating the strength factor α for improved predictability of

radiation hardening, J. Nucl. Mater. 465 (2015) 724–730. https://doi.org/10.1016/j.jnucmat.2015.07.009.

[113] Y.M. Wang, T. Voisin, J.T. McKeown, J. Ye, N.P. Calta, Z. Li, Z. Zeng, Y. Zhang, W. Chen, T.T. Roehling, R.T. Ott, M.K. Santala, P.J. Depond, M.J. Matthews, A. V. Hamza, T. Zhu, Additively manufactured hierarchical stainless steels with high strength and ductility, Nat. Mater. 17 (2018) 63–70. https://doi.org/10.1038/NMAT5021.

[114] I. Bogachev, A. Yudin, E. Grigoryev, I. Chernov, M. Staltsov, O. Khasanov, E. Olevsky, Microstructure investigation of 13Cr-2Mo ODS steel components obtained by high voltage electric discharge compaction technique, Materials (Basel). 8 (2015) 7342–7353. https://doi.org/10.3390/ma8115381.

[115] K. Sasai, Y. Mizukami, Effect of Stirring on Oxidation Rate of Molten Steel., ISIJ Int. 36 (1996) 388–394. https://doi.org/10.2355/isijinternational.36.388.

[116] K. Mundra, T. Debroy, A general model for partitioning of gases between a metal and its plasma environment, Metall. Mater. Trans. B. 26 (1995) 149–157. https://doi.org/10.1007/BF02648987.

[117] Y. Shi, Z. Lu, L. Yu, R. Xie, Y. Ren, G. Yang, Microstructure and tensile properties of Zr-containing ODS-FeCrAl alloy fabricated by laser additive manufacturing, Mater. Sci. Eng. A. 774 (2020). https://doi.org/10.1016/j.msea.2020.138937.

[118] B.K. Paul, K. Lee, Y. He, M. Ghayoor, C. hung Chang, S. Pasebani, Oxide dispersion strengthened 304 L stainless steel produced by ink jetting and laser powder bed fusion, CIRP Ann. 69 (2020) 193–196. https://doi.org/10.1016/j.cirp.2020.04.071.

[119] C. Kim, H. Yin, A. Shmatok, B.C. Prorok, X. Lou, K.H. Matlack, Ultrasonic

nondestructive evaluation of laser powder bed fusion 316L stainless steel, Addit. Manuf. 38 (2021) 101800. https://doi.org/10.1016/j.addma.2020.101800.

[120] J. Chao, R. Rementeria, M. Aranda, C. Capdevila, J.L. Gonzalez-Carrasco, Comparison of ductile-to-brittle transition behavior in two similar ferritic oxide dispersion strengthened alloys, Materials (Basel). 9 (2016) 637. https://doi.org/10.3390/ma9080637.

[121] C. Qiu, M. Al Kindi, A.S. Aladawi, I. Al Hatmi, A comprehensive study on microstructure and tensile behaviour of a selectively laser melted stainless steel, Sci. Rep. 8 (2018) 1–16. https://doi.org/10.1038/s41598-018-26136-7.

[122] B.W. Baker, L.N. Brewer, Joining of Oxide Dispersion Strengthened Steels for Advanced Reactors, JOM. 66 (2014) 2442–2457. https://doi.org/10.1007/S11837-014-1206-6/FIGURES/10.

[123] J. Ribis, M.A. Thual, T. Guilbert, Y. de Carlan, A. Legris, Relaxation path of metastable nanoclusters in oxide dispersion strengthened materials, J. Nucl. Mater. 484 (2017) 183–192. https://doi.org/10.1016/J.JNUCMAT.2016.12.007.

[124] A. Yoshie, T. Fujita, M. Fujioka, K. Okamoto, H. Morikawa, Formulation of the decrease in dislocation density of deformed austenite due to static recovery and recrystallization, ISIJ Int. 36 (1996) 474–480. https://doi.org/10.2355/isijinternational.36.474.

[125] B. Gwalani, R.M. Pohan, O.A. Waseem, T. Alam, S.H. Hong, H.J. Ryu, R. Banerjee, Strengthening of Al0.3CoCrFeMnNi-based ODS high entropy alloys with incremental changes in the concentration of Y2O3, Scr. Mater. 162 (2019) 477–481. https://doi.org/10.1016/J.SCRIPTAMAT.2018.12.021.

[126] H. Yin, M. Song, P. Deng, L. Li, B.C. Prorok, X. Lou, Thermal stability and

microstructural evolution of additively manufactured 316L stainless steel by laser powder bed fusion at 500–800 °C, Addit. Manuf. 41 (2021) 101981. https://doi.org/10.1016/J.ADDMA.2021.101981.

[127] W.M. Tucho, V.H. Lysne, H. Austbø, A. Sjolyst-Kverneland, V. Hansen, Investigation of effects of process parameters on microstructure and hardness of SLM manufactured SS316L, J. Alloys Compd. 740 (2018) 910–925. https://doi.org/10.1016/J.JALLCOM.2018.01.098.

[128] Y. Zhong, L. Liu, S. Wikman, D. Cui, Z. Shen, Intragranular cellular segregation network structure strengthening 316L stainless steel prepared by selective laser melting, J. Nucl. Mater. 470 (2016) 170–178. https://doi.org/10.1016/j.jnucmat.2015.12.034.

[129] K. Saeidi, X. Gao, F. Lofaj, L. Kvetková, Z.J. Shen, Transformation of austenite to duplex austenite-ferrite assembly in annealed stainless steel 316L consolidated by laser melting, J. Alloys Compd. 633 (2015) 463–469. https://doi.org/10.1016/j.jallcom.2015.01.249.

[130] T. Voisin, J.B. Forien, A. Perron, S. Aubry, N. Bertin, A. Samanta, A. Baker, Y.M. Wang, New insights on cellular structures strengthening mechanisms and thermal stability of an austenitic stainless steel fabricated by laser powder-bed-fusion, Acta Mater. 203 (2021) 116476. https://doi.org/10.1016/j.actamat.2020.11.018.

[131] K.M. Bertsch, G. Meric de Bellefon, B. Kuehl, D.J. Thoma, Origin of dislocation structures in an additively manufactured austenitic stainless steel 316L, Acta Mater. 199 (2020) 19–33. https://doi.org/10.1016/j.actamat.2020.07.063.

[132] X. Zhou, X.Y. Li, K. Lu, Stabilizing nanograins in metals with grain boundary relaxation, Scr. Mater. 187 (2020) 345–349. https://doi.org/10.1016/J.SCRIPTAMAT.2020.06.047.

[133] J. Ding, Z. Shang, Y.F. Zhang, R. Su, J. Li, H. Wang, X. Zhang, Tailoring the thermal stability of nanocrystalline Ni alloy by thick grain boundaries, Scr. Mater. 182 (2020) 21–26. https://doi.org/10.1016/J.SCRIPTAMAT.2020.02.032.

[134] P. Street, OVERVIEW A THEORY PINNING FOR GRAIN BOUNDARY, 35 (1987).

[135] Z. Li, Y. Cui, W. Yan, D. Zhang, Y. Fang, Y. Chen, Q. Yu, G. Wang, H. Ouyang, C. Fan, Q. Guo, D.B. Xiong, S. Jin, G. Sha, N. Ghoniem, Z. Zhang, Y.M. Wang, Enhanced strengthening and hardening via self-stabilized dislocation network in additively manufactured metals, Mater. Today. 50 (2021) 79–88. https://doi.org/10.1016/J.MATTOD.2021.06.002.

[136] Y. Cui, E. Aydogan, J.G. Gigax, Y. Wang, A. Misra, S.A. Maloy, N. Li, In Situ Micro-Pillar Compression to Examine Radiation-Induced Hardening Mechanisms of FeCrAl Alloys, Acta Mater. 202 (2021) 255–265. https://doi.org/10.1016/J.ACTAMAT.2020.10.047.

[137] D. Xie, B. Wei, W. Wu, J. Wang, Crystallographic Orientation Dependence of Mechanical Responses of FeCrAl Micropillars, Cryst. 2020, Vol. 10, Page 943. 10 (2020) 943. https://doi.org/10.3390/CRYST10100943.

[138] M.C. Brennan, J.S. Keist, T.A. Palmer, D.L. Bourell, W. Frazier, H. Kuhn, M. Seifi, Defects in Metal Additive Manufacturing Processes, J. Mater. Eng. Perform. 2021 307. 30 (2021) 4808–4818. https://doi.org/10.1007/S11665-021-05919-6.

[139] Z.H. Xiong, S.L. Liu, S.F. Li, Y. Shi, Y.F. Yang, R.D.K. Misra, Role of melt pool boundary condition in determining the mechanical properties of selective laser melting AlSi10Mg alloy, Mater. Sci. Eng. A. 740–741 (2019) 148–156.

https://doi.org/10.1016/J.MSEA.2018.10.083.

[140] W. Shifeng, L. Shuai, W. Qingsong, C. Yan, Z. Sheng, S. Yusheng, Effect of molten pool boundaries on the mechanical properties of selective laser melting parts, J. Mater. Process. Technol. 214 (2014) 2660–2667. https://doi.org/10.1016/J.JMATPROTEC.2014.06.002.

[141] X. Yang, F. Tang, X. Hao, Z. Li, Oxide Evolution During the Solidification of 316L Stainless Steel from Additive Manufacturing Powders with Different Oxygen Contents, Metall. Mater. Trans. B Process Metall. Mater. Process. Sci. 52 (2021) 2253–2262. https://doi.org/10.1007/S11663-021-02191-W/FIGURES/8.

[142] H. Yu, S. Hayashi, K. Kakehi, Y.L. Kuo, Study of Formed Oxides in IN718 Alloy during the Fabrication by Selective Laser Melting and Electron Beam Melting, Met. 2019, Vol. 9, Page 19. 9 (2018) 19. https://doi.org/10.3390/MET9010019.

[143] D.R. Eo, S.G. Chung, J.M. Jeon, J.W. Cho, Melt pool oxidation and reduction in powder bed fusion, Addit. Manuf. 41 (2021) 101982. https://doi.org/10.1016/J.ADDMA.2021.101982.

[144] K.A. Mumtaz, N. Hopkinson, Selective Laser Melting of thin wall parts using pulse shaping, J. Mater. Process. Technol. 210 (2010) 279–287. https://doi.org/10.1016/J.JMATPROTEC.2009.09.011.

[145] S.A. Khairallah, A.A. Martin, J.R.I. Lee, G. Guss, N.P. Calta, J.A. Hammons, M.H. Nielsen, K. Chaput, E. Schwalbach, M.N. Shah, M.G. Chapman, T.M. Willey, A.M. Rubenchik, A.T. Anderson, Y. Morris Wang, M.J. Matthews, W.E. King, Controlling interdependent meso-nanosecond dynamics and defect generation in metal 3D printing, Science (80-.). 368 (2020) 660–665.

https://doi.org/10.1126/SCIENCE.AAY7830/SUPPL_FILE/AAY7830S9.MP4.

[146] Y. Liu, Y. Yang, S. Mai, D. Wang, C. Song, Investigation into spatter behavior during selective laser melting of AISI 316L stainless steel powder, Mater. Des. 87 (2015) 797–806. https://doi.org/10.1016/J.MATDES.2015.08.086.

[147] M. Simonelli, C. Tuck, N.T. Aboulkhair, I. Maskery, I. Ashcroft, R.D. Wildman, R. Hague, A Study on the Laser Spatter and the Oxidation Reactions During Selective Laser Melting of 316L Stainless Steel, Al-Si10-Mg, and Ti-6Al-4V, Metall. Mater. Trans. A Phys. Metall. Mater. Sci. 46 (2015) 3842–3851. https://doi.org/10.1007/s11661-015-2882-8.

[148] M. Qu, Q. Guo, L.I. Escano, A. Nabaa, S.M.H. Hojjatzadeh, Z.A. Young, L. Chen, Controlling process instability for defect lean metal additive manufacturing, Nat. Commun. 2022 131. 13 (2022) 1–8. https://doi.org/10.1038/s41467-022-28649-2.

[149] A.R. Nassar, M.A. Gundermann, E.W. Reutzel, P. Guerrier, M.H. Krane, M.J. Weldon, Formation processes for large ejecta and interactions with melt pool formation in powder bed fusion additive manufacturing, Sci. Reports 2019 91. 9 (2019) 1–11. https://doi.org/10.1038/s41598-019-41415-7.

[150] S.A. Khairallah, A.A. Martin, J.R.I. Lee, G. Guss, N.P. Calta, J.A. Hammons, M.H. Nielsen, K. Chaput, E. Schwalbach, M.N. Shah, M.G. Chapman, T.M. Willey, A.M. Rubenchik, A.T. Anderson, Y. Morris Wang, M.J. Matthews, W.E. King, Controlling interdependent meso-nanosecond dynamics and defect generation in metal 3D printing, Science (80-.). 368 (2020) 660–665. https://doi.org/10.1126/SCIENCE.AAY7830/SUPPL_FILE/AAY7830S9.MP4.

[151] M.B. Wilms, R. Streubel, F. Frömel, A. Weisheit, J. Tenkamp, F. Walther, S. Barcikowski, J.H. Schleifenbaum, B. Gökce, Laser additive manufacturing of oxide dispersion strengthened steels using laser-generated nanoparticle-metal composite powders, in: Procedia CIRP, Elsevier B.V., 2018: pp. 196–200. https://doi.org/10.1016/j.procir.2018.08.093.

[152] D. Riabov, E. Hryha, M. Rashidi, S. Bengtsson, L. Nyborg, Effect of atomization on surface oxide composition in 316L stainless steel powders for additive manufacturing, Surf. Interface Anal. 52 (2020) 694–706. https://doi.org/10.1002/sia.6846.

[153] A. De Luca, C. Kenel, J. Pado, S.S. Joglekar, D.C. Dunand, C. Leinenbach, Thermal stability and influence of Y2O3 dispersoids on the heat treatment response of an additively manufactured ODS Ni–Cr–Al–Ti γ/γ′ superalloy, J. Mater. Res. Technol. 15 (2021) 2883–2898. https://doi.org/10.1016/J.JMRT.2021.09.076.

[154] Otsuka, Shinya, and Zensaku Kozuka. "The diffusivities of oxygen in liquid nickel and liquid iron determined by electrochemical measurements." Transactions of the Japan Institute of Metals 18.10 (1977): 690-696.

[155] B. AlMangour, Y.-K. Kim, D. Grzesiak, K.-A. Lee, Novel TiB2-reinforced 316L stainless steel nanocomposites with excellent room- and high-temperature yield strength developed by additive manufacturing, Compos. Part B Eng. 156 (2019) 51–63. https://doi.org/10.1016/J.COMPOSITESB.2018.07.050.

[156] T.T. Roehling, S.S.Q. Wu, S.A. Khairallah, J.D. Roehling, S.S. Soezeri, M.F. Crumb, M.J. Matthews, Modulating laser intensity profile ellipticity for microstructural control during metal additive manufacturing, Acta Mater. 128 (2017) 197–206.

https://doi.org/10.1016/J.ACTAMAT.2017.02.025.